Ice dynamics and mass balance in the grounding zone of outlet glaciers in the Transantarctic Mountains

---

A thesis
submitted in partial fulfilment
of the requirements for the Degree
of
Doctor of Philosophy
by
Oliver John Marsh

Gateway Antarctica
University of Canterbury
2013

Table of Contents

List of Figures

List of Tables

Abstract

The Antarctic grounding zone has a disproportionately large effect on glacier dynamics and ice sheet stability relative to its size but remains poorly characterised across much of the continent. Accurate ice velocity and thickness information is needed in the grounding zone to determine glacier outflow and establish to what extent changing ocean and atmospheric conditions are affecting the mass balance of individual glacier catchments.

This thesis describes new satellite remote sensing techniques for measuring ice velocity and ice thickness, validated using ground measurements collected on the Beardmore, Skelton and Darwin Glaciers and applied to other Transantarctic Mountain outlet glaciers to determine ice discharge. Outlet glaciers in the Transantarctic Mountains provide an important link between the East and West Antarctic Ice Sheets but remain inadequately studied. While long-term velocities in this region are shown here to be stable, instantaneous velocities are sensitive to stresses induced by ocean tides, with fluctuations of up to 50% of the mean observed in GPS measurements. The potential error induced in averaged satellite velocity measurements due to these effects is shown to be resolvable above background noise in the grounding zone but to decrease rapidly upstream. Using a new inverse finite-element modelling approach based on regularization of the elastic-plate bending equations, tidal flexure information from differential InSAR is used to calculate ice stiffness and infer thickness in the grounding zone. This technique is shown to be successful at reproducing the thickness distribution for the Beardmore Glacier, eliminating current issues in the calculation of thickness from freeboard close to the grounding line where ice is not in hydrostatic equilibrium. Modelled thickness agrees to within 10% of ground penetrating radar measurements.

Calibrated freeboard measurements and tide-free velocities in the grounding zones of glaciers in the western Ross Sea are used to calculate grounding zone basal melt rates, with values between 1.4 and 11.8 ma^{-1} in this region. While strongly dependent on grounding line ice thickness and velocity, melt rates show no latitudinal trend between glaciers, although detailed error analysis highlights the need for much improved estimates of firn density distribution in regions of variable accumulation such as the Transantarctic Mountains.

Deputy Vice-Chancellor's Office
Postgraduate Office

UNIVERSITY OF CANTERBURY
Te Whare Wānanga o Waitaha
CHRISTCHURCH NEW ZEALAND

Co-authorship Form

This form is to accompany the submission of any thesis that contains research reported in co-authored work that has been published, accepted for publication, or submitted for publication. A copy of this form should be included for each co-authored work that is included in the thesis. Completed forms should be included at the front (after the thesis abstract) of each copy of the thesis submitted for examination and library deposit.

Please indicate the chapter/section/pages of this thesis that are extracted from co-authored work and provide details of the publication or submission from which the extract comes:

Chapter 2 is dervied from **Marsh, O.J. and W. Rack, 2012. A method of calculating ice-shelf surface velocity using ICESat altimetry, Polar Record, 48(244), 25-30, doi:10.1017/S0032247411000362**

Please detail the nature and extent (%) of contribution by the candidate:
The candidate has performed all ICESat processing, conceived the analysis and written the text. W. Rack has given supervisory comments and suggestions to improve the paper. Candidate contribution 90%.

Certification by co-authors:
If there is more than one co-author then a single co-author can sign on behalf of all.
The undersigned certifies that:

- the above statement correctly reflects the nature and extent of the PhD candidate's contribution to this co-authored work;
- in cases where the candidate was the lead author of the co-authored work he or she wrote the text.

Name: Signature: Date:

Deputy Vice-Chancellor's Office
Postgraduate Office

UNIVERSITY OF CANTERBURY
Te Whare Wānanga o Waitaha
CHRISTCHURCH NEW ZEALAND

Co-authorship Form

This form is to accompany the submission of any thesis that contains research reported in co-authored work that has been published, accepted for publication, or submitted for publication. A copy of this form should be included for each co-authored work that is included in the thesis. Completed forms should be included at the front (after the thesis abstract) of each copy of the thesis submitted for examination and library deposit.

Please indicate the chapter/section/pages of this thesis that are extracted from co-authored work and provide details of the publication or submission from which the extract comes:

Chapter 3 is derived from **Marsh, O.J., W. Rack, D. Floricioiu, N.R. Golledge and W. Lawson, 2013. Tidally-induced velocity variations of the Beardmore Glacier, Antarctica, and their representation in satellite measurements of ice velocity, The Cryosphere Discuss, 7, 1761-1785, doi:10.5194/tcd-7-1761-2013.**

Please detail the nature and extent (%) of contribution by the candidate:
The candidate has performed all GPS and TerraSAR-X processing individually, conceived the analysis and written the text. Assistance has been given from W. Rack and N. Golledge in collection of GPS data in the field. D. Floricioiu has provided raw TerraSAR-X data. All authors have given supervisory comments and suggestions to improve the paper. Candidate contribution $\sim 90\%$.

Certification by co-authors:
If there is more than one co-author then a single co-author can sign on behalf of all.
The undersigned certifies that:

- the above statement correctly reflects the nature and extent of the PhD candidate's contribution to this co-authored work;
- in cases where the candidate was the lead author of the co-authored work he or she wrote the text.

Name: Signature: Date:

Deputy Vice-Chancellor's Office
Postgraduate Office

UNIVERSITY OF CANTERBURY
Te Whare Wānanga o Waitaha
CHRISTCHURCH NEW ZEALAND

Co-authorship Form

This form is to accompany the submission of any thesis that contains research reported in co-authored work that has been published, accepted for publication, or submitted for publication. A copy of this form should be included for each co-authored work that is included in the thesis. Completed forms should be included at the front (after the thesis abstract) of each copy of the thesis submitted for examination and library deposit.

Please indicate the chapter/section/pages of this thesis that are extracted from co-authored work and provide details of the publication or submission from which the extract comes:

Chapter 4 is derived from **Marsh, O.J., W. Rack, N.R. Golledge, W. Lawson and D. Floricioiu, 2013. Grounding zone ice thickness from InSAR: Inverse modelling of tidal elastic bending, Journal of Glaciology**

Please detail the nature and extent (%) of contribution by the candidate:
The candidate has performed all GPR processing and finite element modelling individually, conceived the analysis and written the text. Assistance has been given from W. Rack and N. Golledge in collection of GPS and GPR data. D. Floricioiu provided raw TerraSAR-X data. W. Rack converted raw TerraSAR-X SLCs into an interferogram. All authors have given supervisory comments and suggestions to improve the paper. Candidate contribution $\sim 90\%$.

Certification by co-authors:
If there is more than one co-author then a single co-author can sign on behalf of all.
The undersigned certifies that:

- the above statement correctly reflects the nature and extent of the PhD candidate's contribution to this co-authored work;
- in cases where the candidate was the lead author of the co-authored work he or she wrote the text.

Name: Signature: Date:

Acknowledgements

This thesis has benefited from the support and guidance of many people without whom it would not have been possible. Firstly I would like to thank my supervisors: Wolfgang Rack, who has always been around to talk to and discuss ideas with; and Wendy Lawson who has kept me on track and motivated to finish. Both my supervisors have allowed me the flexibility to pursue interesting ideas as they arose and offered guidance when necessary.

I would also like to acknowledge Nick Golledge at Victoria University of Wellington for the opportunity to conduct fieldwork in Antarctica and the Antarctic Research Centre for giving me a temporary desk at VUW and making me feel welcome for several weeks after the Christchurch earthquakes. I have become particularly involved with the small New Zealand Snow and Ice Research Group and New Zealand Antarctic research community, the members of which have always provided interesting discussions related to this project. Dana Floricioiu and Wael Abdel Jaber were also supportive during a productive research stay at DLR, giving me guidance on TerraSAR-X satellite data aqcuisition and processing.

I am grateful for assistance provided by Justin Harrison and Nick Key in preparing equipment for Antarctic fieldwork and to Dean Arthur, Antarctica New Zealand and the Scott Base staff for support in field. I also talked to Charles Swithinbank prior to our fieldwork on the Beardmore Glacier and his raw data and accounts from the area were instrumental in planning radar transect routes and GPS positions.

This work would not have been possible without generous support from a Commonwealth Scholarship and additional funding from Gateway Antarctica and GNS Science (ANDRILL Project No. CO5X1001). I would like to thank everyone at Gateway Antarctica for providing a friendly atmosphere in which to work, particularly my post-graduate office mates Crystal and Erin for advice at the beginning and Dan and Sira who have been supportive whilst I have been writing up.

Finally, a special thanks to all my friends in NZ, particularly Ellen, Brian and Sophie, who have kept me in the mountains during the weekends. And to my parents for their support, encouragement and patience from the other side of the world.

Chapter I

Introduction

1.1 The Antarctic Grounding Zone

The Antarctic Ice Sheet contains approximately 27 $\times 10^6$ km^3 of ice - enough to raise global sea levels by an average of 58m were it all to melt (Fretwell et al., 2013). In order to determine the sensitivity of the ice sheets to external climate forcing and to assess the rate at which melting in Antarctica could affect sea level, it is necessary to have a good knowledge of current glacier dynamics. Local ice discharge measurements can be used to identify glaciers which are not in equilibrium with their current environment and most susceptible to changing conditions, as well as to increase the temporal and spatial resolution of regional and continental ice volume calculations. The change in mass of the ice sheet, known as mass balance, can be determined by looking at the difference between inputs and outputs.

The major input of mass to Antarctica is snowfall, while the majority of ice is lost to the ocean, either via iceberg calving at the margins of ice shelves and tidewater glaciers, or melting at the ice-ocean interface (Jacobs et al., 1992). Increases in snowfall may offset some of the predicted increases in ice discharge (Winkelmann, 2011), but it is vital that the high uncertainties in ice discharge calculations are reduced, specifically related to glacier outflows. A more standardised quantification of flow variability and mass balance of individual Antarctic outlet glaciers will allow a better determination of how and where changes in the Antarctic Ice Sheet will be most rapid and most significant.

Rapidly warming oceans and redirection of warm ocean currents onto the continental shelf have been documented around Antarctica (Jacobs et al., 2011; Walker et al., 2007) and where this ocean warming is occurring similarly rapid ice loss from the ice sheet is also observed (Shepherd et al., 2004; Jenkins et al., 2010; Joughin et al., 2012). The combined effects of continued ocean warming and changing circulation

patterns are predicted to have the greatest influence on ice sheet behaviour in the next century through their effect on ice shelf basal melting and dynamic thinning of tidewater glaciers (Hellmer et al., 2012; Pritchard et al., 2009, 2012). The effect of warm oceans is particularly strong at the landward margin of the ice shelves (Rignot and Jacobs, 2002). This instantaneous point of transition between a floating ice shelf and the grounded ice sheet is know as the 'grounding line' and is the point at which ice becomes sufficiently buoyant that it is no longer in contact with the underlying land. It is difficult to exactly define the grounding line position, which moves in relation to ocean tides and glacier flow variability. Due to the ephemeral nature of the grounding, this region is sometimes referred to as the 'grounding zone' (e.g. Rignot et al., 2011a). More generally, however, the term grounding zone is used to refer to the wider region downstream of the grounding line extending from the landward limit of tidally induced flexure to the hydrostatic line at which ice begins to oscillate with the full tidal range (Fricker et al., 2009; Walker et al., 2013). For clarity, reference to the grounding zone hereafter will assume the latter definition.

Grounding zones have received increasing attention over the last 40 years as their role in the stability and future response of the marine ice sheets to climate change has become more apparent (Weertman, 1974; Vanderveen, 1985; Schoof, 2007; Vaughan, 2008). Hysteresis in grounding line migration has been shown through modelling studies, with a future reversal of oceanic temperature to current levels being unable to reverse predicted grounding line retreat to a point of stability once a certain threshold is reached (Schoof, 2007). For reverse sloping beds which deepen as you move inland, small perturbations in external conditions may lead to thinning and acceleration of ice in the grounding zone causing rapid and irreversible grounding line retreat and further increasing ice discharge and thinning in a positive feedback loop.

Major and rapid changes to the ice sheet mass balance and hence global sea level are predicted to result from increased discharge across grounding zones around Antarctica and grounding line retreat. This increased discharge is already being seen in areas of West Antarctic such as Pine Island Glacier, where warm ocean currents encroaching on the continental shelf and in the ice shelf cavity have triggered acceleration and thinning starting in the grounding zone and spreading upstream (Wingham, 2009). The changes are strongest in the grounding zone where pressure at depth causes a depression of the melting point of ice, and melt rates can reach over

100 m yr^{-1} (Payne et al., 2007; Bindschadler et al., 2011b; Dutrieux et al., 2013). As buoyant plumes of meltwater rise along the ice-ocean boundary they lose heat and pressure and their efficiency at melting is reduced. Although the grounding zones of a few fast flowing ice streams and outlet glaciers are well studied by ground-based and airborne measurements (e.g. Scott et al., 2009; Smith et al., 2009), only recently have attempts been made to fully map grounding zones on a continent-wide scale (Bindschadler et al., 2011a; Rignot et al., 2011a). Even so, techniques to identify the grounding zone rely on different observable surface characteristics which often produce diverging estimates of grounding line location, despite numerical models of the grounding zone requiring sub-kilometre discretisation (Pattyn et al., 2012b).

Given the high sensitivity of the grounding zone to external forcing in relation to other regions of the Antarctic Ice Sheet; the significant impact of changes in basal melt rate and distribution on grounding line retreat (Walker et al., 2008); and the amplification of any changes through potential positive feedbacks (Schoof, 2007), it is vital to measure ice discharge and melt rates in the grounding zone with the highest accuracy possible. Measuring these components of the Antarctic mass balance requires knowledge of grounding line location, surface velocity and ice thickness.

1.2 Aims and Objectives

The aim of this research is to standardise and improve how ice discharge and basal melt rates can be calculated in Antarctic grounding zones using satellite remote sensing. By addressing uncertainties in ice velocity caused by ocean tides and uncertainties in ice thickness due to bending stresses in the grounding zone, a better baseline can be determined for monitoring glacier discharge and change related to oceanic warming. The ability to accurately measure ice discharge and melt rates in the grounding zone from satellite is a vital component for a comprehensive assessment of ice dynamics and mass balance for the whole of Antarctica. Specific objectives are:

1. To investigate new satellite remote sensing techniques for identification of grounding line location and ice velocity in the grounding zone.

2. To quantify the influence of diurnal ocean tides on short-term velocity fluctu-

ations in the grounding zone, with specific focus on how these fluctuations are represented in satellite measurements of annual average velocities.

3. To improve satellite measurements of ice thickness in the grounding zone by modelling the relationship between observed tidally-induced flexure, ice rheology and ice thickness distribution.

4. To combine these improved techniques with established methods for thickness and velocity mapping and more accurately quantify and compare ice discharge and mass balance in the grounding zone of outlet glaciers along a latitudinal gradient in the Transantarctic Mountains.

Objectives 1-3 are developed and explained in detail for the Beardmore Glacier, a glacier of moderate size and discharge feeding into the Ross Ice Shelf at 83.5 °S (Figure 1.3). The approaches discussed in chapters 1-3 are then expanded to fulfill objective 4 using remote sensing data from five additional glaciers in the Ross Sea region. From north to south these glaciers are the David and Mackay Glaciers, terminating in ice tongues on the Victoria Land Coast; and the Skelton, Mulock and Darwin-Hatherton Glaciers terminating in the Ross Ice Shelf (Figure 1.1).

1.3 Study Area

Recent coring in the Ross Sea region as part of the ANDRILL project (Naish et al., 2009) and associated modelling have demonstrated that the Ross Ice Shelf has been unstable in the past and may be at risk of rapid future collapse (Pollard and DeConto, 2009). The vulnerability of the West Antarctic Ice Sheet to climate change has been extensively discussed and is the subject of ongoing discussion (Oppenheimer, 1998; Vaughan, 2008; Joughin and Alley, 2011), but the effects of any future changes in the extent of the West Antarctic Ice Sheet on the much larger East Antarctic Ice Sheet are not well understood. Increased accumulation in East Antarctica could act to stabilise and support the Ross Ice Shelf under oceanic warming scenarios (Davis et al., 2005; Boening et al., 2012) while thinning of the ice shelf could lead to acceleration of East Antarctic outlet glaciers as has been observed on the Antarctic Peninsula following the thinning and collapse of smaller ice shelves (Rott et al., 2002; Scambos et al., 2004; Hulbe et al., 2008). Grounding zones of the

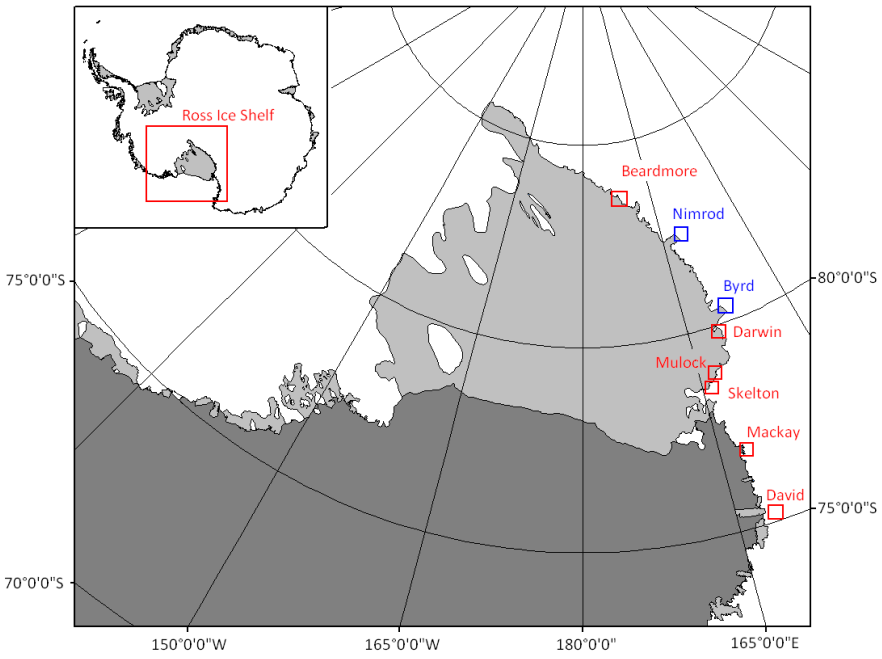

Figure 1.1: Locations of outlet glaciers where discharge and melt rates are calculated (red) and other major outlet glaciers in the Transantarctic Mountains (blue)

glaciers which drain ice from East Antarctica, through the Transantarctic Mountains and into the Ross Ice Shelf form both the boundary between East and West and the boundary between grounded ice and floating ice. These transitions are the key to understanding the relationship between the two ice sheets and between ocean warming and mass balance, and are therefore also important for accurately modelling the future behaviour of the Ross Ice Shelf.

The grounding line position of ice in the Ross Ice Shelf retreated relatively rapidly from near the continental shelf break at the last glacial maximum to its current position (Conway et al., 1999). For the last 9,000 years, however, the ice shelf calving front has remained approximately in the same position near to Ross Island (Mckay et al., 2008) and the location of the grounding zone on the Siple Coast shows relative stability interrupted by episodes of rapid advance and retreat over the last millennium (Horgan and Anandakrishnan, 2006; Catania et al., 2012). Whilst ice shelves on the Antarctic Peninsula and in the Amundsen Sea have undergone either steady retreat or catastrophic collapse in the last few decades linked to atmospheric and oceanic warming (Scambos et al., 2000; Shepherd et al., 2003; Vieli et al., 2007; Shepherd et al., 2010), the Ross Ice Shelf has undergone only relatively localised thinning related to Siple Coast ice stream variability (Pritchard et al., 2012). While the ice is pinned by islands and ice-rises it is difficult to predict its vulnerability to climatic warming. North of the Ross Ice Shelf, the outlet glaciers flow directly into the Ross Sea and in some places form extensive ice tongues sticking out tens of kilometres into the ocean (Frezzotti, 1997). As the thinning or collapse of the ice tongues may be an indicator of thinning and possible collapse of the Ross Ice Shelf, a thorough investigation of outlet glacier ice dynamics and mass balance is also needed in this area. Southward migration of outlet glacier retreat and ice shelf instability has been observed on the Antarctic Peninsula linked to regional warming (Morris et al., 2003; Cook et al., 2005) and the Transantarctic Mountain outlet glaciers provide a similarly extensive 'latitudinal gradient' from $\sim 70°$S to $\sim 85°$S over which to monitor the progression of change.

1.4 Identification of the Grounding Zone

Characteristics of the grounding zone and satellite techniques to identify its location can be divided into 'static' and 'dynamic'. Static (or topographic) identifica-

tion involves delineating the instantaneous surface impression and observable surface physical features of the grounding zone, whilst dynamic identification involves monitoring the pattern of ice movement created at the surface in response to ocean tides. Where grounded ice with a steep surface gradient meets an ice shelf a point of inflection can be used to identify the grounding line and can be mapped using altimetry or photogrammetry (Bohlander and Scambos, 2007; Bindschadler et al., 2011a). This approach works well in steep outlet glaciers with a distinct change in stress conditions across the transition from grounded to floating ice but is not successful in flat regions where the ice is loosely grounded on an 'ice-plain', such as in Pine Island Bay or the Siple Coast (Corr et al., 2001). Grounding lines are also sometimes characterised by areas of intense crevassing as basal shear stress is reduced. Crevasses formed in these areas may then propagate downstream across the floating ice where internal stresses are once again more uniform (Glasser and Scambos, 2008).

In tidal or marine-terminating glaciers the grounding line migrates with the tides as ice is lifted off the bedrock by the increasing hydrostatic pressure. Freely floating ice experiences the full range of vertical tidal motion and can be considered to be in hydrostatic equilibrium (Bindschadler et al., 2011a) while upstream of this point stresses are transmitted from the grounding line and partially resist the vertical movement of the ice. Grounding of the ice only during low tide is known as ephemeral grounding (Schmeltz et al., 2001). The amount of horizontal movement of the grounding line over a tidal cycle will depend on the slope of the underlying bed and the tidal range, both of which affect the surface impression of the ice at the transition. The limit of flexure or hinge-line marks the boundary between ice whose surface elevation is raised by peak high tides and ice which maintains a stationary profile (Figure1.2). A small opposite displacement may also be observed upstream of the grounding line where the bedrock at the grounding-line acts as a fulcrum (Walker et al., 2013). High precision altimetry and interferometric synthetic aperture radar (InSAR) have been used to measure these small vertical displacements to identify the region affected by ocean tides (Goldstein et al., 1993; Fricker and Padman, 2006; Brunt et al., 2010a; Rignot et al., 2011a). These methods involve measuring the elevation of the glacier surface with high precision at periods when ocean tides are unequal. Satellite-based altimetry currently requires interpolation between grounding zone positions, while InSAR requires high volumes of data and

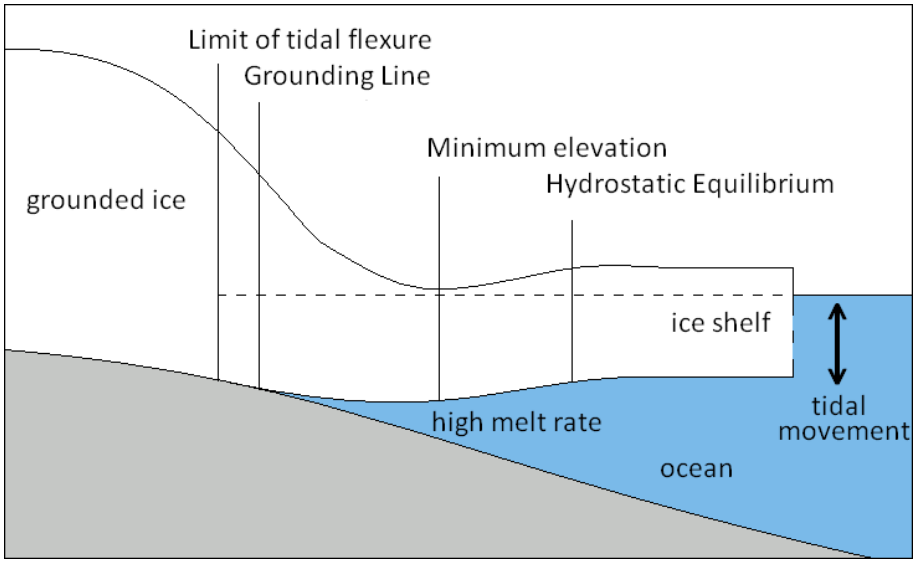

Figure 1.2: Schematic representation of a grounding zone, adapted from Fricker and Padman (2006)

may suffer from problems with loss of image coherence in very dynamic grounding zones with rapid changes in surface characteristics. Identifying new methods to map the grounding zone without ambiguity would be a useful contribution both for measuring ice flux and monitoring grounding line migration.

1.5 Measurement of Ice Velocity in Antarctica

The most rapid changes to the Antarctic Ice Sheet in the short-term have been to ice velocity in grounding zones. Rott et al. (2002) and Scambos et al. (2004) observed a two- to six-fold increase in the speed of outlet glaciers following the break up of the Larsen B Ice Shelf, while Pritchard and Vaughan (2007) observed an average velocity increase of 12% over ten years for glaciers on the west coast of the Antarctic Peninsula. Velocity has been measured precisely on the ground using triangulation of stakes (e.g. Swithinbank, 1963) and more recently precise GPS measurements have provided a much finer temporal resolution of velocity (Bindschadler et al., 2003; Murray et al., 2007; Brunt et al., 2010b) and the identification of tidally-controlled velocity fluctuations (Gudmundsson, 2007; Legresy et al., 2004). The high-precision of GPS surveys allows a better quantification of short-term change but does not

provide suitable spatial coverage or repeatability for application across all Antarctic grounding zones. Repeat GPS measurements are costly to implement yet the potential for satellite monitoring of short-term variability is relatively unexplored.

High precision ground-based velocity measurements can be used to validate satellite-derived velocity fields and provide high accuracy over a much greater area. Images from optical satellite sensors such as Landsat or ASTER have been used to track visible surface features such as crevasses often present in fast flowing regions (Lucchitta and Ferguson, 1986; Bindschadler and Scambos, 1991; Stearns, 2011) and development of interferometric synthetic aperture radar (InSAR) has further reduced the uncertainties at which glacier flow speeds can be measured by providing additional information in the form of phase shift of the received signal between image pairs (Goldstein et al., 1993; Rignot et al., 2011b). The fringe patterns produced by InSAR may be unwrapped using ground information to give displacements to centimetre precision over periods of a few days and provide precision only possible with regular feature tracking over 1-2 years. Although in recent years InSAR and radar speckle tracking have largely replaced optical feature tracking, new GPS observations of non-linear tidal effects on velocity have called into question the reliability of using such short-interval repeats to infer annual trends (Gudmundsson, 2006).

1.6 Measurement of Ice Thickness in Antarctica

The other vital parameter for discharge calculations and assessment of melt rates is the ice thickness. Ice thickness on grounded ice has been calculated using ice-penetrating radar since the early 1960s (Evans, 1963), either from the ice surface or from the air (Gogineni et al., 1998). Seismic observations have also been used to measure ice thickness and the composition of the basal substrate (Anandakrishnan et al., 1998). The coverage for radar measurements of ice thickness is rapidly improving with widespread aerial surveys such as Operation IceBridge (Studinger et al., 2010; Fretwell et al., 2013) but is still poor where aerial surveys have not been flown, or only linear central flightlines are available. Thickness of ice shelves, on the other hand, can be obtained from altimeter-derived surface elevations, corrected for firn and ice density by assuming hydrostatic equilibrium (Griggs and Bamber, 2011). This hydrostatic equilibrium assumption is widely used to infer ice flux at

grounding lines and basal melt rates (Rignot, 2002) but small errors in surface elevation, geoid height or firn correction are amplified in the thickness calculations and error estimates are usually large. Close to the grounding zone where the thickness change is often greatest, ice is partially supported by the land and thickness estimates using this method can be inaccurate. While coverage using airborne radar is improving, there are still significant obstacles to implementing a spaceborne radar (Heliere et al., 2007) and alternative solutions for measuring ice thickness remotely must be examined.

1.7 Measurement of Basal Melting Beneath Ice Shelves

Melting at the base of ice shelves in Antarctica accounts for a large percentage of mass loss from the ice sheet. For the Ronne Ice Shelf, for example, Jenkins and Doake (1991) estimate 85% of the ice crossing the grounding line is lost by ablation before reaching the ice front. The rate of melting depends on how quickly heat and salt can be transported across the boundary layer at the ice-ocean interface, which in turn depends on turbulence, temperature and salinity gradients (Nicholls et al., 2009). Rignot and Jacobs (2002) observe a linear relationship between temperature and melt rate with 1°C effective temperature rise leading to approximately 10 ma^{-1} additional melting, while modelling supports a more quadratic response due to simultaneously increasing convection (Holland et al., 2008). Models of ocean circulation often do not accurately simulate basal melt rates due to a complex interaction between seasonal distribution of water masses and ocean temperature and unknown basal roughness (Hatterman et al., 2012). Nevertheless, from both modelling and observations, melt rates are generally highest close to the grounding line (Rignot and Jacobs, 2002; Holland, 2008), decreasing over a short distance and again higher than average close to the front of the ice shelf (Horgan et al., 2011).

Satellite techniques for melt rate calculations beneath ice shelves usually rely on the assumption that the ice is in hydrostatic equilibrium (e.g. Joughin and Padman, 2003; Wen, 2010) and that the horizontal flux divergence is balanced by the sum of surface accumulation/ablation and basal melting/freezing (Jenkins and Doake, 1991). Calculation of the flux divergence requires accurate measurement of surface velocity and surface accumulation, and calculation of ice thickness, which are then combined to derive values for discharge through flux gates on the ice shelf (e.g.

Neckel et al., 2012). Alternatively, melt rates have been calculated along linear flowlines where high quality airborne radar data are available using vertical strain rates derived from surface velocity fields (Bindschadler et al., 2011b). Melt rate calculations in the grounding zone are particularly difficult due to rapidly changing thickness and velocity gradients. They require high spatial resolution measurements and although various remote sensing techniques have been explored both geophysical (Smith, 1996; Corr et al., 2002; Jenkins et al., 2006; Catania et al., 2010; Pattyn et al., 2012a) and satellite based (Rignot, 2002), there are no current approaches which can be easily applied over large areas and which give reliable results. Values for melt rates at different locations are difficult to compare due to different methodological approaches and data availability. To properly analyse geographic distribution of melting and change in melt rates, a standardised method based on satellite data must be developed.

1.8 Thesis Structure

The main body of the thesis is arranged into 4 chapters which each broadly address the respective research objectives highlighted above. The chapters have been written for publication as peer-reviewed journal articles. These articles are presented verbatim as Chapters 2-5, with additional material included in chapter addenda or appendices where relevant. Chapter 6 links the thesis together with a description of how this combined work meets the outlined objectives. Full paper citations for each chapter, acknowledgements and publication status as of July 2013 are summarised below.

Chapter 2

Marsh, O.J. and W. Rack, 2012. A method of calculating ice-shelf surface velocity using ICESat altimetry, Polar Record, 48(244), 25-30, doi:10.1017/S0032247411000362. Publication status: received 05/12/10, accepted 10/06/11, published 29/11/11.

The work presented in this chapter explains a new method of calculating velocity over ice shelves, with particular emphasis on the grounding zone. High-precision ICESat altimetry is used to track surface undulations on an ice shelf for the first time, with observed displacements used to map ice velocity. Results are shown to

accurately represent velocities in the grounding zone of the Beardmore Glacier. By identifying the change in stress conditions associated with the grounding zone, this technique also provides a new method of grounding line identification. This novel technique of grounding line identification and mapping velocity fulfills the first of the aims listed in section 1.2. An addendum to the paper considers the application of this technique into two dimensions across the Ross Ice Shelf and its potential for further development.

Acknowledgements: ICESat data were provided by the National Snow and Ice Data Center (NSIDC) in Boulder, Colorado. ASTER data were provided within the GLIMS project.

Chapter 3

Marsh, O.J., W. Rack, D. Floricioiu, N.R. Golledge and W. Lawson, 2013. Tidally-induced velocity variations of the Beardmore Glacier, Antarctica, and their representation in satellite measurements of ice velocity, The Cryosphere Discuss, 7, 1761-1785, doi:10.5194/tcd-7-1761-2013. Publication status: The Cryosphere Discuss: received 08/04/13, accepted 22/04/13, published online 29/04/13. The Cryosphere: received 17/07/13, accepted 24/07/13.

The work presented in this chapter describes short-term velocity variations at the grounding zone of the Beardmore Glacier, recorded using ground-based GPS during the 2010-11 field season. The observed fluctuations are used to predict the velocity signal which should be visible in TerraSAR-X satellite velocity measurements. TerraSAR-X scenes from 2009-2012 are analysed to assess the contribution of tidal effects to measured velocity. Measurements from 2010-11 are also compared with geodetic measurements from 1960-61 to calculate long-term change at the Beardmore Glacier grounding line. This paper builds on earlier work looking at tidally-induced velocity change on the Ronne-Filchner ice shelf outlet glaciers and fulfills the second aim listed in section 1.2 by quantifying the influence of tides on satellite velocity measurements. The paper also describes a method of grounding line identification using speckle tracking which further develops the first objective.

Acknowledgements: TerraSAR-X data were provided by DLR from science proposal HYD1421. ASTER data were provided through the GLIMS project. Fieldwork on the Beardmore Glacier was supported by the US Antarctic Program, Antarc-

tica New Zealand Event K001BI and with assistance from Dean Arthur. Weather station data were provided by the UW-Madison AWS Program. This research was funded, in part, by the Ministry of Business, Innovation and Employment through research contract CO5X1001 to GNS Science. Comments by two anonymous reviewers led to revisions and improvement of the paper.

Chapter 4

Marsh, O.J., W. Rack, N.R. Golledge, W. Lawson and D. Floricioiu, 2013. Grounding zone ice thickness from InSAR: Inverse modelling of tidal elastic bending, Journal of Glaciology. Publication status: received 11/02/13, resubmitted 05/07/13

The work presented in this chapter addresses objective three from section 1.2 by developing a new satellite method of measuring ice thickness. This technique relies on high resolution vertical displacement information and describes an inversion of the Euler-Bernoulli equations for elastic plate bending and their application to the Beardmore Glacier grounding zone. It is shown how, when ice is modelled as an elastic medium, flexure information from differential InSAR may be used to derive ice stiffness and by application of an effective Young's Modulus this stiffness can be converted into a map of the spatial variability in ice thickness. Thickness calculated in this way agrees well with ground penetrating radar measurements for the area. This technique provides an alternative method of indirectly measuring ice thickness in Antarctic grounding zones using satellite.

Acknowledgements: The authors would like to thank Prof. Charles Swithinbank for information pertaining to the 1967 Beardmore RES data as well as Antarctic New Zealand Event K001B-Ice and Dean Arthur for field and logistical support. This research was funded, in part, by the Ministry of Business, Innovation and Employment through research contract CO5X1001 to GNS Science. TerraSAR-X data provided by DLR from science proposal HYD1421. ASTER data provided through the GLIMS project. Comments by two anonymous reviewers led to revisions and improvement of the paper.

Chapter 5

Marsh, O.J., W. Rack, W. Lawson, D. Floricioiu and N.R. Golledge,

2013. Spatial variability in ice discharge and basal melt rates in the grounding zones of Transantarctic Mountain outlet glaciers, Antarctic Science. Publication status: in preparation

This chapter provides high resolution velocity maps from TerraSAR-X speckle tracking for six outlet glaciers in the Transantarctic Mountains along with estimates of basal melt rates close to their grounding lines. The velocity measurements account for tidal effects and thickness estimates are standardised using a photogrammetrically derived digital elevation model corrected with ICESat data. 2012-13 estimates of velocity and discharge are compared to previous estimates from satellite and ground-based measurements. This chapter uses information from the previous chapters to address the fourth objective and produce a standardised comparison between ice discharges and melt rates along a latitudinal gradient in the Transantarctic Mountains.

Acknowledgements: TerraSAR-X data were provided by DLR from science proposal HYD1421. ASTER data were provided through the GLIMS project.

1.9 Data sources

The research objectives are addressed using a combination of multiple remote sensing satellite techniques, finite-element modelling, field validation and freely available datasets. Details of specific applications and development of the methods are provided in each chapter while a broad overview of the sources of data is outlined below. In order to provide Antarctic-wide applicability to the methods, it is necessary to use satellite remote sensing techniques with high spatial coverage. Synthetic aperture radar data are acquired using the TerraSAR-X satellite and laser altimetry using ICESat (Ice, Cloud and Land Elevation Satellite). Although often used in conjunction with other satellites, it is shown here that both of these satellites contain sensors capable of independently measuring the three key components of interest for grounding zone mass balance: grounding line position, ice velocity and ice thickness.

1.9.1 Altimetry

Satellite radar and lidar altimeters measure the distance between the satellite and the ground at nadir by identifying a precise location of the satellite orbit and record-

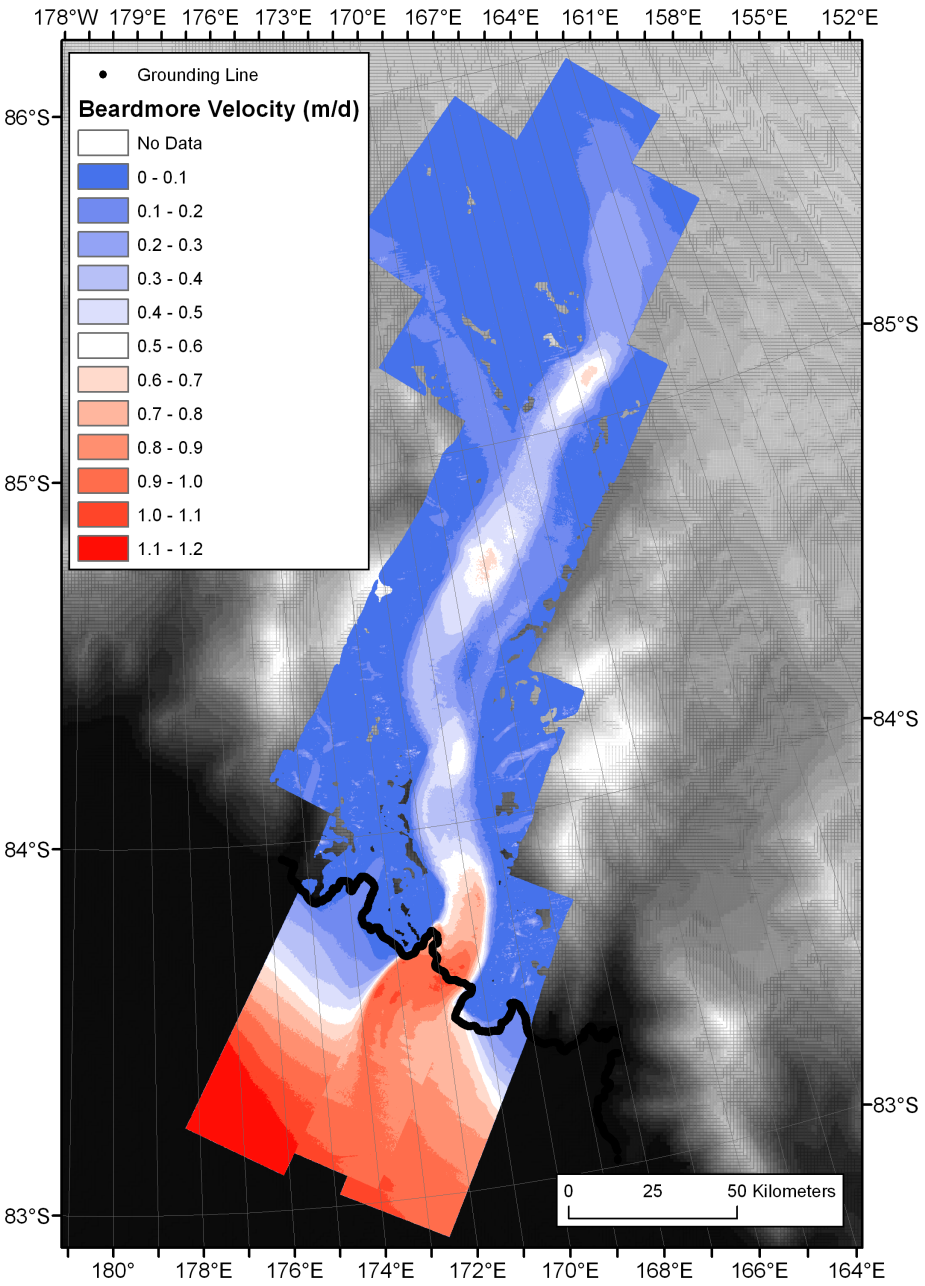

Figure 1.3: TerraSAR-X derived satellite map of the Beardmore Glacier. All maps are in WGS-84 Antarctic Polar Stereographic Projection with latitude of true scale at -71 °S.

ing the pointing angle and duration for an emitted electromagnetic pulse to be reflected at the surface and returned to the satellite. The primary altimeter used in this research is the Geoscience Laser Altimeter System (GLAS) onboard ICESat, a LIDAR emitting pulses of infrared and visible light at 1064 nm and 532 nm (Zwally et al., 2002). The GLAS lasers produced 70 m diameter surface footprints spaced every 170 m and for the main portion of the mission from 2004 to 2009 the satellite was in a 91-day repeating orbit. These data are used to identify the grounding line and to track the movement of surface undulations over floating ice (Chapter 2). ICESat data also produces high precision, accurate elevation point measurements which are used to calibrate the elevations from digital elevation models (Chapter 4).

1.9.2 Synthetic Aperture Radar

TerraSAR-X is an X-band SAR antenna which acquires phase and amplitude information with resolution of up to 3m in StripMap mode and high geometric accuracy. These data are used to measure surface movement: both the horizontal velocity component from single image pairs (Chapter 3); and vertical tidal flexure from double-difference image pairs (Chapter 4).

1.9.3 GPS Data

GPS measurements of horizontal and vertical motion were recorded on the glacier central flowlines of the Beardmore and Skelton Glaciers, in the grounding zone. The GPS data were processed using GIPSY precise point positioning algorithms (Zumberge et al., 1997). These GPS data allow georeferencing of satellite images and ground validation of satellite derived velocities, plus detailed information about short-term velocity variability (Chapter 3).

1.9.4 Ground-penetrating Radar

Ground-penetrating radar data were also collected in the field on the Beardmore Glacier. Clear basal reflectors on the ice shelf provide good independent information about ice thickness in the grounding zone. These thickness measurements are used to calibrate the effective Young's Modulus for ice stiffness in the grounding zone (Chapter 4). The radar data are processed using the ReflexW geophysical interpretation package.

1.9.5 Additional Datasets

Grounding line maps produced from digital elevation models and visible surface impression of the grounding zone (Bindschadler et al., 2011a), from interferometry (Rignot et al., 2011a) and from ICESat laser altimetry (Brunt et al., 2010a) are used in comparison with new methods of grounding line location. The Circumpolar Antarctic Tidal Simulation (CATS_2008opt) (Padman et al., 2008) is used to provide tidal amplitude information for investigating tidal variations in velocity (Chapter 3). The RAMP DEM (Liu et al., 2001) and ASTER GDEM v2 are used in addition to self-generated DEMs to provide surface elevation information for calculation of hydrostatic ice thickness. Thickness information from BEDMAP 2 (Fretwell et al., 2013) from previous calculations over ice shelves (Griggs and Bamber, 2011) and from airborne surveys from CReSIS (Gogineni, 2012) and archive data (Swithinbank, 1963) are also used for thickness estimation (Chapters 4 and 5).

Chapter II

A method of calculating ice-shelf surface velocity using ICESat altimetry

Very high precision satellite altimeter measurements from the Geoscience Laser Altimeter System onboard NASA's Ice, Cloud and land Elevation Satellite (ICESat) have allowed a method of feature tracking to be developed for floating ice which relies on recording the movement of large surface undulations. This method is applied to a section of the Ross Ice Shelf downstream of the grounding line of the Beardmore Glacier, Antarctica. The altimetry method has benefits over established optical and interferometric remote sensing techniques due to high pointing accuracy for geo-location, ability to deal with tidal fluctuations and to measure velocity where visible surface features are absent. Initial processing of a single sequence of ICESat tracks gives encouraging results for unidirectional ice flow with correlations between surface profiles in consecutive years exceeding 90% and producing high internal consistency in velocity between independent tracks. Velocities of 331 $\pm$ 28 m yr^{-1} near to the grounding line are also consistent with available ground measurements for the area.

2.1 Introduction

Ice shelves occupy almost 50% of the coastline of Antarctica and the majority of the continent's large outlet glaciers terminate in an ice shelf. The stability of marine ice sheets and flow rates of outlet glaciers is related to the thickness and extent of their surrounding ice shelves and margins. The collapse of ice shelves on the Antarctic Peninsula has been seen to immediately precede acceleration of tributary glaciers and thinning of ice further inland (Rott et al., 2002; Scambos et al., 2004). The buttressing effect of the ice shelves pinned against islands and ice-rises in the Ross, Weddell and Amundsen Seas protects the unstable West Antarctic Ice

Sheet from rapid collapse which could lead to a sea-level rise of approximately 3.3 m (Bamber et al., 2009). As well as being important for marine ice sheet stability, ice shelf velocity and thickness measurements can be used to predict inland changes by calculating variation in ice discharged across the grounding line. Variation in ice shelf extent, ice flux across the grounding line and contribution of melting and calving can be monitored by recording ice thickness and surface velocity. Four components of mass-balance are applicable to ice shelves: ice flux across the grounding line, melting/freezing at the ice-ocean interface, calving at the seaward margin and accumulation/ablation on the surface. Monitoring some of these components in combination with calculations of mass distribution, strain rate and flow patterns allows important inferences about accumulation patterns, sublimation and surface melt rates, ocean temperatures and internal ice dynamics to be made.

The aim of this study is to demonstrate the value of satellite altimetry as a method of calculating surface velocity over ice shelves. Airborne laser altimetry has been used previously to monitor ice movement in small areas and over short time periods on Jakobshavn Isbræ, Greenland (Abdalati and Krabill, 1999). This was achieved by densely scanning the glacier on different days and differencing the resulting digital elevation models. More recently terrestrial laser scanning has been used in the same area by placing the scanner on a hill overlooking the glacier (Schwalbe and Maas, 2009), but these techniques are unfeasible for large ice shelves in the Antarctic due to their low spatial coverage. Satellite-borne altimeters have not previously been used for velocity measurement over ice as they are unable to pick out small-scale features with large vertical impressions such as crevasses due to the large sensor footprint. Modern satellite altimeters have a high pointing accuracy, reasonably small footprints and high pulse rates, as well as accurate repeat pass orbits, which together allow the repeated mapping of relatively small and gentle surface undulations.

As very precise elevation measurements are needed over ice sheets to quantify their contribution to sea-level change (Pritchard et al., 2009), high precision satellite laser altimeters such as the Geoscience Laser Altimeter System (GLAS) aboard ICESat have been developed. This altimeter has a footprint size of around 70 metres meaning it can identify areas with large crevasses and rifts (Fricker et al., 2005). A vertical accuracy of around 3 cm over the poles also means that it can identify low-amplitude, long wavelength undulations in the ice (Zwally et al., 2002). This

accuracy has previously been used to map thinning (e.g. Smith et al., 2005; Csatho et al., 2005; Pritchard et al., 2009) as well as comparing the tidal signal beneath ice shelves with the non-tidal signal over grounded ice to pinpoint the grounding line (Brunt et al., 2010a).

To use the high vertical precision of altimetry to monitor horizontal movement requires firstly that features are sufficiently large to be detected by the altimeter and secondly that they move in the same direction and speed as the ice. Alberti and Biscaro (2010) show that ICESat can be used to detect decimetre-scale topography variation in snow megadunes in East Antarctica, so variations of this order should also be traceable over the ice shelf. When ice is grounded, the general shape of the surface of the ice depends on the shape of the bedrock, with bedrock protrusions and depressions often visible as surface bumps or hollows. These surface features do not move with the ice, rather the ice deforms around them. This has been used as a method of image co-registration where bedrock is not visible (e.g. Scambos et al., 1992). Small scale features such as surface crevasses may still be tracked over grounded ice with optical imagery or speckle and reflectance patterns from synthetic aperture radar (SAR). When the ice is floating however, any surface irregularities in the ice imprinted at the grounding line are transmitted downstream as there are no significant shear stresses to cause further deformation. Due to this difference in the movement and deformation of ice, the satellite altimetry technique described here is only applicable to floating ice where the movement of large scale features is synchronized with ice flow.

Currently, the most common methods of mapping ice shelf velocities involve cross-correlation of repeat-pass optical or SAR images, or radar interferometry (Rignot et al., 2008). Interferometry measures changes in phase of the return signal from SAR and relies on being able to maintain high phase coherence between images. This requires repeat acquisitions within a short time period and although accurate, is therefore limited in its applicability to many areas due to satellite coverage. SAR interferometry also suffers from tidal effects which make measuring velocity close to the grounding line difficult (Giles et al., 2009). Repeat-pass imagery allows features to be tracked on much longer time-scales with images separated by several years. High resolution optical or SAR sensors such as Landsat or Radarsat benefit from high accuracy in velocity measurements however they cover small areas. Individual images, particularly over ice shelves, will not always contain stationary points such

as rock outcrops, making co-registration difficult without stitching together multiple scenes. Low spatial resolution sensors such as MODIS (Moderate Resolution Imaging Spectroradiometer) suffer from reduced precision due to large pixel sizes (Haug et al., 2010) and passive optical sensors have a further disadvantage over altimetry in that they cannot acquire images during the polar winter when it is dark, or when there is cloud cover.

2.2 Mapping velocity using ICESat

The method of calculating surface velocity described here involves repeat-track analysis of laser altimetry data from the ICESat satellite. ICESat is a NASA satellite designed primarily for measuring ice surface heights, clouds and aerosols in the atmosphere. The uses of ICESat and an overview of its design brief are detailed elsewhere (Schutz et al., 2005). Its only scientific instrument is the Geoscience Laser Altimeter System (GLAS) which is a high precision LIDAR operating at wavelengths of 532 and 1064 nm. ICESat initially had a pointing accuracy of 7.5 m ± 6.6 m for Laser 3a (Magruder et al., 2005), giving a high confidence that the repeat data can be compared with minimal geolocational errors and the velocities obtained are well georeferenced. The altimeter acquires data to a latitudinal limit of 86 °S (Zwally et al., 2002), repeating each track between two and three times a year on a 91-day cycle. Altimetry data are sampled with 50-70 m diameter footprints every 0.025 seconds, giving an along track spacing of around 170 m (Schutz et al., 2005). The repetition of close to the same orbits and adjustment of the pointing angle up to 5°allows comparison between surface elevations at different times.

ICESat product GLA12 (GLAS Antarctic and Greenland Ice Sheet Altimetry Data), release 531, is used with acquisitions from October 2004 to October 2009. The elevation data are based on the TOPEX/Poseidon ellipsoid. The tidal correction applied to the data has been removed as it is likely to be inaccurate in the grounding zone where a tidal model had been applied based on a best estimation of the grounding line. As the grounding line is not known precisely for many areas of Antarctica, grounded ice may have been tidally corrected during pre-processing and areas which are floating may not. This could affect the slope, particularly where the grounding zone is poorly defined. A correction for signal saturation has also been applied as the high reflectance of the ice can affect the elevation value based on peak

return time of the laser pulse.

A small area of the Ross Ice Shelf downstream of the grounding line of the Beardmore Glacier is used to validate the technique (Figure 2.1). The data are interpolated to a regularly spaced 1 m grid using distance from a fixed point upstream, in line with the central track as an origin. The interpolation method is based on a smoothed cubic interpolation providing steady changes in surface slope whilst maintaining as much detail as possible (Figure 2.2a). Although the orbit path is broadly the same during each data acquisition period, the centre of the laser footprint is not always in the same place due to atmospheric affects and slight variation in the orientation, position or pointing angle of the satellite. The first derivate of elevation is used in favour of actual elevation to amplify differences in the ice profile between years. This conversion also removes the influence of tidal cycles on the correlation, producing a comparison between slope features (Figure 2.2b) rather than actual elevations (Figure 2.2a). As well as removing the effect of tides on the correlation, slope profile maintains a greater consistency over time and enhances the signal from feature peaks and troughs. Although undulations may decrease in amplitude over time due to spreading within the ice, the peaks and troughs stay in proportionally the same place.

Each pair of tracks are correlated separately using a stepped cross-correlation method with increasing lag applied to the second track. The point of maximum correlation between the two tracks is recorded (Figure 2.3). The amount of lag required in metres to obtain this maximum correlation represents the total movement of the ice in the along-track direction over the period between the two ICESat acquisitions. These values of ice movement are only used for further analysis if the correlation between the two profiles is greater than 0.75. This reduces the possibility of any coincidental correlations.

Although the ICESat tracks follow very similar paths, after post-processing the centre of the footprints can vary by up to 200 m across track (Table 2.1). This can cause the altimeter to record slightly different ice profiles, introducing some correlation errors. For identifying changes in grounded ice elevation this offset can be overcome by triangulating points on consecutive tracks (Pritchard et al., 2009). This is more difficult on floating ice due to changes in tide between acquisitions, although it could still be applied away from the grounding zone where the ice shelf moves consistently with tidal models and the elevations could be adjusted accordingly.

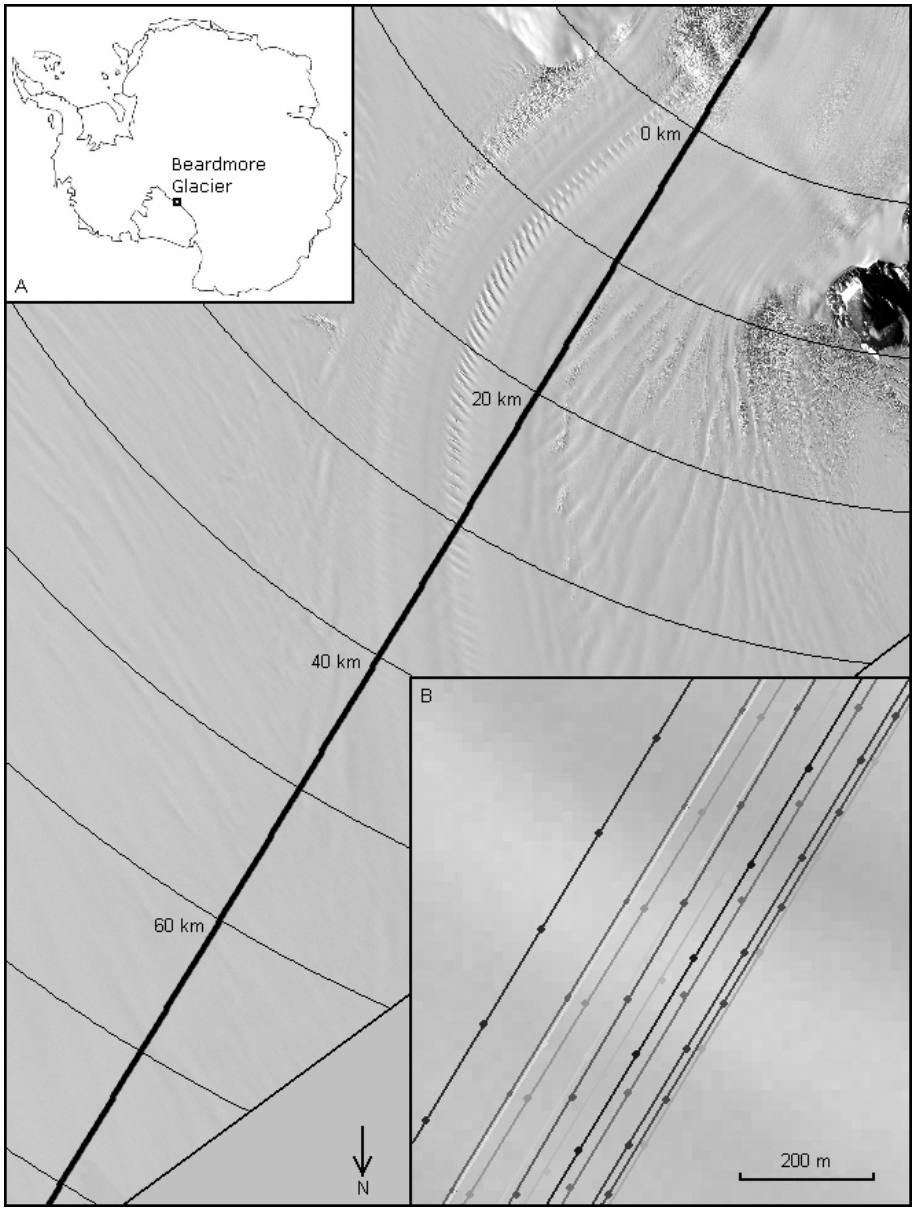

Figure 2.1: ASTER image of the Beardmore grounding zone showing the orbital path of ICESat. Inset a shows the location of the Beardmore Glacier on the Ross Ice Shelf. Inset b is a close up of the tracks showing the amount of offset from the mean.

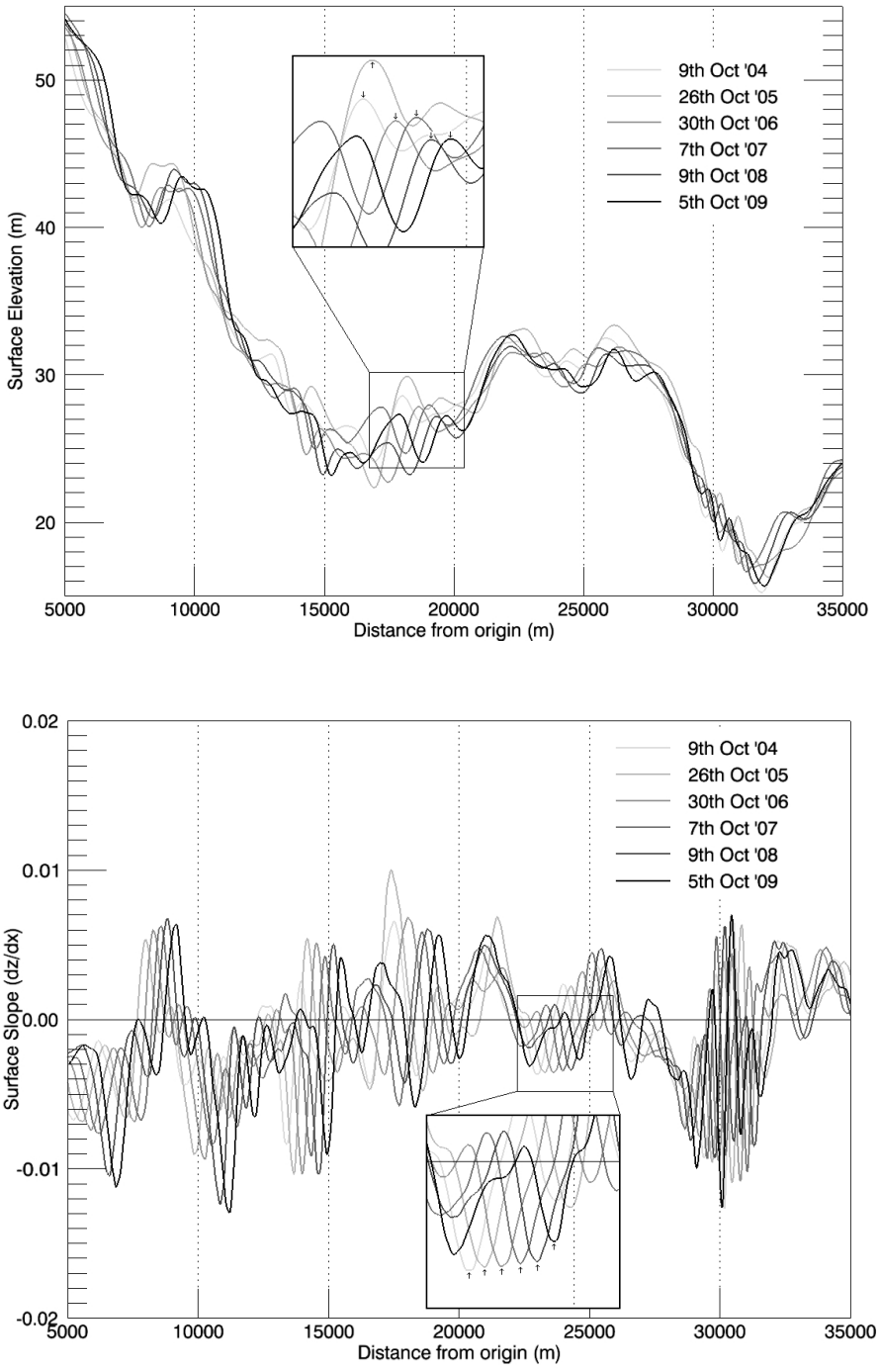

Figure 2.2: ICESat derived surface elevation for a 20 km section downstream of the grounding line (top) and along-track surface slope for the same section (bottom).

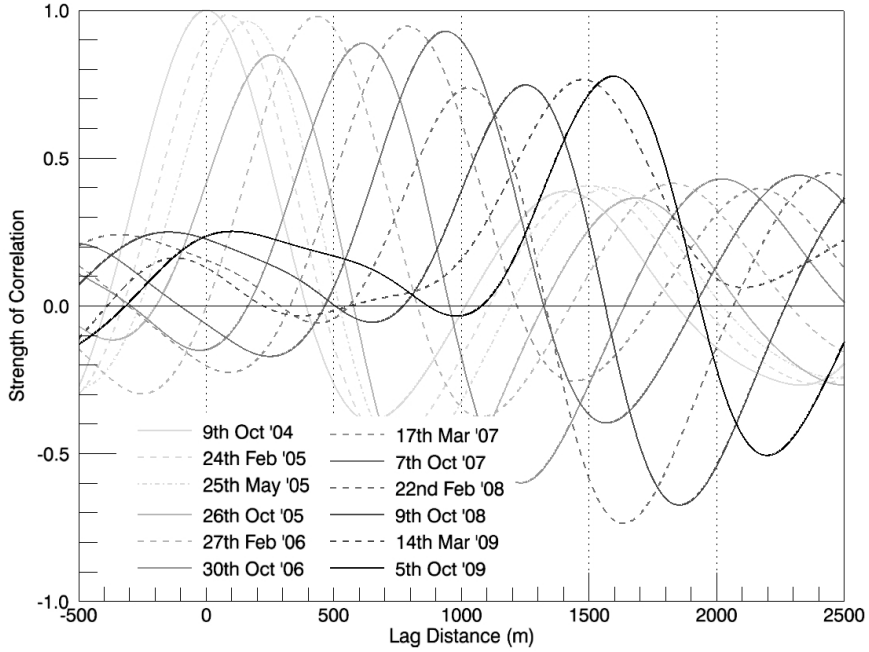

Figure 2.3: A comparison of the strength of correlation between the surface-slope profiles obtained during each track pass. All tracks are compared against track L3A (9th October '04).

This issue should be resolved with future altimeters (Abdalati et al., 2010) but currently an alternative method must be used to account for this offset which relies on simultaneous comparison of multiple tracks.

Where the features recorded by the altimeter are perpendicular to the satellite track, no adjustment needs to be made. Where the tracks pass over non-perpendicular features, an adjustment can be made by assuming a constant velocity between repeat passes. The adjustment for features is made using simple trigonometry (Figure 2.4) before the velocity is calculated. Depending on which way the features are orientated, the offset between tracks may form a greater or lesser contribution to the overall displacement. The feature-track angle (α) is unknown without combining the ICESat method with another sensor but can be approximated by a minimization routine if taken to be constant using data from all tracks as a series of simultaneous equations . This assumes features do not significantly change orientation between ICESat orbits. The amount of adjustment increases proportionally

Campaign ID	Date	Days after track L3A	Offset from mean (left positive, m)
L3A	9th Oct 2004	0	-98
L3B	24th Feb 2005	138	-24
L3C	25th May 2005	229	14
L3D	26th Oct 2005	383	123
L3E	27th Feb 2006	507	-61
L3G	30th Oct 2006	751	86
L3H	17th Mar 2007	889	-91
L3I	7th Oct 2007	1094	-14
L3J	22nd Feb 2008	1232	110
L3K	9th Oct 2008	1461	97
L2E	14th Mar 2009	1617	-178
L2F	6th Oct 2009	1823	40

Table 2.1: Details of the 12 overlapping ICESat tracks used for this study. 'Offset from mean' refers to the average lateral displacement of each track from its ideal path, calculated over the whole length of the track (see Figure 2.1, inset b)

to the inverse of the tangent of α (the angle between linear surface features and the satellite track). The features must not be parallel to the tracks or the error induced by the offset tends to infinity. If perpendicular then the offset can be ignored.

$$v\Delta t = \Delta x + \frac{\Delta y}{tan\alpha} \quad \alpha \neq 0 \tag{2.1}$$

where, v = flow velocity, x = feature location, y = perpendicular offset, t = acquisition time, α = angle between features and satellite track

The direction of flow of ice compared to the ICESat tracks can also influence the relative contribution of feature orientation and offset to the recorded velocity. Provided that the same large features are aligned in a constant direction between repeat passes, the effect of the offset can be removed if both the angle of flow and the feature angle are known. With this in mind, the net velocity can be calculated exactly if the two angles are known. Alternatively, if one of the angles is known the other can be deduced providing there are enough ICESat tracks of sufficient quality (generally greater than 4). This technique is more suitable for use at ICESat track crossing points where the velocity in two directions can be calculated and

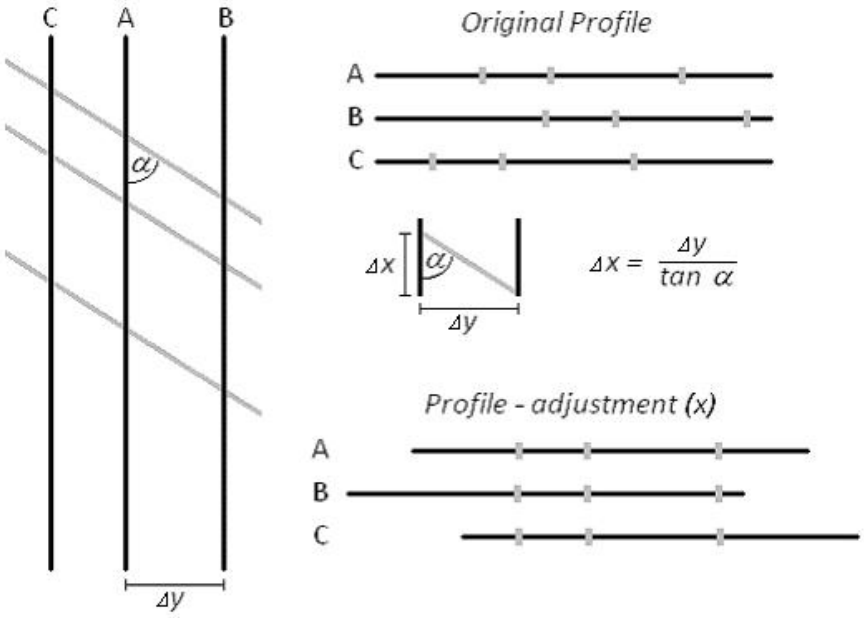

Figure 2.4: A schematic explanation of the method used to reduce the effect of oblique ice flow and irregularly orientated features. Black lines indicate ICESat tracks, grey lines indicate the orientation of surface features. The adjusted profile (bottom right) shows zero relative feature displacement due to cross-track separation.

therefore the angle between the tracks and the flow is already known. Three-value minimization of both angles and velocity for a single track leads to widely varying values of flow direction inconsistent with intuitive flow directions obtained from satellite imagery and was not adopted here.

2.3 Discussion

Figure 2.5 shows the offset-adjusted velocity recorded from each track pairing at 1 km intervals starting just above the grounding-line. The 5 km running mean is overlaid. The grounding line occurs between 3 and 4 km downstream of the specified origin indicated by a rapid increase in measured velocity. The peak in velocity occurs at 17 km from the origin where the ice flow is parallel to the ICESat track although there is also fast flow at the grounding-line. Both here and where the ice flow is parallel to the ICESat tracks at a point around 15 km downstream of the grounding

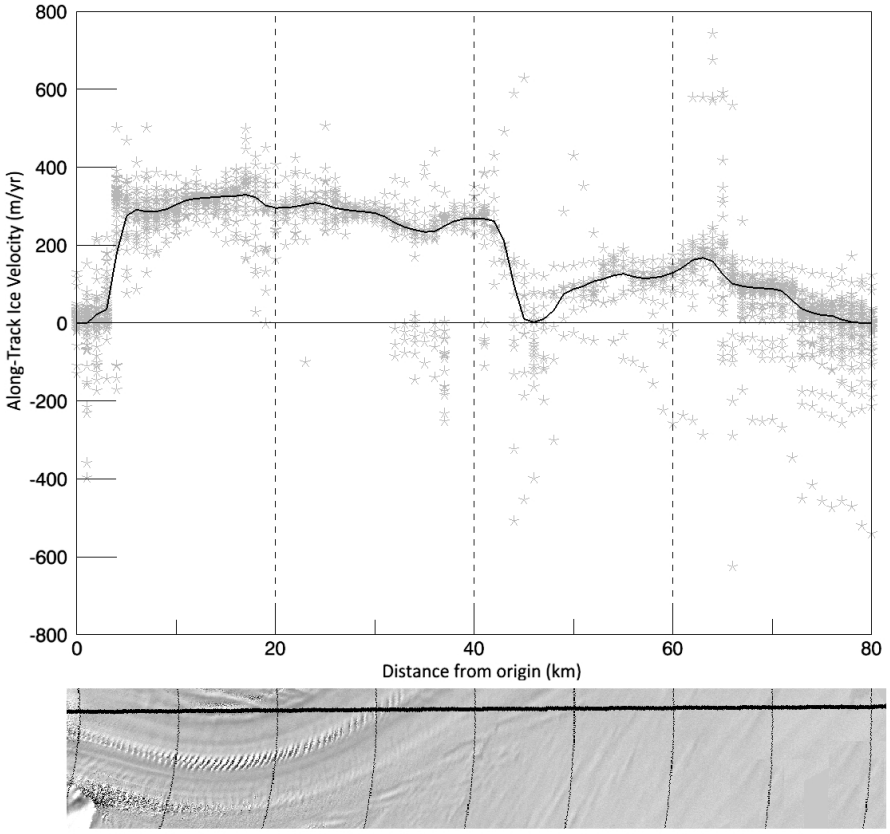

Figure 2.5: Along-track surface velocity for the 80 km downstream of the grounding line after adjustment for perpendicular offset.

line, the recorded velocities in the range 325-360 m a^{-1} are within 10% of currently published measurements for the glacier at its grounding line (Swithinbank, 1963). Calculated velocities along the whole section also show a high internal consistency, particularly where the offset between tracks is small. The two pairs of tracks which most closely overlap (repeating their footprint to within 10m), L3A - L3H and L3B - L3I, yield velocities of 365 m a^{-1} and 367 m a^{-1} respectively, at the grounding line. The recorded velocity drops sharply at around 40 km downstream of the grounding line. This represents the area of transition where ice originating from the Beardmore Glacier merges with slower ice already part of the ice shelf and the flow direction changes. This transition can also be seen in the ASTER imagery (Figure 2.5). Shearing in this zone disrupts the features being tracked, and fewer pairs of tracks

reach the correlation threshold for inclusion.

As the ice swings around to the north, approaching a perpendicular angle to the satellite tracks, the velocity in the along-track direction is reduced. To get a more accurate representation of the velocity in this area would require looking at tracks from a complimentary orbital path. The standard deviation of values in this area is also increased as errors in offset are multiplied by the rapidly increasing values of $(\tan \alpha^{-1})$. This increase in scatter of the velocities is also an indication that the quality of the results for the last 40km of the profile is lower than for the first 40km.

Although there is a reduction in velocity precision where the flow is not parallel to the satellite tracks, the tracked features are assumed to be stable along the whole profile. A comparison of tracks five years apart only produces marginally lower correlations than tracks one year apart (Figure 2.3). Features with similar amplitudes and wavelengths on the East Antarctic plateau have been interpreted as snow megadunes which migrate with the wind (Frezzotti et al., 2002) but these are unlikely to form on the ice shelf, as they appear to be caused by oscillations in katabatic winds in a stable, uniform wind environment. Smaller aeolian features such as sastrugi and wind scours which modify the ice surface are not resolved by the ICESat footprint but both accumulation rates and prevailing wind should be considered when tracking features over longer periods. The correlation between recorded profiles will decrease over time but atmospheric conditions should not destroy or fundamentally change the pattern of kilometre-scale undulations over the period involved.

The offset adjustment requires an assumption of constant velocity over the measured time-period. Fluctuations in surface velocity have been recorded on the nearby Byrd Glacier (Stearns et al., 2008) but these are thought to be caused by subglacial lake drainage. As no subglacial lakes have presently been documented in the Beardmore catchment (Siegert et al., 2005; Smith et al., 2009) and repeat ground measurements near the grounding line suggest that the velocity does not vary seasonally (Swithinbank, 1963), it seems reasonable to make the assumption of constant velocity over time periods of a few months for this glacier.

2.4 Conclusion

The single-track method described is useful when the track is parallel to ice flow but cannot be used as a standalone method as it produces values of ice movement in only one direction and the variance in measured velocity between tracks increases as flow becomes perpendicular to the tracks. In the Beardmore Glacier the ice flow direction can easily be inferred from ASTER imagery but further out on the ice shelf a combined track approach, or supplementary imagery is needed. The new technique described here is made possible by the high precision of modern satellite altimeters but is only applicable to floating ice where there is little surface deformation. The use of altimetry to measure ice shelf velocity is not meant to replace feature tracking using optical imagery or interferometry, it is designed to complement these techniques in areas where there are no ground control points or where image availability is limited. This is possible due to the high spatial coverage of altimetry data across Antarctica. The principles behind this method are currently being used to produce a 2-D velocity map of the entire ice shelf, by extending the simple version of the method presented here to multiple crossing tracks. The benefits of this technique over feature tracking by other satellite methods are the high accuracy of georeferencing, the availability of year-round, repeating data across Antarctica and the low computational expense in processing.

2.5 Addendum

Since submission in December 2010 and publication of this paper, the method described here has been further tested and developed for application to the entire Ross Ice Shelf. The method explained in reference to a single track can be applied to multiple tracks to create a 2D velocity map of absolute velocities and flow directions at points where ascending and descending orbit paths cross. Additional velocity data from the Beardmore Glacier grounding zone are also available from TerraSAR-X speckle tracking (Chapter 3) and the MEaSUREs dataset (Rignot et al., 2011b), against which these results may be compared. The velocity in along-track direction is within 5% of the MEaSUREs velocity between 8 and 42 km from the grounding line (Figure 2.5). Across this section the angle between velocity direction and track direction is between -14 °and 33 °. As the angle increases further towards 49 °at 80

km, the quality of velocity measurements significantly decreases.

ICESat data for the entire ice shelf have been batch processed in stages, in code written in IDL. ICESat orbital crossing points are identified by searching for regions with high point density and where there is coverage by multiple ICESat orbit campaigns in both ascending and descending directions. For the Ross Ice Shelf there are 743 potential orbit paths between 154 °W and 158 °E with greater than 10,000 possible crossing points. The high spatial density of ICESat track crossing points on the southern Ross Ice Shelf increases the spatial resolution of this technique in this area with separation of between 5 and 10 km at 83 °S. Data is extracted at each crossing point and tracks grouped by ascending and descending orbits. The method described in Section 2.3 is applied separately to all ascending tracks and all descending tracks.

Although this method only records flow in an along-track direction, where ascending and descending orbit paths are well separated the two velocities can be combined to produce a real ground displacement, similar to the approach used with SAR interferometry in two directions (Joughin et al., 1998). The calculated velocities along each track represent a component of the velocity in a non-orthonormal coordinate system and must be transformed into xy coordinates to produce an output velocity vector. The coordinate system transformation is done using the following equation:

$$\begin{bmatrix} v_x \\ v_y \end{bmatrix} = \mathbf{AB} \begin{bmatrix} v_a \hat{\mathbf{a}} \\ v_d \hat{\mathbf{d}} \end{bmatrix}$$

where

$$\mathbf{A} = \begin{bmatrix} cos\beta & cos(\alpha+\beta) \\ sin\beta & sin(\alpha+\beta) \end{bmatrix}$$

and

$$\mathbf{B} = \left(\frac{1}{sin^2\alpha}\right) \begin{bmatrix} 1 & -cos\alpha \\ -cos\alpha & 1 \end{bmatrix}$$

where $\hat{\mathbf{a}}$ and $\hat{\mathbf{d}}$ are unit vectors in ascending track and descending track direction; v_x and v_y are velocity components in x and y directions; v_a and v_d are velocity components in ascending and descending track directions; α is the angle between the ascending track and the x-axis; and β is the angle between the two tracks.

Data are interpolated from all crossing points where velocities in x and y pass quality checks on number of campaigns, strength of correlation between tracks and variability in velocity between track pairs. A velocity map produced for the Ross Ice Shelf using this method is shown in Figure 2.6a in comparison with a map from the Ross Ice Shelf Geophysical and Glaciology Survey (RIGGS, Figure 2.6b).

This velocity map replicates the ground-measured interpolated velocity to within 50 ma^{-1} over much of the ice shelf but suffers from high errors and consequent loss of data in some regions. These errors are caused by the inexact repeat of the ground-track location for ICESat and loss of correlation where the angle between ice flow direction and satellite flight direction is greater than $\sim$35-45 °. Lower amplitude of surface undulations towards the northern margin of the ice shelf also produces maximum correlation coefficients below the threshold value of 0.7 set for this run, yielding no results in this region. Figure 2.6c.

Since publication of this paper, the concept of using ICESat altimetry for feature tracking has been further adapted by Lee et al. (2012) in their paper 'Ice velocity mapping of Ross Ice Shelf, Antarctica by matching surface undulations measured by ICESat laser altimetry', where elevations are transformed into time-varying coordinate system using InSAR-derived initial estimates of velocity. The method described by Lee et al. (2012) produces a better spatial coverage by analysing crossing points in parallel rather than separately for ascending and descending tracks and produces a more smoothly varying velocity map in 2D for the Ross Ice Shelf with stated error estimates of only 8 ma^{-1}. This does not yet replicate the precision available for InSAR measurements (Mouginot et al., 2012), but these studies show that mapping surface velocity using satellite altimetry will be possible at high resolution in the future with sensors such as ICESat-2 (Abdalati et al., 2010) and will have significant potential as a calibration and verification tool for optical or radar measurements.

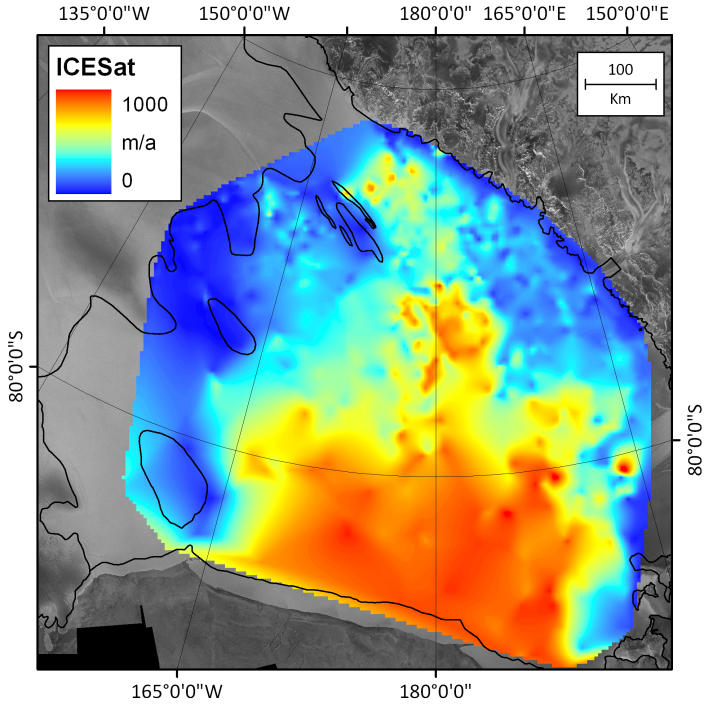
135°0'0"W
150°0'0"W
180°0'0"
165°0'0"E
150°0'0"E
ICESat
1000
m/a
0
100
Km
80°0'0"S
80°0'0"S
165°0'0"W
180°0'0"

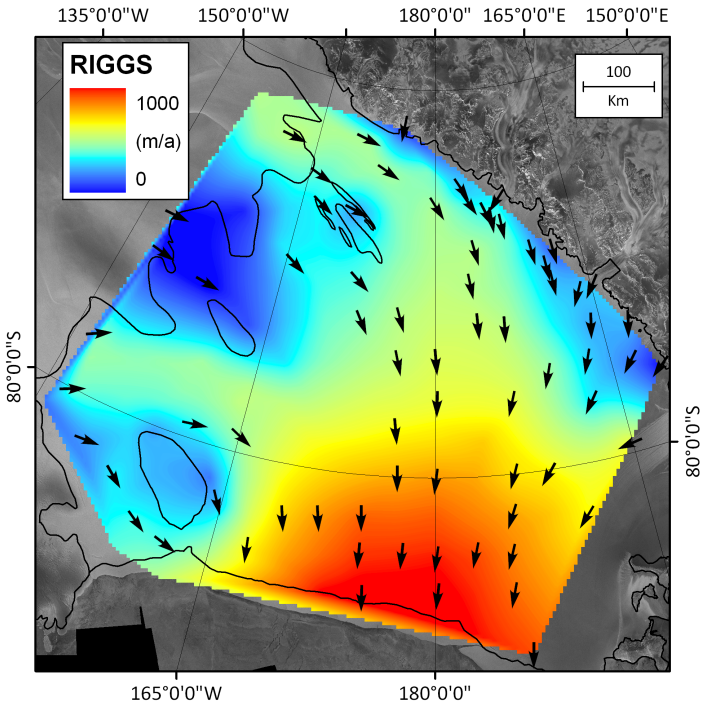
135°0'0"W
150°0'0"W
180°0'0"
165°0'0"E
150°0'0"E
RIGGS
1000
(m/a)
0
100
Km
80°0'0"S
80°0'0"S
165°0'0"W
180°0'0"

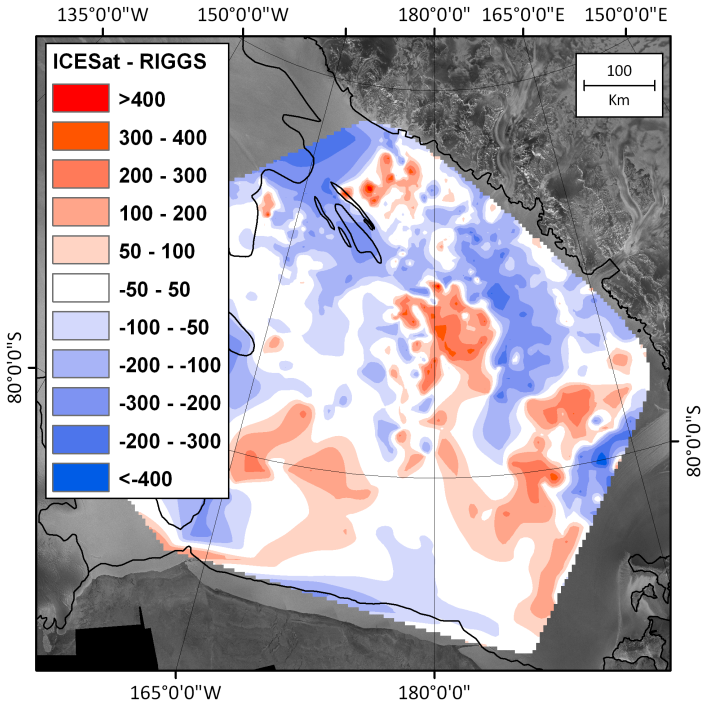

Figure 2.6: a) Velocity data for the Ross Ice Shelf from ICESat feature tracking, b) Ground based velocity data for the Ross Ice Shelf from RIGGS (Thomas et al., 1984) and c) Difference map between ICESat and RIGGS.

Chapter III

Tidally-induced velocity variations of the Beardmore Glacier, Antarctica, and their representation in satellite measurements of ice velocity

Ocean tides close to the grounding line of outlet glaciers around Antarctica have been shown to directly influence ice velocity, both linearly and non-linearly. These fluctuations can be significant and have the potential to affect satellite measurements of ice discharge, which assume displacement between satellite passes to be consistent and representative of annual means. Satellite observations of horizontal velocity variation in the grounding zone are also contaminated by vertical tidal effects, the importance of which is highlighted here in speckle tracking measurements. Eight TerraSAR-X scenes from the grounding zone of the Beardmore Glacier are analysed in conjunction with GPS measurements to determine short-term and decadal trends in ice velocity. Diurnal tides produce horizontal velocity fluctuations of $> 50\%$ on the ice shelf, recorded in the GPS data 4 km downstream of the grounding line. This variability decreases rapidly to $< 5\%$ only 15 km upstream of the grounding line. Daily fluctuations are smoothed to $< 1\%$ in the 11-day repeat pass TerraSAR-X imagery but fortnightly variations over this period are still visible and show that satellite-velocity measurements can be affected by tides over longer periods. The measured tidal displacement observed in radar look direction over floating ice also allows the grounding line to be identified, using differential speckle tracking where phase information cannot be easily unwrapped.

3.1 Introduction

The Antarctic Ice Sheet contains approximately 27,000,000 Gt (10^{12} kg) of ice (Fretwell et al., 2013). Recent estimates suggest around 2,000 Gt or 0.01% of this

ice moves through the system every year (Rignot et al., 2008), which is a volume equivalent to around 5 mm per year of global sea level rise. It is clear that even a small imbalance between inputs and outputs could cause a rapid change in global sea level. Accurate methods of identifying ice discharge around the perimeter of Antarctica are necessary to quantify the mass-balance of individual glaciers and allow modelling of current and future contribution of the ice sheets to sea-level rise. Discharge of outlet glaciers is typically calculated at the grounding line where ice becomes floating and before it moves into a regime of net negative mass-balance on the ice shelf influenced by significantly enhanced basal melting (Rignot, 2002).

Frequent measurement of surface displacement allows observation of dynamic changes in glacier velocity. The velocity of ice streams and outlet glaciers terminating in ice shelves has been shown to fluctuate in response to ocean tides (e.g. Anandakrishnan et al., 2003; Bindschadler et al., 2003; Gudmundsson, 2006) and when analysing long-term trends it is important not to include bias from these short-term, unrepresentative velocity variations, or misuse a velocity 'snapshot' taken over a few days to calculate an annual average ice discharge (Doake et al., 2002; Joughin et al., 2005; Gudmundsson, 2006). The frequency and amplitude of the tidally-induced response varies with location, with velocity increases between 100 and 300% of the mean recorded near the calving margins of large ice shelves (Brunt et al., 2010b; Makinson et al., 2012) and smaller variations recorded tens of kilometres upstream of the grounding line on fast flowing ice streams (Gudmundsson, 2006). Variations close to the grounding line have been linked to pertubation in basal shear stress (Bindschadler et al., 2003; Anandakrishnan et al., 2003) but it is not yet clear how longitudinal stresses are transmitted within the ice shelf (Brunt et al., 2010b). Velocity also varies differently depending on the strength of tidal components, with a non-linear response of velocity associated with the semi-diurnal tides (King et al., 2010) and more regular response to diurnal tides (Bindschadler et al., 2003).

A full understanding of the drivers of this velocity fluctuation is of particular importance when annual velocity patterns are calculated using Interferometric Synthetic Aperture Radar (InSAR) or other satellite measurements of surface displacement calculated over short intervals (Gudmundsson, 2006). In the last two decades InSAR has become a standard way of measuring ice sheet surface velocities remotely (Goldstein et al., 1993; Rignot, 1996; Rignot et al., 2008). This technique relies on the satellite acquisitions being separated by a short time interval in order

that snowfall events or other changes in the surface do not reduce the interferometric coherence. For spaceborne InSAR, repeat pass acquisitions are typically separated by several days to weeks depending on the repeat cycle of the satellite. Here we use velocity data from GPSs at points upstream and downstream of the grounding line to quantify the temporal variability in velocity in the grounding zone, both on daily timescales and over the last 50 years. Using these data in combination with a tide model (Padman et al., 2008) and glacier response model (Gudmundsson, 2007), we extend the measured GPS time series and predict how these variations will be visible from satellite speckle tracking. Synthesised velocities are compared with real satellite acquisitions and used to make inferences about the spatial extent of short-term velocity changes observed at GPS points and their propagation upstream of the grounding line.

TerraSAR-X and ground-based velocity measurements are presented for Beardmore Glacier, an outlet glacier in the Transantarctic Mountains, Antarctica. The high accuracy of TerraSAR-X speckle tracking also allows a method of grounding line identification using techniques similar to differential interferometry (Goldstein et al., 1993; Rignot et al., 2011a) but possible where phase coherence is not necessarily continuous or fringes are too densely spaced to be unwrapped (Joughin et al., 2010).

3.2 The Beardmore Glacier

The glaciers which flow through the Transantarctic Mountains provide an important link between the West Antarctic and East Antarctic Ice Sheets and understanding their flow and variability is important for monitoring how mass-balance changes can be transmitted across the ice sheet. The Beardmore Glacier ($83.5°S, 172°E$) drains a catchment of around 90,000 km^2 from East Antarctica into the Ross Ice Shelf (Fig. 3.1). The glacier flows steeply through the Transantarctic Mountains with a well-defined break of slope where it meets the ice shelf, between Mount Hope and Mount Kyffin and is around 25 km wide at this point. Previous measurements of the Beardmore Glacier are limited due to its high latitude and inaccessibility. A velocity of 364.7 ± 1.5 ma^{-1} (0.998 ± 0.004 md^{-1}) was calculated for the Beardmore in 1960-61 by measuring stakes over a period of close to 1 year on the central flowline of the glacier close to the grounding line (Swithinbank, 1963) with a coincident

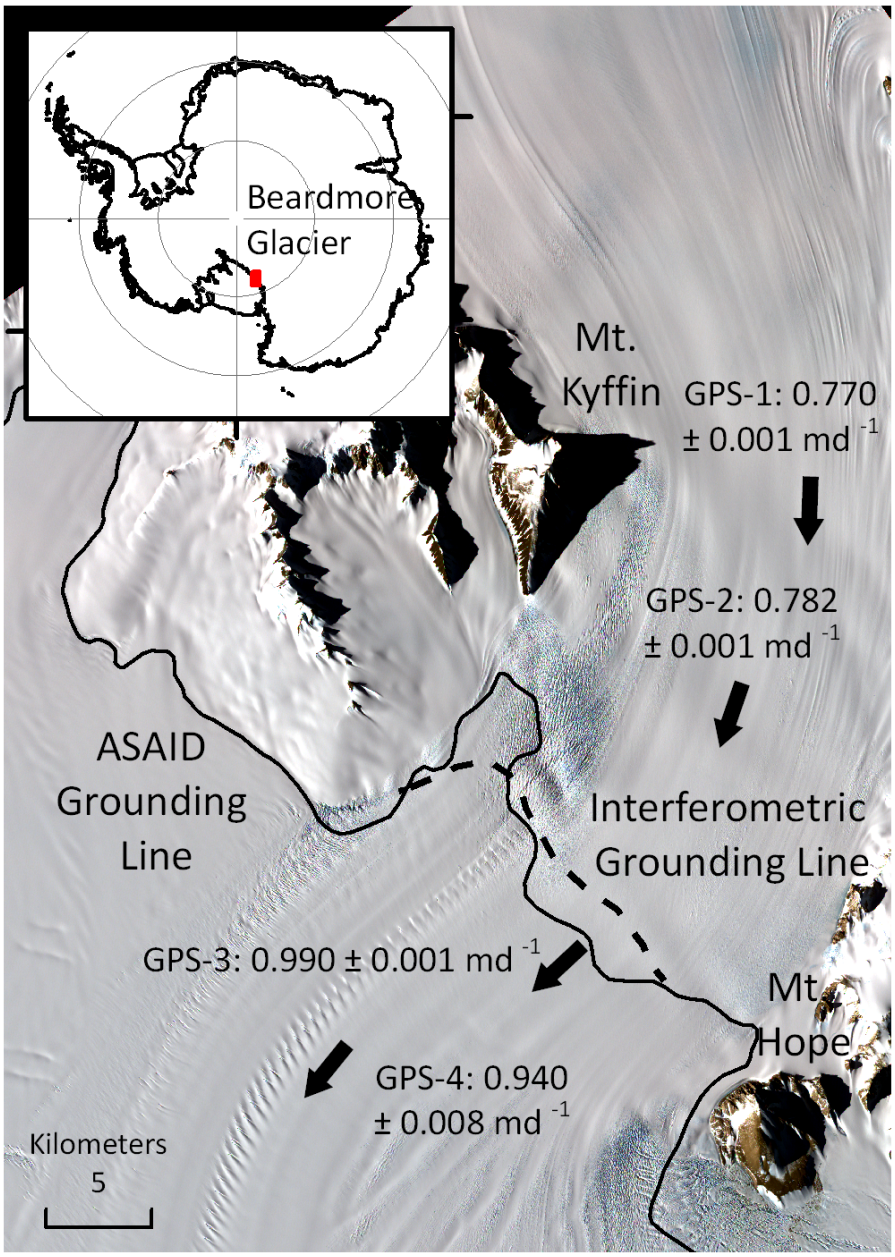

Figure 3.1: Beardmore Glacier GPS positions and velocities in December 2010 superimposed on an ASTER image from 2008. GPS positions correspond to the centres of arrows. The ASAID (solid line) and Interferometric (dashed line) grounding lines are also shown.

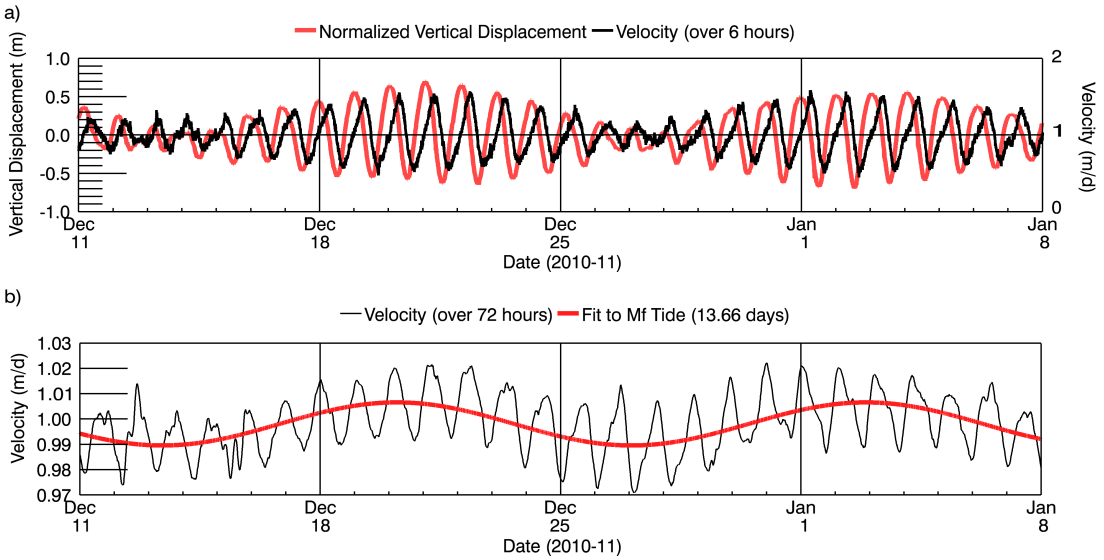

Figure 3.2: **a)** Recorded vertical displacement and 6-hour averaged surface velocity at GPS-3. Peaks in velocity match closely to peak rate of falling tide both in phase and amplitude. **b)** 3-day running average velocity at the Beardmore grounding line from GPS data. Velocities show the outcome of 3-day repeat feature tracking. Short-term velocities throughout the paper are given in md^{-1} instead of ma^{-1}.

measurement over 14 days during the summer agreeing with these results to within 2% (the limit of detection), and suggesting limited seasonal variability at this time.

The grounding line of the Beardmore is defined here using two methods; photoclinometrically to identify a surface impression of change in stress regime, and interferometrically identifying the landward limit of tidal flexure (Fig. 3.1). A photoclinometric grounding line is available from the ASAID full Antarctic grounding line map (Bindschadler et al., 2011a) but no published landward limit of tidal flexure is available for this area. This was instead derived manually from a combination of TerraSAR-X differential interferograms (2012) and ICESat data (2003-2009) for the area. The two grounding lines differ by less than 2 km and where ICESat tracks cross the grounding line, data from Brunt et al. (2010a) using flexure information and Marsh et al. (2012) using break of slope and surface deformation distribution also agrees well with these grounding lines.

3.3 GPS Measurements

GPS measurements are used to provide high temporal resolution information on glacier velocity. Four GPS stations (1 to 4) were positioned on the centreline of the glacier at 20 km and 10 km upstream and 4 km and 15 km downstream of the grounding line. GPS-3 was positioned on the coordinates of the 1960-61 measurement in the grounding zone by Swithinbank (1963). Data at all sites were recorded at 15 second intervals over a 35-day period, although data are not continuous at some of the sites. These data have been processed using kinematic Precise Point Positioning algorithms in JPL's GIPSY software (Zumberge et al., 1997; King, 2004). Effects of ionospheric and tropospheric delay are reduced by kinematic processing under loose random-walk constraints although some precision is lost in comparison to static occupation methods (e.g. King et al., 2000). Locational accuracy from this method is nominally between 1.5 and 2.5 cm. Care was taken in resolving ambiguities in horizontal and vertical velocities to avoid errors in horizontal measurements due to unmodelled vertical signals (King, 2004). Point velocities are calculated based on differencing the positions over time intervals of 6 hours. This smoothes out high frequency noise associated with the coordinate location errors and any unmodelled higher harmonic tides. A comparison between GPS measured velocity and vertical movement at GPS-3 is given in Fig. 3.2a. Local maxima in velocity in the grounding zone coincide with maximum rate of falling tide, which is in agreement with elastic flexure theory which predicts a longitudinal extension at the surface during low tide (Holdsworth, 1969). At GPS-3, 6-hour mean velocities vary between 0.5 md^{-1} and 1.5 md^{-1} during spring tides.

3.4 TerraSAR-X Speckle Tracking

TerraSAR-X data are used to provide information on spatial variability of glacier velocity. Speckle tracking makes use of the high pixel noise inherent in coherent imaging systems such as SAR. Speckle tracking can be used to map displacement vectors over short periods but unlike optical feature tracking it does not require large scale features such as crevasses. This method can be applied where surface displacement is relatively large and phase coherence is not completely lost. Current and recent InSAR and speckle tracking calculations have used consecutive repeat

pass acquisitions of the available spaceborne SAR missions with various repeat cycles, e.g. 1-day repeats, for instance with ERS-1/-2 in tandem mode (e.g. Joughin et al., 1996; Burgess et al., 2005); 3-day repeats such as with ERS-1 repeat pass acquisitions during the ice phase (e.g. Kwok and Fahnestock, 1996); 11-day repeats such as with TerraSAR-X (Jezek et al., 2011); 24-day repeats as with the Radarsat-1 (Scheuchl et al., 2012); and 46-day repeats with ALOS PALSAR (Baessler et al., 2012).

For the Beardmore Glacier grounding zone, eight TerraSAR-X scenes with 11-day separation have been acquired in StripMap mode: two sets of triples in March and June 2012 and an image pair in December 2009 (Table 3.1). Calculating displacement between these images allows five temporally distinct measurements of velocity. At $83.5°S$ the data are acquired in left-looking mode on a descending orbit and processed to single-look slant-range complex (SSC) format by DLR (Breit et al., 2010). A scene centre incidence angle of 44°gives range pixel resolution of 2.5 m and azimuth resolution of 3.3 m for these scenes. TerraSAR-X scenes over the Beardmore are acquired with the radar look direction aligned approximately perpendicular to the main component of ice flow. Velocities are calculated from full resolution SSC data by speckle amplitude tracking simultaneously in range and azimuth direction, which largely avoids coherence problems in fast flowing areas and shear zones but provides sub-pixel resolution (Joughin, 2002). Co-registration of image pairs is done by masking out moving areas on the glacier and ice shelf, and calculating a base offset between images for the remaining areas. The slave image is then shifted to match this offset and produce a zero velocity over non-moving areas. Patches between 64 and 512 pixels square were tested for cross-correlation and a 256^2 pixel patch used for final matching, producing a high signal to noise ratio but minimum loss of spatial resolution. Correlations with poor signal-to-noise ratio are discarded. An oversampling factor is applied to increase the precision of correlation. Jezek et al. (2011) estimate an absolute error for TerraSAR-X imagery of 0.03 md^{-1} from atmospheric path delay and solid earth tide effects. Relative velocity errors depend on patch size and shape of the correlation function but are here minimised due to large patch sizes.

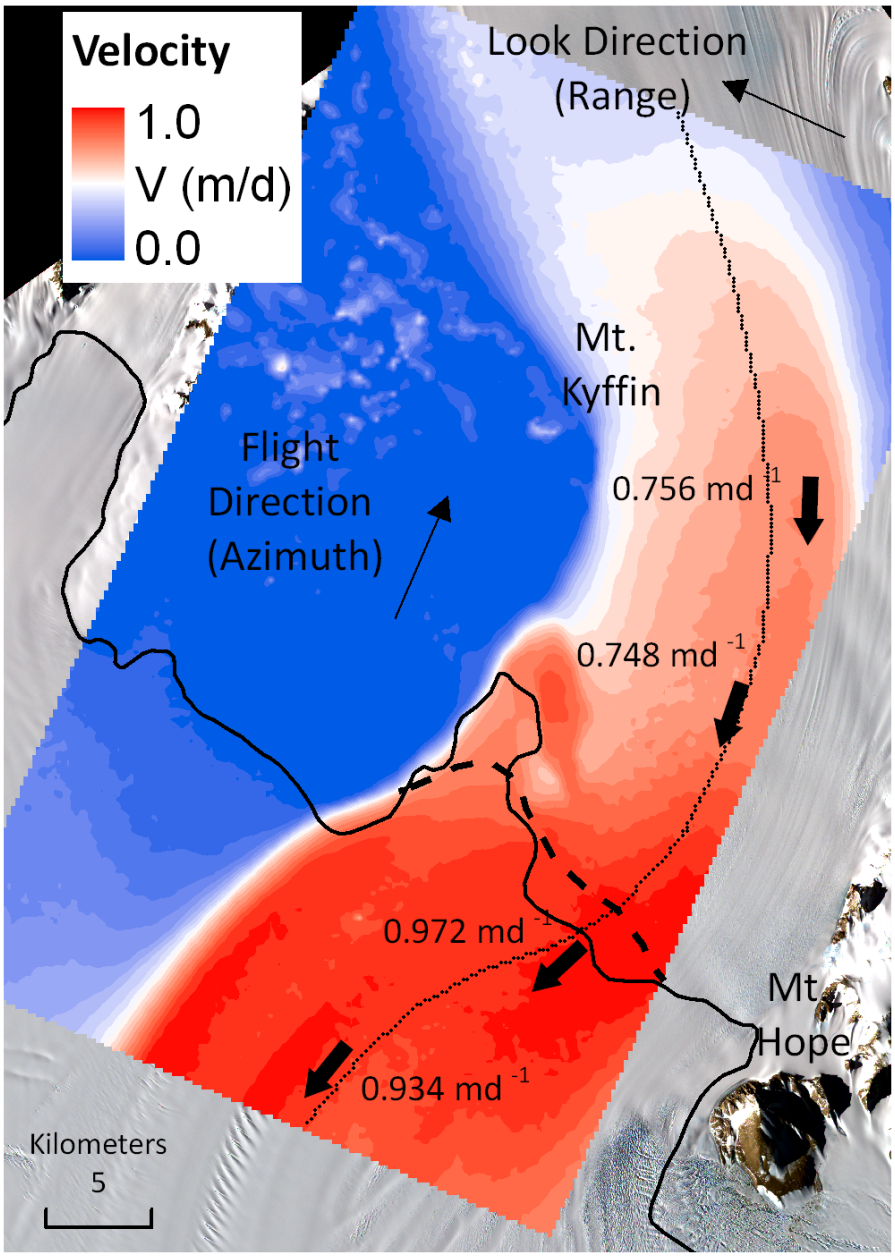

Figure 3.3: Absolute velocity across the Beardmore Glacier grounding line created by stacking velocity data from Dec-1/2, Jun-1/2 and Jun-2/3. Velocity arrows show TerraSAR-X velocities at GPS points for comparison with Fig. 3.1.

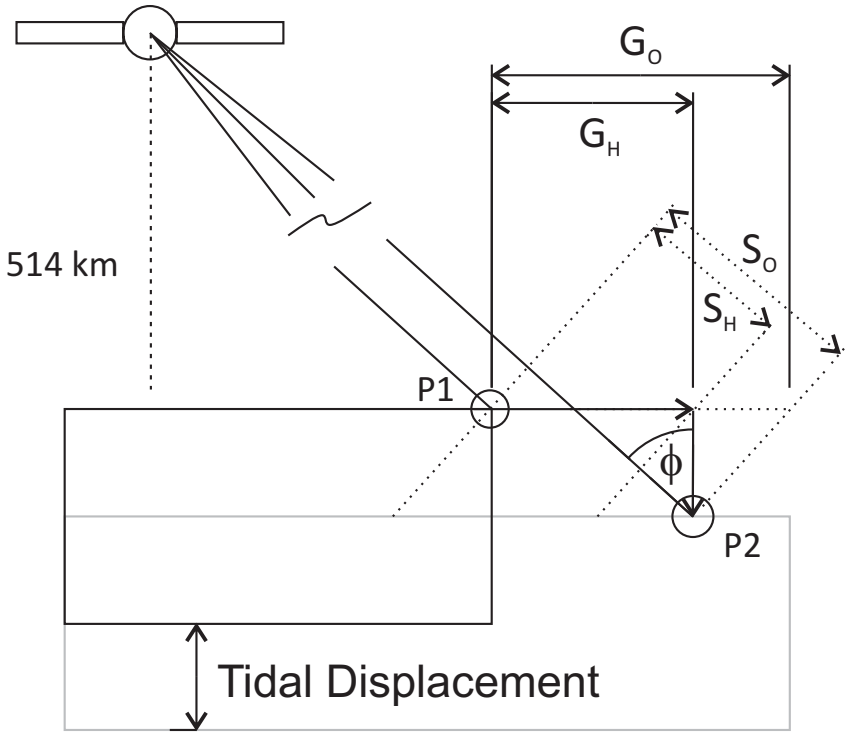

Figure 3.4: Schematic showing the effect of tidal displacement on observed displacement in slant range (S_O) and ground range (G_O) compared to actual horizontal displacement (G_H). When slant range is converted into ground range the additional displacement equals the tidal change divided by the tangent of the incidence angle ($S = T/\tan(\phi)$).

Table 3.1: Modelled tidal height above mean sea level and inverse barometer effect derived from atmospheric pressure at 'Elaine' weather station for individual TerraSAR-X acquisition dates.

TSX ID	Date	Tide (m) (CATS_2008opt)	Atmospheric Pressure (hPa)	Inverse Barometer Effect (m)
Dec-1	16/12/09	0.606	982.5∗	-0.175
Dec-2	27/12/09	0.024	981.7∗	-0.183
Mar-1	20/03/12	0.271	982.0	-0.180
Mar-2	31/03/12	-0.198	990.3	-0.097
Mar-3	11/04/12	-0.684	981.2	-0.188
Jun-1	05/06/12	-0.596	972.3	-0.277
Jun-2	16/06/12	-0.116	985.2	-0.142
Jun-3	27/06/12	-0.019	998.2	-0.018

∗ data from 'Lettau' station $(83.1°S, 174°E)$

Table 3.2: Predicted absolute mean glacier velocity at GPS-3 (V) for TerraSAR-X acquisition periods from tidal response modelling and expected tidal (V_t) and atmospheric (V_{IBE}) induced-error in observed radar look-direction velocity due to vertical displacement.

TSX Pairs	Δ Tide (m)	V_t (md^{-1})	Δ IBE (m)	V_{IBE} (md^{-1})	V (md^{-1})
Dec-1/2	-0.581	+0.052	-0.008	+0.001	1.003
Mar-1/2	-0.469	+0.042	+0.083	-0.008	0.973
Mar-2/3	-0.486	+0.044	-0.091	+0.008	0.979
Jun-1/2	0.480	-0.043	+0.135	-0.012	0.992
Jun-2/3	0.0970	-0.009	+0.124	-0.011	0.997

3.5 Ice Velocity Results

Averaged GPS data from December 2010 shows a 1% decrease in velocity at the grounding line of the Beardmore Glacier over the 50-year period since 1960-61 from 0.998 ± 0.004 md^{-1} to 0.990 ± 0.001 md^{-1}. This difference is greater than the combined error estimates given for the 1960-61 and 2010-11 data but suggests that discharge from this glacier has likely not changed significantly over the last fifty years (Swithinbank, 1963) in contrast to glaciers elsewhere in Antarctica. A stacked velocity map using data from three pairs of TerraSAR-X data gives a smoothed spatial velocity over three 11-day periods (Fig. 3.3). Comparison between TerraSAR-X

derived velocities and GPS velocities highlights the absolute error in the TerraSAR-X data. TerraSAR-X and GPS velocities respectively in md^{-1} at GPS-1 are 0.756 and 0.770; at GPS-2 are 0.748 and 0.782; at GPS-3 are 0.972 and 0.990; and at GPS-4 are 0.934 and 0.940. This shows agreement within 5% at all sites and $< 2\%$ at all but one site, supporting estimates of TerraSAR-X error of around 0.03 md^{-1}.

3.6 Grounding Line Identification

Although the effect of tides becomes progressively less important with longer repeat pass intervals and speckle tracking has previously been used to infer a horizontal velocity independent of tidal interference (e.g. Baessler et al., 2012), with high resolution sensors such as TerraSAR-X the quality of speckle tracking velocity measurements is high enough that vertical tidal effects are clearly observed in radar range and when not removed can introduce a large bias in horizontal velocity. At an incidence angle of 44°, a 1 m change in tide between satellite passes produces a 1.036 m error in the horizontal displacement which translates to approximately 0.094 md^{-1} error in velocity in look direction over the 11-day repeat pass interval of TerraSAR-X (Fig. 3.4). This is significant for many outlet glaciers and ice streams surrounding Antarctica, particularly where the main component of flow is in look direction, and must be removed in the velocity calculations. Where the main component of flow direction is in azimuth direction there will instead be a net effect on estimated flow direction. Where the incidence angle is smaller than 44°, as is the case with many side-looking radar systems, these biases will be further amplified. A 10% error as predicted by the vertical tidal movement between scenes should therefore be observable well above random noise in the TerraSAR-X data and can be used to map the grounding line.

The unmodified velocity difference map shown in Fig. 3.6a shows an apparent significant increase in velocity in radar look direction over the ice shelf between December 2009 and June 2012 with little change on the grounded ice. This increase averages around 0.09 md^{-1}, a difference that can be explained by error in calculated horizontal velocity induced by the vertical tidal movement of the ice shelf (Fig. 3.4). The Dec-1 to Dec-2 tidal and atmospheric difference is -0.589 m and Jun-1 to Jun-2 is +0.615 m, giving a double difference of +1.204 m and expected velocity error of 0.113 md^{-1} based on the radar incidence angle. This differential vertical movement

allows identification of the areas of floating ice affected by the tides, similar to established techniques using interferometry (Goldstein et al., 1993; Rignot et al., 2011a) but without the need for the high coherence in the often crevassed shear zones around the grounding line and continuously resolvable fringes required for phase unwrapping by InSAR.

3.7 Tidally-induced Velocity Change

The Ross Ice Shelf has a relatively strong diurnal tide, particularly in the K1 (23.93 hrs) and O1 (25.82 hrs) components with modelled amplitudes of 0.5 m and 0.4 m respectively at the Beardmore Glacier grounding line; conversely the semi-diurnal tidal components are weak and close to zero and the vertical movement of the ice shelf is consistently diurnal (Padman et al., 2008). A baseline for expected tidal range on the ice shelf was obtained from the CATS2008a_opt tide model (Padman et al., 2008) using eight major tidal components (K1,O1,P1,Q1,M2,S2,N2,K2). The response of ice shelves to changes in atmospheric pressure, known as the inverse barometer effect adds a further centimetre of change per hecto-Pascal (Padman et al., 2003). These air pressure effects are accounted for using Antarctic Weather Station Observations made at the 'Elaine' weather station at $83.1°S$, $174°E$ and at 'Lettau' at $82.4°S$, $174°W$, (Table 3.1). Temporal variation in load tide and solid earth tide is negligible and therefore neglected.

An equation linking tidally-varying basal shear stress to forward surface movement was put forward by Gudmundsson (2006, 2007) and is shown to be robust in replicating observed velocity variations on the Rutford Ice Stream using vertical movement from a tide model where errors in the tide prediction are reasonable (King et al., 2010). This relationship is here used to extrapolate the observed GPS-3 coverage from 2010-2011 to the satellite data acquisition period from 2009-2012. GPS-3 is close to the grounding line and we assume the variability in ice flow at this point to be representative of the grounding zone. The forward velocity, u, is related to mean basal shear stress, $\bar{\tau}$ by the following equation:

$$u = (\frac{1}{r} + 1)C(\bar{\tau} + K\rho_w g h(t))^m \tag{3.1}$$

where ρ_w is the density of ocean water, g is the gravitational constant, $h(t)$ is the tidal height, r is the ratio between mean sliding velocity and mean forward

deformational velocity, K is a site-specific constant varying in proportion to the tidal influence on velocity, C is the sliding coefficient and m is the power law exponent, hereafter taken to be equal to 3. Although sensitive to the value m, it has been shown that $m \approx 3$ fits well to data elsewhere (King et al., 2010). Measured GPS velocities and tidal displacements over a 35-day period were used to fit parameters for this relationship between basal shear stress and velocity for the Beardmore Glacier. As model parameters are not all independent, separate estimates of shear stress and sliding are made by using:

$$\tau_d = \rho_i g h sin\alpha \tag{3.2}$$

$$u_s = u - \frac{2A(\tau_b)^n}{n+1}h \tag{3.3}$$

where u_s is sliding velocity, τ_d is driving stress, τ_b is basal shear stress, h is ice thickness and A is the flow rate factor, here taken to be 1.6×10^{-10} $a^{-1}kPa^{-3}$ for ice at -20°C (Cuffey and Paterson, 2010).

The mean surface slope in the last 10 km before the grounding line of the Beardmore is 0.017, with an ice thickness of 1050 m at the centreline measured with ground-penetrating radar at the grounding line during 2010 and backed up by BEDMAP data (Fretwell et al., 2013). This gives an approximate driving stress of 160 kPa (Eq. 3.2). A very simple approximation of basal shear stress using a 'shape factor' of 0.9 gives $\tau_b = 144$ kPa. A simple depth integrated shallow ice approximation using the non-linear relation given by Glen's flow law (Nye, 1965) produces a predicted deformation velocity about a quarter of velocities measured on the glacier surface (Eq. 3.3). This suggests that the contribution of basal sliding to glacier motion is approximately three-quarters of the total observed surface velocity.

We use the parameters derived from the fit and tidal information from the CATS2008_opt tidal model to extrapolate the measured velocity dataset to cover a longer time-series and predict the expected tidal component of velocity at dates of TerraSAR-X acquisitions (Table 3.2). With a value of 144 kPa for shear stress, 3 for r and 3 for m, the best fit to data is observed with $K = 0.8$ and $C = 0.246 \times 10^{-6}$ $md^{-1}kPa^{-3}$. r and C are mutually dependent (King et al., 2010) and while r is fixed from the calculation of basal sliding, C is calculated through a best-fit to observed data.

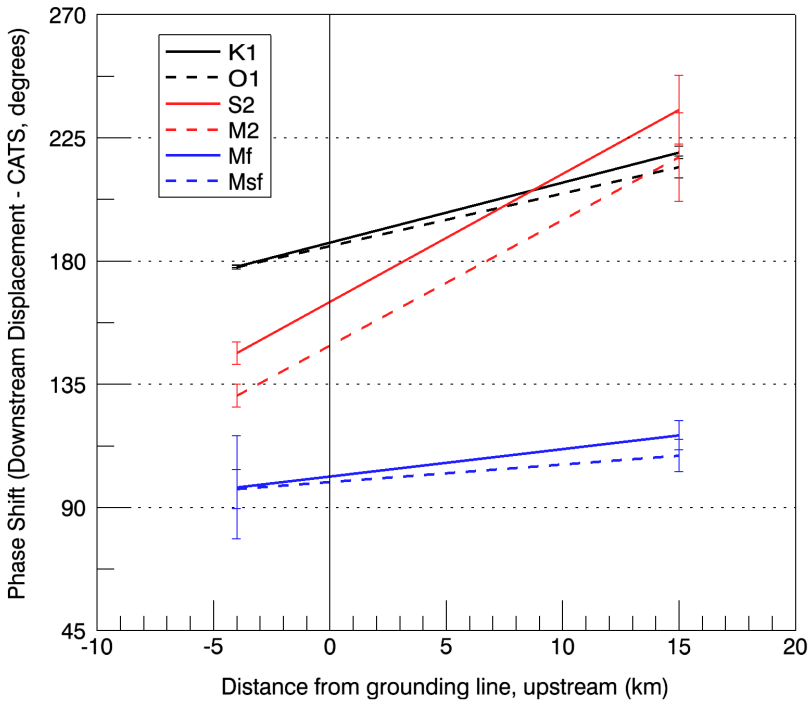

Figure 3.5: Phase difference between measured detrended-horizontal displacements in downstream direction at GPS-2 and GPS-3 and modelled vertical ocean tides from the CATS_2008opt tidal simulation (Padman et al., 2008). Phase information for each tidal component is calculated using the t_tide software package (Pawlowicz et al., 2002). Error bars are at 1σ confidence intervals.

The dependence of glacier velocity fluctuation on distance upstream of the grounding line is analysed by comparing the phase shift between the observed horizontal displacement from GPS-2 and GPS-3 and vertical ocean tides (Fig. 3.5). Tidal velocity modulation was too small to be statistically significant at GPS-1 and coverage intermittent at GPS-4. Phase calculations are done using the t_tide software (Pawlowicz et al., 2002). Vertical ocean tides are taken from the CATS_2008opt tidal simulation (Padman et al., 2008) which agrees well with the vertical movement observed in GPS-3 although with a phase shift of around 25 minutes main diurnal components. The M_f and M_{sf} tides are estimated separately as the angular resolution is not high enough to solve for both together over such a short measurement period (Gudmundsson, 2007). For the diurnal (K1, O1) and semidiurnal (S2, M2) components it can be seen that the displacement downstream is generally 180 degrees out of phase with the tides implying greatest displacement at low tides and maximum velocity during the falling tide. For the fortnightly components (M_f and M_{sf}), the peak horizontal displacement downstream is during the falling tide, corresponding to highest velocities during spring tides. The impact of tides on velocities also becomes further delayed upstream. A similar effect with distance upstream has been observed elsewhere, although the delay in all components seems less over a similar distance at the Rutford Ice Stream (Gudmundsson, 2007).

Gudmundsson (2011) showed how long-period velocity fluctuations could occur in response to semi-diurnal tides but were weak in response to diurnal tides when the ice was modelled using viscoelastic rheology. Testing such models requires more detailed knowledge of how glacier velocities vary, both temporally and spatially. The temporal variation in velocity for a single point in the grounding zone is shown in Fig. 3.2a, while a spatial pattern averaged over time is shown in Fig. 3.3. Velocity smoothed over 3-days by looking at total horizontal displacement over this period reduces the influence of diurnal tides and highlights a spring-neap fortnightly velocity variation (Fig. 3.2b). This shows that despite the small variation in this region, velocities from 3-day repeat pass satellite imagery would be sensitive to the acquisition period and not suitable for measuring long-term trends in surface velocity on this glacier. The daily fluctuations are further damped when velocities are calculated over an 11-day repeat orbit, such as with TerraSAR-X, and the changes in horizontal velocity predicted by Eq. 3.1 are largely due to the non-linear interaction between the tidal components over longer periods. As this signal is small

for the Beardmore Glacier, it is not clear from the short GPS dataset whether the resulting frequency is at the lunisolar fortnightly period (M_f) or at the lunisolar synodic fortnightly period (M_sf) due to the small semi-diurnal tides compared to other regions (Gudmundsson, 2007).

On the Beardmore Glacier the predicted variability in real horizontal velocity due to the diurnal tides over 11 days is $< 3\%$ (Table 3.2), approximately equivalent to the confidence in the TerraSAR-X velocities of around 0.03 md^{-1}. The velocity difference map shown in Fig. 3.6b shows a velocity increase across the lower glacier from mid-late March 2012 to early April 2012 (a period of only 11 days) where the vertical tide differences are approximately the same. Unlike the vertical signal observed in Fig. 3.6a, there is no well-defined break at the grounding line and the signal slowly reduces within a few tens of kilometres upstream of the grounding line. Assuming that all observed velocity change is real, the glacier experiences an increase of approximately 0.035 md^{-1} or 4%. This is around 5 to 6 times larger than the 0.006 md^{-1} predicted by the tide response model (Table 3.2) but falls within the error margin of the TerraSAR-X data.

TerraSAR-X velocities in azimuth direction only from December, March and June are shown along a central flowline for comparison with the predicted velocities from the tide response model (Fig. 3.7). By ignoring the range component any bias due to tidal displacement is avoided, and as velocity is largely in azimuth direction results remain representative of trends. There is no observable change in velocity between these periods well upstream of the grounding line and although the observed differences approach the predicted absolute error for TerraSAR-X, slightly lower velocities are observed around the grounding line in March and June, agreeing with the tide response model.

3.8 Conclusions

Building on existing knowledge of how glaciers react to tides, it is shown that velocity fluctuations in the grounding zone can be observed using high-resolution satellite data with short repeat pass intervals. On a timescale of 11-days these fluctuations are heavily smoothed and become close to the limit of detection ($< 3\%$) for the diurnally-dominated flow variation on the Beardmore Glacier although still may introduce a systematic bias in long term measurements. The relatively higher basal

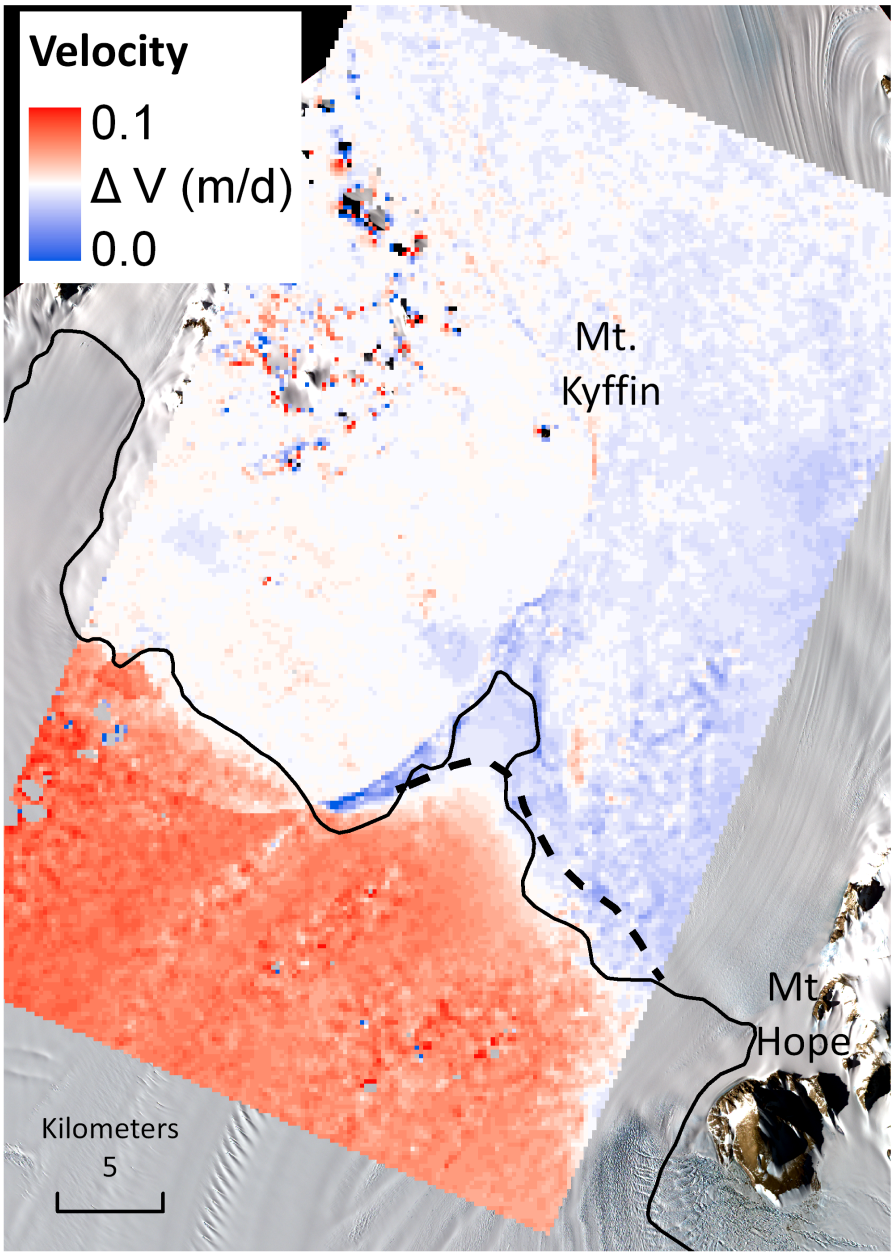

Figure 3.6a: Difference in velocity in look direction between Dec1/2 and Jun1/2 highlighting the influence of the tides downstream of the grounding line.

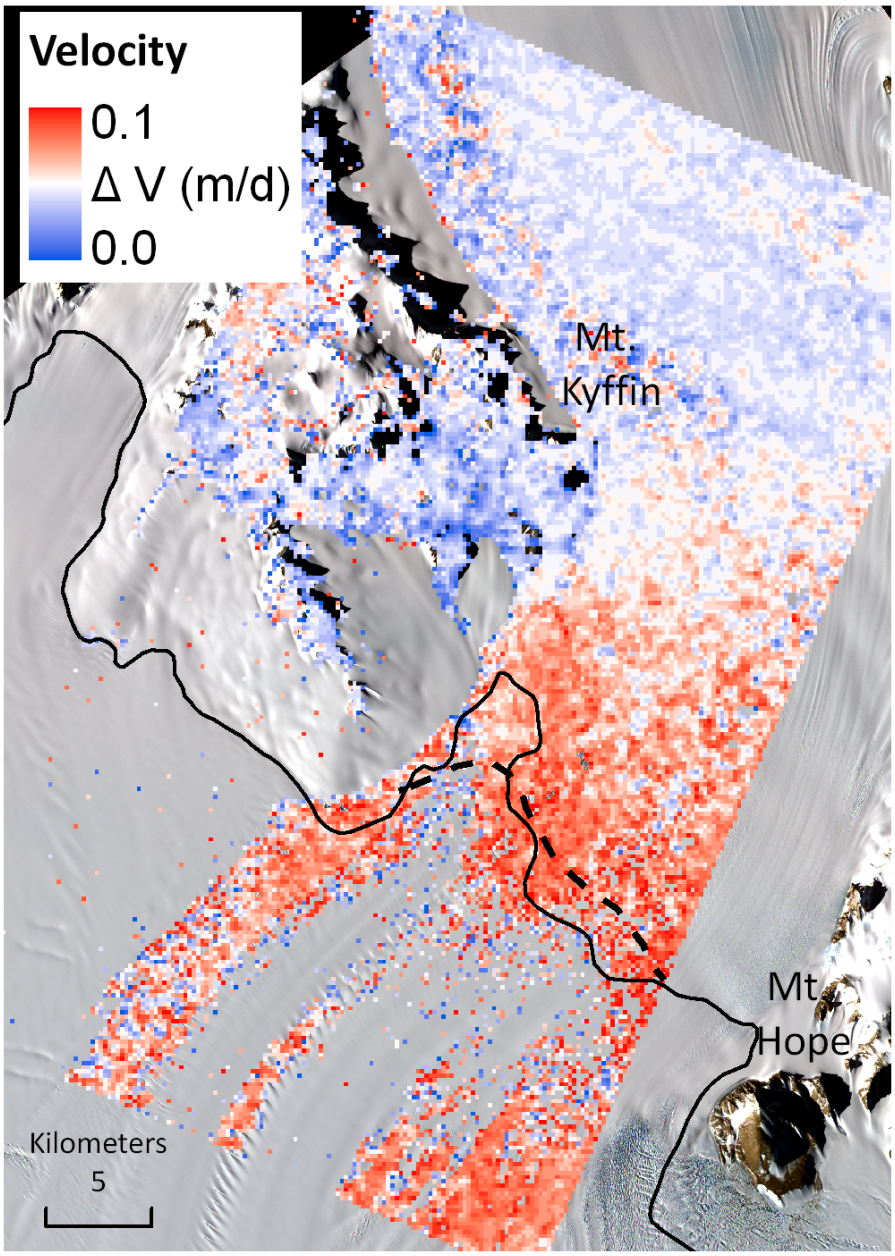

Figure 3.6b: Difference in absolute velocity between Mar-1/2 and Mar-2/3. Poor image coherence reduces data quality over the ice shelf.

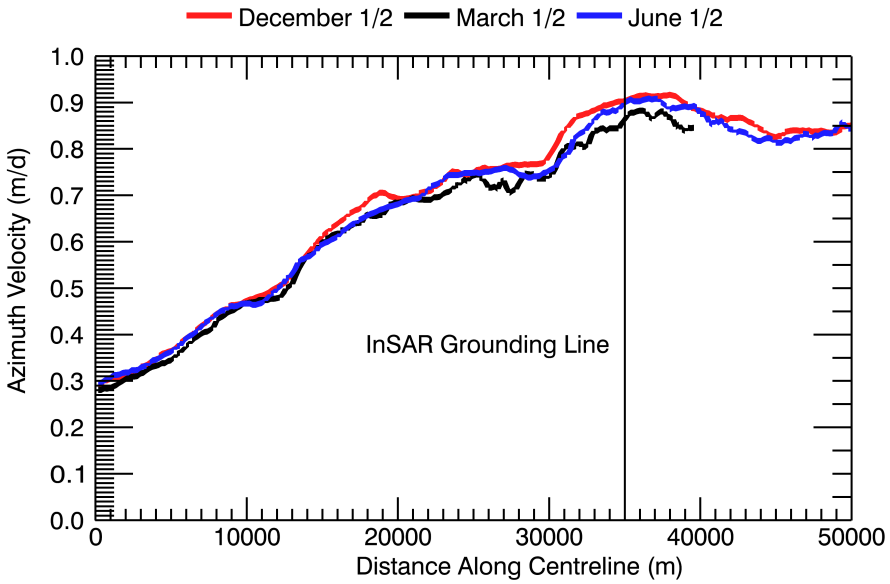

Figure 3.7: TerraSAR-X velocities in radar azimuth direction for December 2010, March 2012 and June 2012. The location of the centreline is shown in Fig. 3.3 with the origin at the upstream edge of the image.

shear stress in comparison to fast-flowing ice streams is thought to contribute to the limited upstream propagation of these fluctuations (Gudmundsson, 2003) with 1 to 2% variation in 6-hour averaged velocities during spring tide periods at the GPS 15 km upstream of the grounding line.

Velocity fluctuations have previously been observed only on ice streams with significant basal sliding. Here we observe >50% diurnal fluctuations in GPS records from the grounding zone of the Beardmore Glacier, which are not observed 15 km upstream from the grounding line. Detrending of daily signals in the grounding zone highlights fortnightly velocity fluctuation, here with a best fit around M_f period (13.7 days). This is in contrast to observations of the Rutford Ice Stream where interaction of the semi-diurnal tides causes much larger fortnightly fluctuations at the M_{sf} period. The 5-week data period is not long enough to make a firm statement that this is indeed an M_f signal, which could be a residual effect of the small semi-diurnal tides still present at this site and longer periods of observation would be necessary to draw further conclusions on the applicability of the Gudmundsson (2007) flow model at this location.

The viability of using SAR speckle tracking to map spatial variability in these short-term velocity fluctuations is also examined. In addition to horizontal displacements, speckle tracking offsets in radar look direction contain a component of the tidal vertical displacement over the ice shelf, proportional to radar incidence angle. This effect distorts calculations of horizontal velocity and flow direction in this area and should be removed using a separate tide model or reference measurements in stagnant areas over the ice shelf nearby. It can also be used to map the grounding zone where tidal range between image acquisitions exceeds the limit of detection for the radar, as is demonstrated for the Beardmore. Fortnightly horizontal velocity changes upstream of the grounding line are too small to be accurately detected here as the non-linear interaction between diurnal tides is thought to be small, however it is quite likely that spatial patterns of velocity fluctuation could be detected by this method on ice streams which exhibit stronger fortnightly velocity variations.

Chapter IV

Grounding zone ice thickness from InSAR: Inverse modelling of tidal elastic bending

We describe a new inverse modelling optimization approach to calculate ice thickness in the grounding zone of Antarctic outlet glaciers using spatial patterns of flexure derived from differential interferometric synthetic aperture radar (InSAR). We show that the ill-posedness of the inverse formulation of the elastic-plate equations for bending can be controlled by regularization. In 1-D, the finite-element model recreates smooth synthesized profiles of ice thickness from flexure information to within 1-2% and is stable for typical noise levels present in high-coherence interferograms with a moderate tidal range. The method is tested in 2-D and applied to the grounding zone of the Beardmore Glacier, a major outlet glacier in the Transantarctic Mountains, using interferograms from TerraSAR-X satellite data acquired in 2012. Results are compared with 1967 radio-echo sounding and new ground penetrating radar measurements of thickness from 2010. Best agreement (RMSE 50m) at the observed longitudinal and transverse thickness transects is obtained in this location using a value of 1.4 GPa for the effective Young's Modulus. The inverse model resolves undulations larger than a threshold distance depending on stiffness (here approximately three times the ice thickness). The highest accuracy is achieved close to the grounding line, where current estimates of thickness based on freeboard measurements contain a systematic bias towards thicker ice.

4.1 Introduction

Grounding zones, or the transition between ice sheets and ice shelves, are one of the most sensitive parts of the ice sheet system (Schoof, 2007). As the ice crosses this transition, shear stress at the bed is removed and ice accelerates, spreads and thins. In many places water in the ice shelf cavity is at significantly higher temperatures

than the pressure melting point, causing rapid melting which is particularly strong in the grounding zone (Jacobs et al., 1992; Shepherd et al., 2004; Pritchard et al., 2012). This rapid melting is likely to have the greatest impact on ice flow dynamics as ocean properties are modified by climate change (Joughin et al., 2012). To estimate the effects of rising ocean temperatures on the mass balance of outlet glaciers and future stability of ice shelves, it is vital to know melt rates in this sensitive area, as well as being able to measure the input to the ice shelves from outlet glaciers precisely through ice discharge across the grounding line. The grounding line may be identified statically from surface characteristics or dynamically looking at how the ice responds to ocean tides. Interferometric SAR and precise altimetry are used to identify the landward limit of vertical surface motion (Rignot et al., 2011a; Brunt et al., 2010a), which may vary horizontally in response to tide level and bedrock slope (Brunt et al., 2011). Additionally and independently, high resolution digital elevation models can detect an inflection point within the grounding zone, interpreted as the point where floating ice is influenced by the proximity of the grounded ice and the change in internal stress is visible at the surface (Bindschadler et al., 2011a).

Traditional methods of measuring ice discharge across the grounding line using satellite-derived thicknesses assume that ice at the grounding line is close to hydrostatic equilibrium (and therefore make a simple calculation from freeboard and ice density(e.g. Stearns, 2011)) but uncertainties may be in the range of 80 to 120m (Rignot et al., 2008). A more accurate cross-section can be calculated at the 'hydrostatic line' where the ice is far enough downstream of the grounding line to be fully floating but the distance between the hydrostatic line and grounding line is typically several kilometres, depending on ice thickness and ice properties (Fricker et al., 2009; Bindschadler et al., 2011a) and so calculating ice discharge at the hydrostatic line overlooks potentially significant basal melting upstream of this point.

Applying the hydrostatic equilibrium assumption at the flexure line must overestimate the ice thickness, as the ice is at least partially grounded and supported by the land (Vaughan, 1995), however further downstream the ice may be partly depressed below hydrostatic equilibrium and thickness consequently underestimated (Fricker and Padman, 2006). Because of both the limitations in deriving the ice thickness cross-sections in the grounding zone and the complications in observing horizontal ice flow by interferometry, tidal zones are sometimes excluded from the remote sensing analysis of melt rates (Neckel et al., 2012). Alternatively ice thick-

ness can be measured using ground penetrating radar, but the spatial coverage is then confined to the tracks measured and, in many areas, there is limited potential for multiple repeat measurements to identify thickness change.

One of the special properties of the grounding zone is that it forms a region of differential motion associated with the tidal cycle. The vertical displacement of an elastic beam of ice due to ocean tides has been described by Holdsworth (1969) and Vaughan (1995) and the theory expanded to cover 2D elastic plates (Schmeltz et al., 2002). GPS measurements in Greenland have shown that a visco-elastic deformation model better describes the vertical deflection in this region, reproducing both phase and amplitudes of tidal deflections where elastic models cannot (Reeh et al., 2000, 2003), but elastic models are shown to widely replicate amplitudes of flexure in interferometric synthetic aperture radar (InSAR) observations when a lower 'effective' Young's Modulus is used (Rignot, 1996; Schmeltz et al., 2002; Jenkins et al., 2006; Sykes et al., 2009). This effective Young's Modulus essentially accounts for primary creep deformation and can be thought of as an anelastic or delayed elastic modulus.

In this study, an inverse formulation of the elastic plate equation for bending is used to predict ice thickness from tidal flexure measurements. A thorough sensitivity analysis of the model configuration and glaciological parameters is conducted and interferograms from an outlet glacier in the Transantarctic Mountains are used to validate the numerical results against ground measurements. The Beardmore Glacier is used for validation due to availability of field data showing thickness undulations in the grounding zone and GPS measurements to constrain both vertical displacement and the value of Young's Modulus (Figure 4.1). 1D cross-sections through grounding zones have been observed to fit much better with elastic beam models of this type where the grounding zone has a downstream convex curvature than where it is concave, for example an ice rise as opposed to an embayment (Rabus and Lang, 2002). Sensitivity of the model to grounding zone curvature is therefore also tested. The Beardmore Glacier has a grounding zone with regions indicative of these two types of situation and provides further field validation. The main aim of this work is to show that the inverse formulation of the plate bending equations, based on simple elastic assumptions, can be used to solve for thickness and applied to satellite measurements to derive ice thickness at the grounding line.

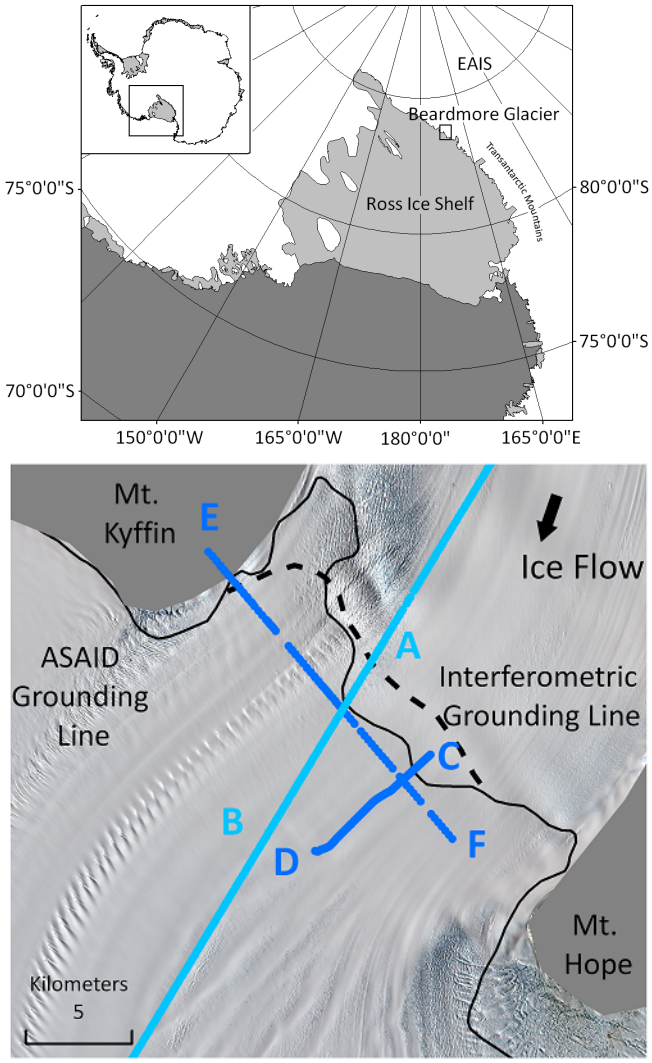

Figure 4.1: Location of the Beardmore Glacier draining the East Antarctic Ice Sheet through the Transantarctic Mountains into the Ross Ice Shelf. Inset shows Beardmore Glacier grounding zone with locations of ground penetrating radar measurements (C-D, E-F) and an ICESat track (A-B) used for validation in Figure 4.7. Dashed black line corresponds to interferometric grounding line, while solid line is the ASAID grounding line.

4.2 Elastic and Visco-Elastic Theory

Tidal flexure consists of an instantaneous elastic deformation accompanied by a time-dependent viscoplastic deformation (Hughes, 1977). Ice subject to stresses for short durations exhibits elastic or visco-elastic behaviour depending on the shear modulus of the ice, which in turn depends on ice temperature, density and degree of damage (Schulson and Duval, 2009). Gudmundsson (2007) shows that for periods of applied stress over a few seconds, ice behaves elastically with an elastic response equal to the instaneous Young's Modulus of ice, similar to that measured in laboratory experiments (e.g. Petrenko and Whitworth, 1999). While a value of 9.33 GPa is measured for isotropic polycrystalline ice in laboratory studies (Petrenko and Whitworth, 1999), a value of 0.88 $\pm$ 0.35 GPa is shown to fit better with field data collected on a number of glaciers in both Antarctica and Greenland (Vaughan, 1995). This difference can be attributed to the partially viscous deformation. Over periods of a few minutes, ice behaves as a viscous material while at periods of hours to days, ice again behaves almost purely elastically, with a lower effective Young's modulus producing a delayed elastic response (Figure A1 in Gudmundsson (2007)). An almost purely elastic response is expected on the Rutford Ice Stream for cold ice subject to tidal oscillations of between one hour and 50 days with the importance of viscous flow increasing rapidly with temperature (Gudmundsson, 2007). The maximum duration of applied stress for which ice remains in this elastic state depends on the effective viscosity, which is related to ice temperature and shear stress. Flowline modelling shows that basal ice temperature at the grounding line of the Beardmore Glacier is around -5°C with average surface temperatures of -25°C (Golledge et al., submitted) and calculation of the complex modulus of ice suggests that the amplitude of deformation caused by diurnal tidal oscillations should be well described by an elastic model at this location, despite requiring a modified (and lower) value for the Young's Modulus to account for the deformation due to primary creep over shorter timescales. GPS data obtained in the grounding zone of the Beardmore Glacier also supports a time invariant value for the effective Young's Modulus at this location (GPS-3 in Marsh et al. (2013)). A time-series of vertical deflection form this study lags behind a regional tide model (CATS_2008opt) by 22 minutes, but assuming a fixed grounding line produces a constant value for E of 1.5 $\pm$ 0.5 GPa.

The elastic deformation of a one dimensional beam of variable flexural rigidity is given by the well-known fourth-order Euler-Bernoulli equation (Holdsworth, 1969):

$$\nabla^2(D(x)\nabla^2 w) = f(x) \tag{4.1}$$

where ∇ is the gradient operator ($\frac{\partial}{\partial x}$), w is the vertical displacement, f is the applied load and D is the flexural rigidity given by:

$$D = \frac{Eh^3}{12(1-\nu^2)} \tag{4.2}$$

where E is the Young's modulus, ν is the Poisson's ratio and h is ice thickness.

The flexural rigidity is exponentially dependent on the thickness. Published values of Poisson's ratio do not vary significantly from $\nu = 0.3$, which is the value adopted throughout this study, but a fairly wide range of values has been reported for E (see Vaughan, 1995; Schmeltz et al., 2002). With the method described here it is not possible to distinguish between the separate glaciological parameters which determine the flexural rigidity of ice, so for each individual case it is assumed that ν and E do not vary spatially across the domain and that the observed variation in flexural rigidity therefore depends only on variation in ice thickness. The consequent potential error in the thickness due to variation in the glaciological parameters is discussed in parallel with the sensitivity analysis of modelling and regularization parameters.

Equation (4.1) can be split into a system of two second-order differential equations as follows (e.g. Schmeltz et al., 2002):

$$\begin{aligned} D(x,y)\nabla^2 w(x,y) &= M(x,y) \\ \nabla^2 M(x,y) &= f(x,y) \end{aligned} \tag{4.3}$$

where M is the applied moment. For a beam supported by ocean water and affected by tidal forces, $f = \rho_w g(T - w)$ where T is the magnitude of the tide.

The inverse model to calculate flexural rigidity (i.e. thickness assuming a constant value for E and ν) is ill-posed, meaning small errors in the intial data (the flexure measurements) can propagate into much larger errors and mesh-dependent oscillations about the correct value in the results (Luccinetti and Stussi, 2002). This

issue can be overcome by regularization, that is penalizing solutions with steep gradients or change in gradient of thickness, in this case so that the result minimizes ∇h or $\nabla^2 h$. Additional constraints such as the maximum allowed rate of change of thickness can be imposed in order to expediate the convergence on a numerical solution.

4.3 Interferometry

Interferometric Synthetic Aperture Radar (InSAR) uses the phase difference in two or more SAR images acquired at different times or slightly different locations to accurately identify surface displacement. Interference between the images allows centimetre-scale changes in slant-range, either related to topography or surface deformation, to be identified. Differential InSAR (DInSAR) allows removal of the contribution of topography, leaving only information about the change in displacement between images. In the grounding zone this change in displacement over short time periods is related largely to vertical movement of the ice under the influence of ocean tides and this differential technique has been widely used to map grounding lines around Antarctica (Gray et al., 2002; Rignot et al., 2011a).

InSAR data throughout this paper are taken from the TerraSAR-X mission (Breit et al., 2010) in stripmap mode which provides 9.65 GHz, 3.3m azimuth resolution and 2.5m slant range resolution data on an 11-day repeat cycle. Rabus and Lang (2002) noted that care must be taken when looking at quadruple tide difference at four individual tides (i.e.$(t_1\text{-}t_2)\text{-}(t_3\text{-}t_4)$) and that large errors can be made in locating the grounding-line where this difference is less than around 10% of the dynamic variation in tide. Here TerraSAR-X triples are acquired at periods of significant tidal variation and differenced $(t_1\text{-}t_2)\text{-}(t_2\text{-}t_3)$ to maximize the signal-to-noise ratio of the flexure data (Table 4.1). Although two other triples were acquired, they failed to produce good quality, coherent displacement maps for this glacier. As the differential baseline for the TerraSAR-X pairs is small, the topography is neglected in calculating the tidal flexure.

4.4 One dimensional modelling

The elastic beam theory is first described for a one dimensional case, with model configuration tested on synthetic profiles representing potential thickness distributions

Table 4.1: TerraSAR-X acquisitions with radar incidence angle at the scene centre for the Beardmore grounding zone, with corresponding values of modelled ocean tide from CATS2008a_opt (Padman et al., 2002). All acquisitions in stripmap mode from Beam 014, Track 039 in descending orbit.

Date	TSX Image ID	Incidence Angle (^{o})	CATS Tide (m)
05/06/12	Bea-1	44.652	-0.7421
16/06/12	Bea-2	44.655	-0.1796
27/05/12	Bea-3	44.653	-0.0025

across an Antarctic grounding zone. The one-dimensional problem is essentially a cantilever beam, fixed at the grounding line end ($w(0) = w'(0) = 0$) and freely floating at the ice shelf end ($w''(x_{max}) = 0; w'''(x_{max}) = 0$) with applied vertical load depending on vertical displacement (w). The load is due to the tidal force, which in the inverse model is known *a priori* from the interferogram. A clamped grounding line with zero rotation is used to represent the grounding line (e.g. Vaughan, 1995; Reeh et al., 2003). Grounding line migration is also disregarded. This treatment of the grounding line contrasts with the simply supported boundary approach tested elsewhere (Sayag and Worster, 2011; Walker et al., 2013) but avoids the need for modelling stresses upstream of the grounding line and simplifies analysis of the inverse model for ice resting on a solid foundation.

The solution of the forward model for an elastic beam agrees well with the analytical solution (Holdsworth, 1969; Schmeltz et al., 2002). Here we test the inverse approach using two synthetic beams of exponentially and linearly decaying thickness, as well as beams with additional Gaussian undulations in the centre. The model is initially run forward to predict vertical movement from known thickness and then a white noise Gaussian error is added to simulate uncertainty associated with the input interferograms caused by low phase coherence and resolution. The inverse model is then used to re-calculate thickness and estimate the propagation of error associated with the optimization routine. A comparison of input and output thickness for these two scenarios is shown in Fig. 4.2.

The inverse problem described here is ill-posed, and there exist a number of unique solutions to the thickness profile which satisfy the observed flexure profile. The greater the number of nodes in the finite-element mesh, the more closely the problem approximates the ill-posed continuous problem and becomes more ill-

conditioned (Lesnic et al., 1999). For conversion into a well-posed problem with an optimal solution, the objective function can be modified by adding a 'penalty function', and the thickness calculated using a least-squares optimization routine. The weighted sum of the data error and the penalty function is known as the Tikhonov functional (Tikhonov and Arsensin, 1977):

$$(w_{in} - w)^2 + \lambda(\Gamma h)^2 \tag{4.4}$$

where λ is the regularization parameter and Γ is the regularization operator. In this case the second derivative operator (∇^2) is used as the regularization operator. This minimizes the curvature of the thickness profile and skews the result towards uniform change in thickness. Model runs were also conducted using the first derivative operator $\Gamma = \nabla$ (i.e. minimizing the change in thickness and therefore skewing the results towards a constant value) but this was less effective at approximating the correct solution for undulating thickness profiles, potentially present in ice sheet grounding zones (e.g Dutrieux et al., 2013). Regularization reduces large fluctuations in thickness and as λ is increased, so the solution becomes further biased towards a uniform thickness and 'real' oscillations in thickness are lost. Selection of a suitable value for λ is vital for sufficiently constraining the minimization near the floating margin without unnecessarily biasing the solution and smoothing out genuine thickness deviations closer to the grounding line.

All modelling of ice flexure was conducted with commercial finite-element software COMSOL Multiphysics using the SNOPT (Sparse Nonlinear Optimizer) algorithms for model optimization. This uses a forward gradient-method to return the spatial values of thickness which minimize the Tikhonov functional. The optimization routine iterates the forward model and compares the least-squares difference between modelled vertical displacement and the vertical displacement observed in the interferogram. Additional constraints are imposed on the minimization, including inequality bounds on values of thickness, and limits on maximum thickness gradient. These conditions act to stabilize the solution more rapidly and ensure that unrealistic thickness fluctuations cannot occur. Sensitivity of the output to each of these parameters is discussed in more detail in the following section.

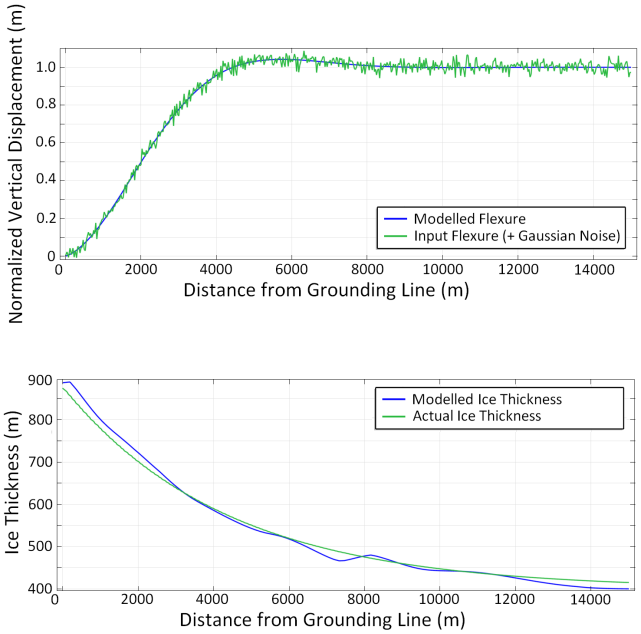

Figure 4.2: Comparison of a) input flexure with modelled flexure and b) input thickness and modelled thickness for a 1D exponentially decaying thickness profile. Input thickness is used to create flexure data, random noise in a normal Gaussian distribution is added to simulate the error in an interferogram and then the inverse model uses the flexure information to reproduce ice thickness. The quality of this reproduction is shown in b).

4.5 Sensitivity Analysis

Initially the model configuration and optimization parameters are analysed for a 1D synthetic profile in order to firstly determine the viability of the inverse method and secondly identify the optimum parameters for the model across a straight grounding line given expected noise in the interferograms. After selection of model parameters, additional sensitivity tests were conducted in 2D for a sinuous grounding line in order to assess the potential range in final thickness results caused by the choice of parameterization at embayments and land protusions. The sensititivity of the inverse approach is tested with regard to: noise in the interferogram; the Tikhonov regularization parameter (λ); glaciological parameters associated with the flexural rigidity (Young's Modulus, Poisson's Ratio, density of ice); model convergence parameters and runtime; shape and discretization of the mesh; and the size of the domain. The sensitivity is quantified by looking at the magnitude of variability in thickness output in relation to the magnitude of changes to the input variables. The percentage change in ice thickness at the grounding line and mean ice thickness in the grounding zone are calculated, as well as maximum deviation from the expected thickness within the grounding zone. The results for these tests on an exponentially decaying ice thickness profile are given in Table 4.2 with examples of output profiles in Figures 4.3 and 4.5. Model convergence parameters had little effect on the final solution except to modify the time taken for convergence and with an appropriate choice of regularization parameter fining of the mesh also produced no improvement in output thickness. For this exponentially decaying thickness profile, increasing the size of the domain to greater than approximately double the grounding zone width (in this case 12km) does not affect the thickness results within the grounding zone. Reducing the size of the domain below this value however causes a divergence from the synthesized thickness close to the downstream margin of the grounding zone, where some residual flexure is observed and therefore does not match the freely-floating condition specified in the model at this boundary ($w''(x_{max}) = 0; w'''(x_{max}) = 0$). A reduction in the domain to 10 km caused a divergence of over 25% from the expected thickness in the region between 7 and 10 km from the grounding-line. The thickness results for the upstream 7 km were not affected. Sayag and Worster (2011) suggest that for a domain greater than a threshold distance related to a set buoyancy-bending length scale, further increases in ice shelf length should have a

negligable effect on the flexure pattern. A value of 12km provides approximately 6-7 times their calculated length scale for ice of constant thickness with the synthesized stiffness used here.

With ideal input parameters, the inverse model converges rapidly on a solution within one percent of the thickness close to the grounding line. Downstream of the point of maximum vertical displacement (approximately 6km in Figure 4.2) the gradient of the flexure profile observed in the interferogram is reduced and deviation from the correct thickness becomes more pronounced. As the distance from the grounding line increases, changes in ice thickness become less important in determining the flexure pattern which becomes almost constant and small errors in the flexure can more greatly affect the resulting thickness. This is particularly highlighted by the 10% noise profile in Figure 4.3.

4.5.1 Glaciological Parameters

Variations in Young's Modulus within the range observed for outlet glaciers (Vaughan, 1995) can have a significant effect on both the calculated thickness at the grounding line and more broadly across the grounding zone (Fig. 4.4). The spatial pattern of thickness remains representative when an incorrect value of E is used but there is a constant percentage offset from the expected thickness, proportional to the error in the estimate of E. Where field measurements of thickness are not available to correct this offset to obtain a more appropriate value for E in the grounding zone (i.e. modifying E by matching modelled and observed thickness data), a best approximation can be made close to the downstream margin of the grounding zone using the hydrostatic equilibrium assumption. Adjusting the density of ice (ρ) and Poisson's Ratio (ν) within a realistic range for outlet glaciers had little effect on the simulated thickness (Table 4.2). The effect of a firn layer on flexural rigidity is accounted for in the chosen value of Young's Modulus.

4.5.2 The Regularization Parameter (λ)

The choice of λ depends on the difference between the observed flexure from the interferogram and the flexure predicted by the Euler-Bernoulli equations from a perfect thickness profile. The two main components which determine this parameter are therefore background noise within the interferogram (i.e. the interferogram not

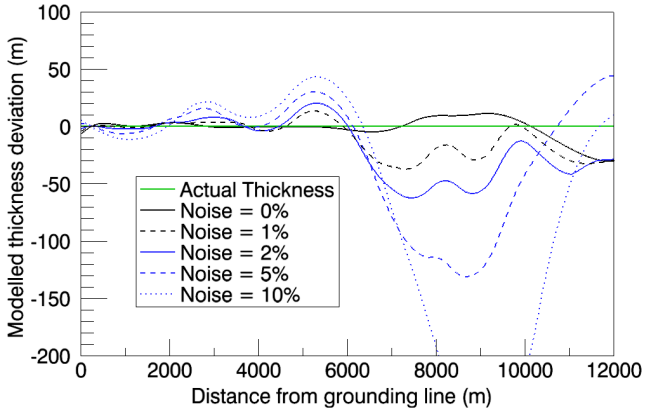

Figure 4.3: Sensitivity of the inverse 1D model to additional noise added to a simulated interferogram. All runs on an exponentially decaying thickness profile with $\lambda = 1\ e^{-22}$.

matching the actual ice flexure) and the assumptions within the model (e.g. error in flexure caused by neglecting viscous effects, shear deformation and rotational inertia).

Sensivity to interferogram noise and phase bias was analysed to assess the suitablity of using interferograms with areas of low coherence as input to the model. White noise in a Gaussian distribution was added to the synthesized flexure profile before being used as input to the inverse model to simulate the interferogram. For reference, the high frequency noise in the unsmoothed TerraSAR-X interferograms is around 1cm, or approximately 2% of the observed tide in interferograms from the Beardmore Glacier. Results are shown in Figure 4.5 and Table 4.2.

4.5.3 Thickness undulations

The 1D model performs well in the grounding zone where ice thickness decays linearly or exponentially downstream. The Euler-Bernoulli equations do not however account for shear deformation within the ice. Equally, the high dependance of the whole ice flexure profile on the ice thickness closest to the grounding line makes resolving small scale undulations further downstream of this point more difficult. The regularization method penalizes these undulations in favour of a more smoothed profile and the strength of the regularization parameter is therefore also important

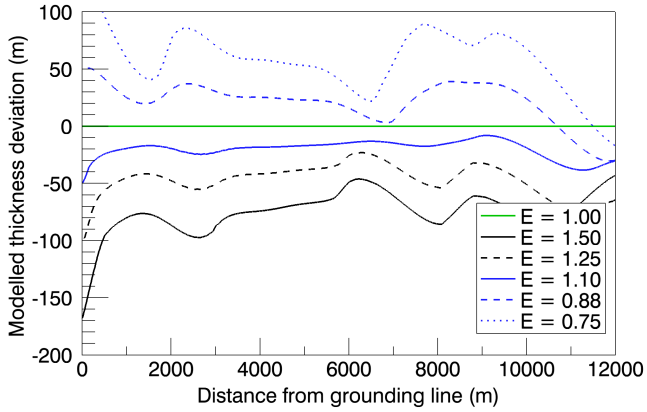

Figure 4.4: Sensitivity of the inverse 1D model to the value of Young's Modulus (E). All runs on an exponentially decaying thickness profile with $\lambda = 1\ \mathrm{e}^{-22}$ and noise = 2%.

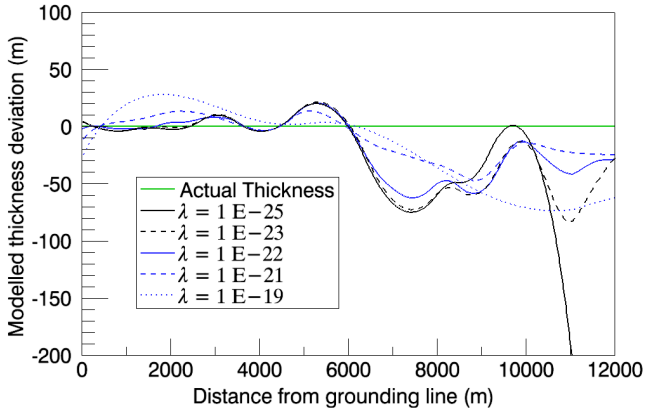

Figure 4.5: Sensitivity of the inverse 1D model to variation in λ. All runs on an exponentially decaying thickness profile with constant noise at 2%.

in determining the width and amplitude of undulations which may be resolved. The model has been tested with a number of synthetic thickness bumps added to the profile at different locations to calculate the potential of the model to capture these small-scale spatial variations in thickness. Gaussian pulses of different width and amplitude are introduced at three locations within the grounding zone: 1km downstream from the grounding line; 3km downstream of the grounding line; and 5km downstream of the grounding line. The results of this testing indicate that for E = 1GPa, bumps greater than 2-3 ice thicknesses in width occurring close to the grounding line are still able to be identified but when they occur close the freely-floating margin their influence on the ice flexure decreases and they are not resolved in the inverse model.

4.5.4 Two-dimensional sensitivity

Calculating ice flexure for glaciers is essentially a three dimensional problem with stress and strain calculated in x, y and z. As we are solving for thickness it requires only a two dimensional geometry and is hereafter referred to as 2D. The two-dimensional version of the model relies on the same constituent equations for beam bending, applied to a two dimensional domain, with lateral boundary conditions ($w''(y_0) = 0; w'''(y_{max}) = 0$). Sensitivities for an elastic beam as discussed above are equivalent to a perfectly straight grounding line of infite width in two dimensions. Grounding zones are rarely straight lines, however, and although the 1D beam approach can work well in many glaciological situations, the numerical model can also be applied to thin elastic plates with irregular plan view geometry. Sensitivity tests in 2D generally reproduce the results demonstrated in 1D (Table 4.2) where the grounding zone is linear or concave downstream, although sensitivity appears to be greater at convex grounding lines. Sensitivity to the regularization parameter is shown in Figure 4.6 for a sinsoidal grounding zone with exponentially varying thickness. Figure 4.6f further demonstrates how the regularization parameter affects the thickness derived at the grounding line, with an increase in λ leading to smoothing of ice thickness with reduced accuracy, but a decrease leading to unrealistic oscillations about the mean.

In the forward model, concave embayments have a much greater effect on the observed flexure than convex protrusions (e.g. Rabus and Lang, 2002). In contrast, the

inverse model shows greater sensitivity to these convex protrusions. The technique described here requires a higher value of the regularization parameter to smooth out fluctuations at these locations (Figure 4.6). A possible explanation for this is that there is a reduced area of contact with the fixed boundary to constrain the model near the region for which a solution is sought. While deviations of the inverse model in reproducing the flexure observed due to perfect elasic deformation may be analysed, deviations from the elastic-plate model have been observed at real grounding zones, particularly at embayments and inlets (e.g. Schmeltz et al., 2002). This cannot be tested using a synthesised flexure profile and requires further validation using field data.

4.6 Field Validation

The Beardmore Glacier ($83.5°S, 172°E$) drains a catchment of around 90,000 km^2 from East Antarctica into the Ross Ice Shelf (Figure 4.1a). The glacier flows steeply through the Transantarctic Mountains with a well-defined break of slope where it meets the ice shelf, between Mount Hope and Mount Kyffin. The glacier is around 25km wide at this point. A notable feature of the grounding zone region is a line of equidistant rifts propagating downstream from the grounding line, interpreted by Collins and Swithinbank (1968) to be caused by ice passing over a high-point on the bed, with thicker ice either side. This is supported by radio echo sounding measurements from December 1967 (Swithinbank, personal communication). Ground-based radar data were also acquired in the grounding zone during December 2010 using a 25 MHz Pulse Ekko system. The thickness data are shown in Figure 4.7b. A domain for the Beardmore Glacier is traced from differential interferograms based on the extent of the flexure zone. Expansion of the domain into the ice shelf has negligible effect on the thickness results, but identification and correct location of the fixed boundary at the grounding line is vital to produce reliable thickness maps. The grounding zone is identified here from the upstream limit of flexure observed in the interferogram (Figure 4.8a,b) (e.g. Rignot et al., 2011a). The flexure is unwrapped using the average vertical displacement over the grounded ice to fix the displacement map to 0 (Figure 4.8c).

a)

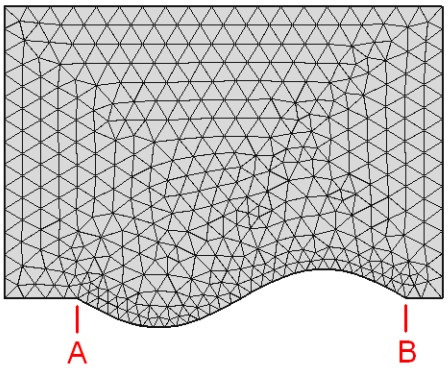

b)

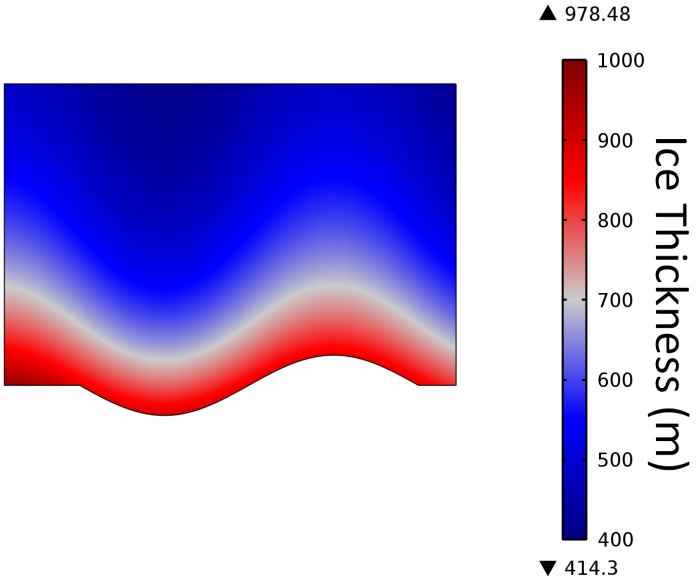

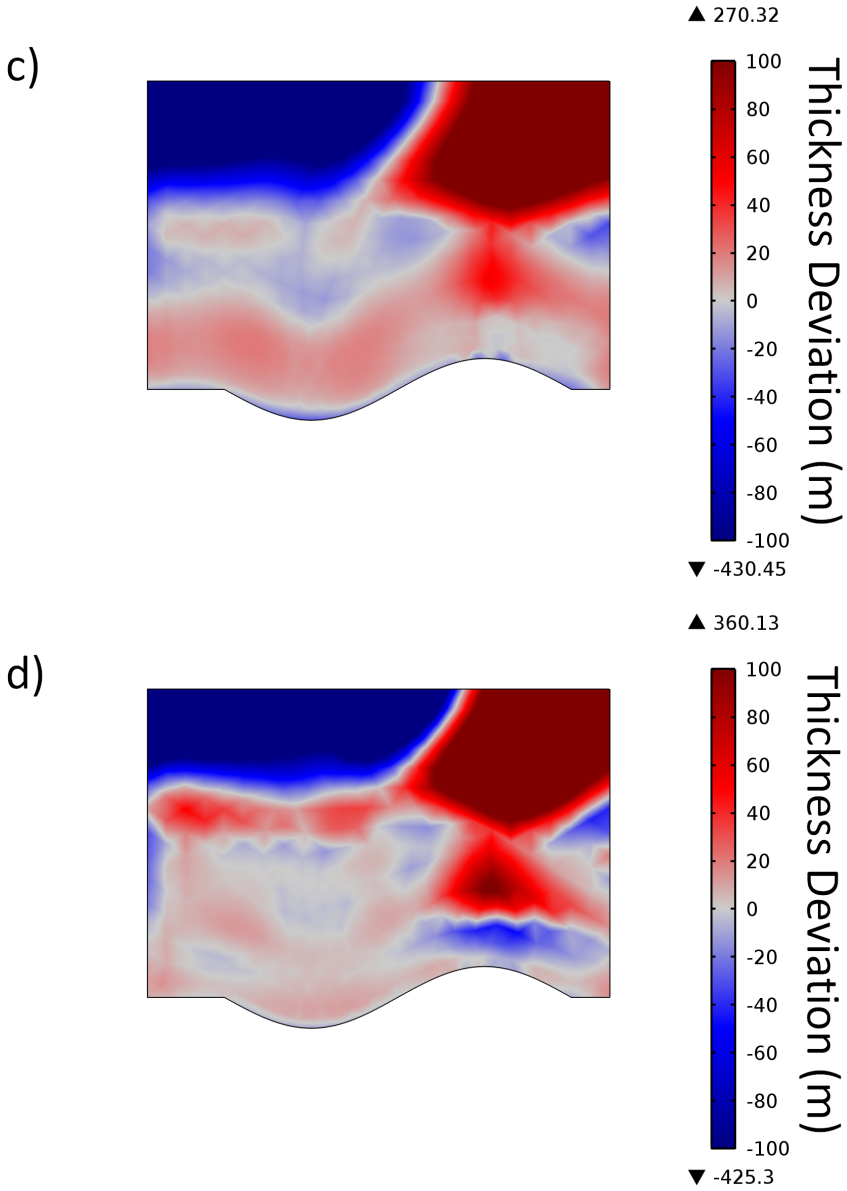
c)
▲ 270.32
100
80
60
40
20
0
-20
-40
-60
-80
-100
▼ -430.45
Thickness Deviation (m)
d)
▲ 360.13
100
80
60
40
20
0
-20
-40
-60
-80
-100
▼ -425.3
Thickness Deviation (m)

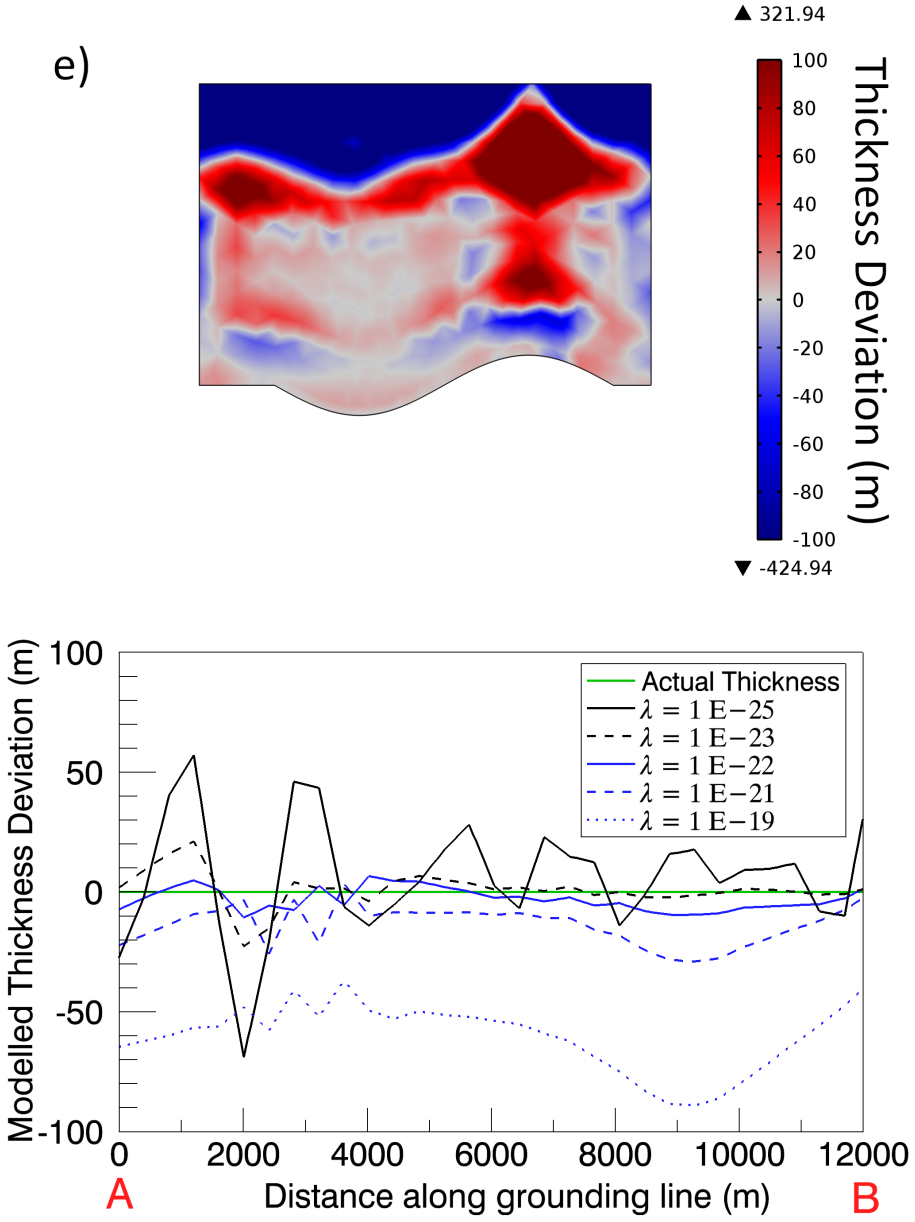

Figure 4.6: Sensitivity to the regularization parameter in two-dimensions for a sinsoidal grounding line. a) Mesh and model domain, b) Input thickness, c) Modelled thickness deviation from the input with initial conditions of $h = 500$ and $\lambda = 1e^{-21}$, d) $\lambda = 1e^{-22}$, e) $\lambda = 1e^{-23}$, f) Thickness along the curved section of the the grounding line, shown in a).

4.6.1 Initial conditions

Thickness can only be calculated using this method within the 5-10 kilometres of the grounding line where there is still differential vertical displacement. Ice that is out of the region of influence of the grounding line (i.e. where the ice moves vertically in synchronicity with the tides) should however be in hydrostatic equilibrium and its thickness can be calculated by measuring the freeboard. An intial estimate for the equivalent ice thickness is inferred by using the principle of hydrostatic equilibrium. Where ice is in hydrostatic equilibrium its thickness is given by:

$$h_{eq} = \frac{(h_f - F_c)\rho_w}{\rho_w - \rho_i} \tag{4.5}$$

where, h_{eq} is the equivalent thickness, h_f is the freeboard, F_c is the firn correction and ρ_w and ρ_i are the densities of water and ice, respectively. Grounding line position and the geometry of the model domain is obtained from the extent of TerraSAR-X imagery and the interferograms used to map flexure. Grounding line migration is limited at this location due to steep topography. A triangular mesh is used which decreases in size towards the grounding line, with spacing between nodes of 1 km on the ice shelf and approximately 500 m in sensitive areas close to the grounding line (Figure 4.8a). The model is not sensitive to the initial estimate for thickness near to the grounding line as a difference of less than 1% is observed when comparing a model run with constant initial thickness and initial thickness based on the freeboard estimate. The sensitivity to initial conditions is higher close to the floating margin of the domain, increasing to almost complete dependence on initial thickness outside of the flexure zone due to the progressively lower importance of ice thickness in this region in determining flexure.

Ice surface elevations for the Beardmore Glacier are produced from an ASTER stereographic satellite image pair at 30m resolution. This is georeferenced to ICESat points and ground-based GPS measurements. Photogrammetry produces high quality DEMs in grounding zones of steep outlet glaciers and although there is likely no systematic offset due to the applied ICESat correction, this DEM still has a standard deviation of 16 m at the grounding line in comparison to 'best-available' elevation measurements from the ASAID project, also corrected with ICESat (Bindschadler et al., 2011a). Modelled firn correction varies between 13.5 and 14.5 m in this area and

a constant firn correction of 14 m is applied to the elevation data to obtain an initial thickness estimate (van den Broeke, 2008). All data are linearly interpolated onto the mesh. A ground-based longitudinal thickness transect across the Beardmore at a central point is used here as field validation of spatial variability in thickness and to obtain a reliable estimate of the Young's Modulus. Close agreement with ice thickness from ICESat based hydrostatic equilibrium calculations close to the hydrostatic line suggests that a satellite only technique could also be used at this location. Output for the model is shown in Figure 4.8d with a direct comparison of ground penetrating radar thickness, hydrostatic equilibrium derived thickness and model thickness at linear transects in Figure 4.7.

4.7 Discussion

Sensitivity analysis shows that changes in model domain extent and discretization have a small effect on the final thickness distribution. Initial conditions are also unimportant with regard to data quality close to the grounding line, although a reasonable initial approximation of ice thickness and Young's Modulus reduces the time taken for the model to converge to a solution which agrees with GPR measurements. In the 1D case, the inverse model reproduces steady variation in ice thickness well, with models of both linearly and exponentially decaying thickness profiles downstream of the grounding line agreeing to within 1-2% with actual thickness. The 1D analysis shows that the inverse approach may be a useful tool for calculating ice thickness at the grounding line where the grounding line is relatively straight and free from side effects. The quality of thickness results in this simple case depends on the amount of noise in the intial input data (the interferogram) as well as the value of the Tikhonov regularization parameter. The Tikhonov parameter must be tuned to reduce the effect of the noise within the interferogram but not bias the thickness close to the grounding line by excessive smoothing. For low interferogram noise levels (where unwrapping is possible) and with a tidal amplitude of 50 cm, a regularization parameter of 1 e^{-20} allows for a stable thickness map which agrees with radar measurements. The optimum value of this parameter depends on rate of spatial thickness variation and model domain characteristics and may therefore be site specific. The synthetic 2D case (Fig. 4.6) suggests that a value of around $1e^{-21}$ yields best results across the grounding zone. Methods of calculating the

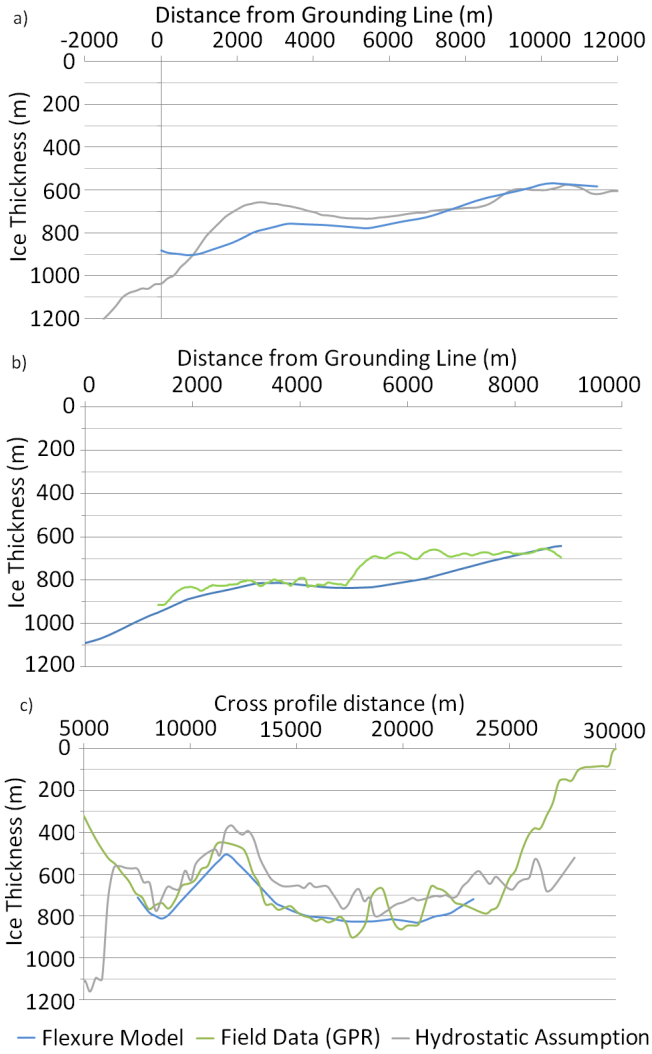

Figure 4.7: Ice thickness transects through the grounding zone of the Beardmore Glacier, showing comparison of the 2D flexure model against (a) thickness derived through the hydrostatic equilibrium assumption from ICESat surface elevations, (b) a ground-penetrating radar profile using Pulse Ekko Radar and (c) thickness as inferred from hydrostatic equilibrium assumption applied to an ASTER DEM and to airborne Radar from 1967. Locations of cross sections (A-B, C-D and E-F) are shown in Figure 4.1

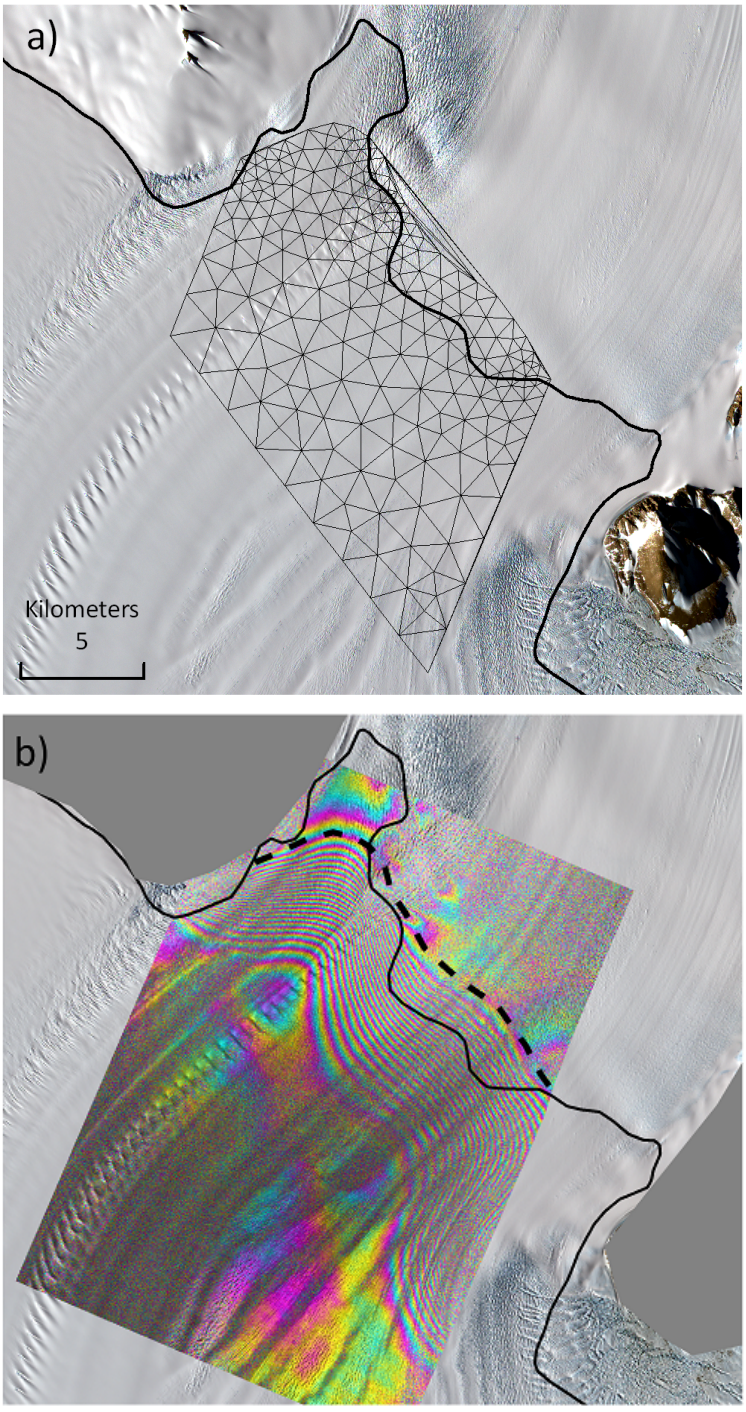
a)
Kilometers
5
b)

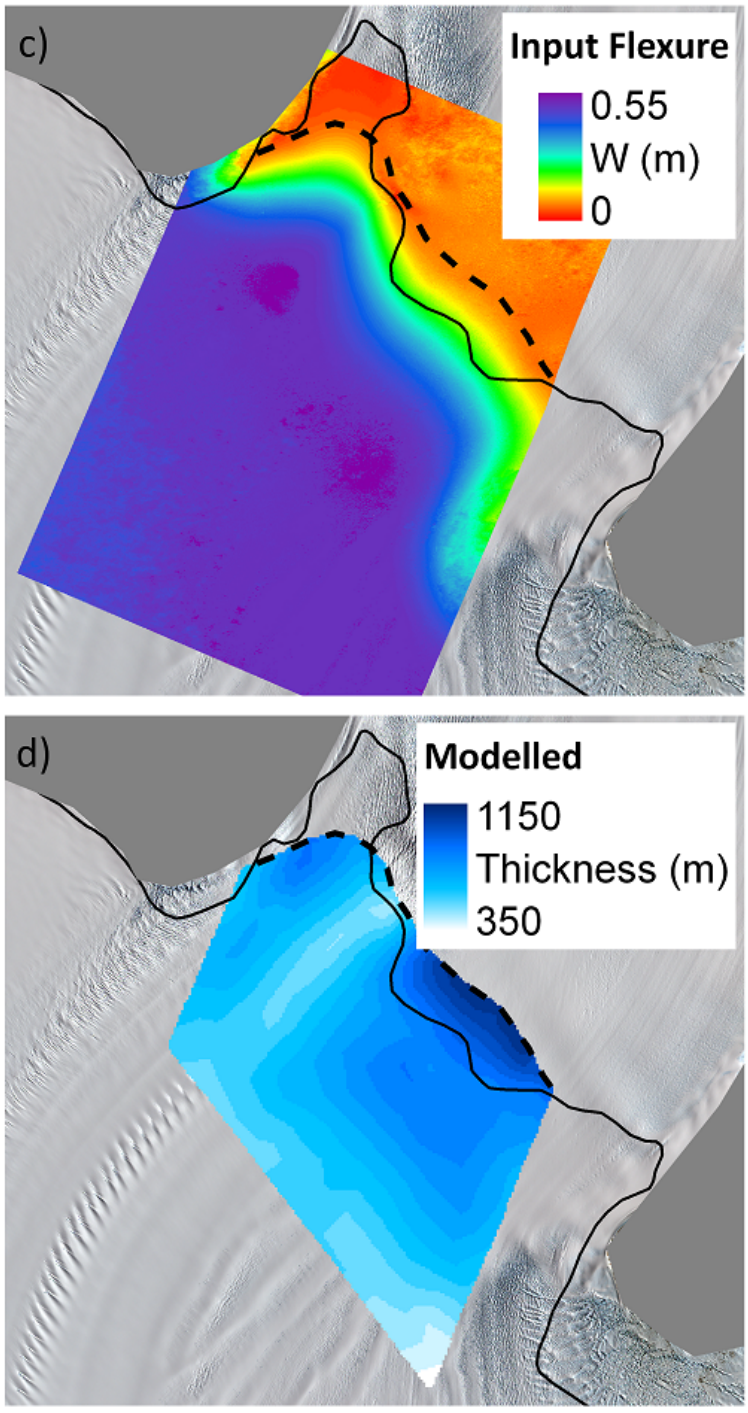
c)
Input Flexure
0.55
W (m)
0
d)
Modelled
1150
Thickness (m)
350

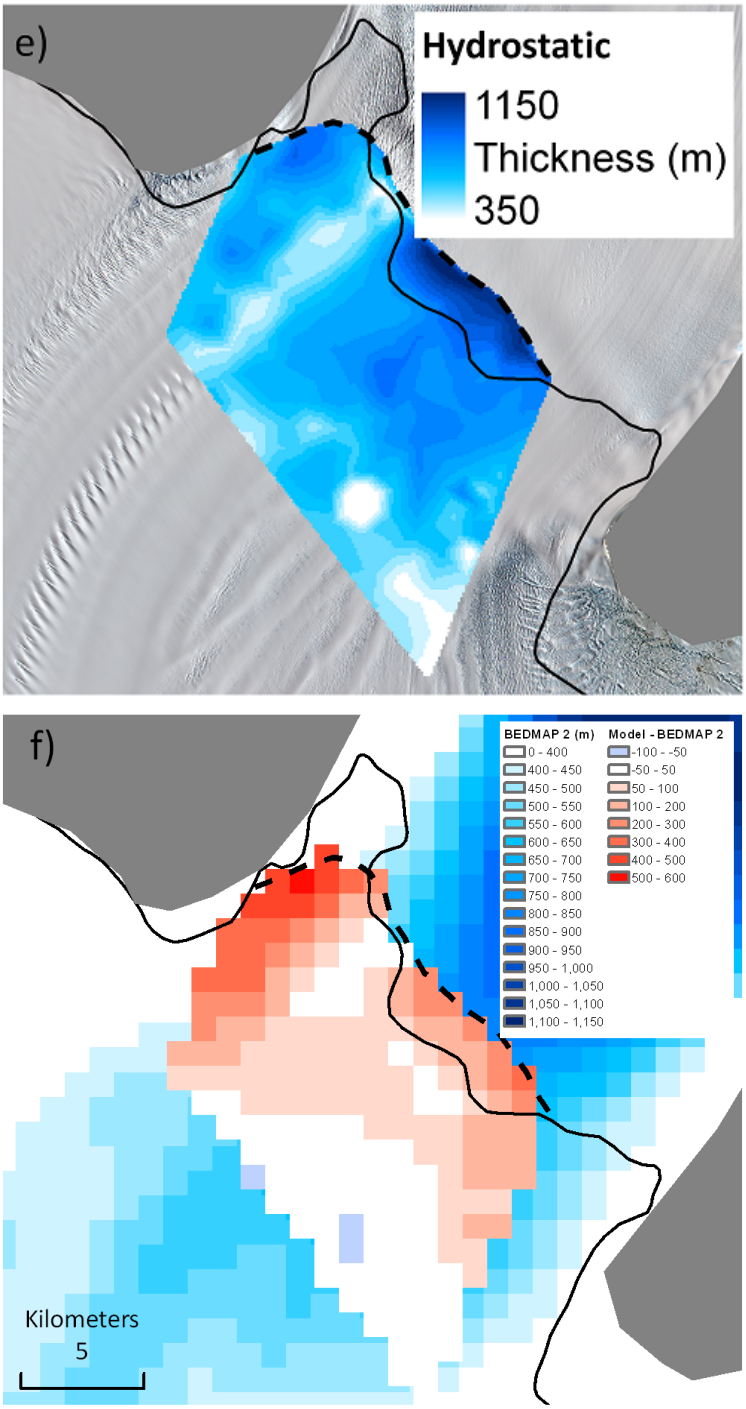

Figure 4.8: (a) Beardmore grounding zone with model domain and mesh, (b) TerraSAR-X differential interferogram showing tidal flexure fringes, (c) Differential vertical displacement derived from unwrapped interferogram, (d) Inverse modelled ice thickness in the Beardmore grounding zone, (e) Thickness assuming hydrostatic equilibrium using ICESat-corrected ASTER DEM and (f) Difference between BEDMAP-2 thickness data and model results.

optimum value for this parameter without additional information are discussed elsewhere (e.g. Luccinetti and Stussi, 2002) but are beyond the scope of this study and require further work.

In two dimensions the pattern of flexure also depends on grounding zone shape, with sinuous grounding zones affecting the observed flexure pattern. Where the elastic-theory describes the flexure pattern, the inverse model reproduces thickness well, but it requires further investigation at other locations using real observed flexure patterns to determine the wider applicability of this technique, particularly at convex grounding zones where the observed flexure is not well described by the model and warmer glaciers where visco-elastic effects may have a greater influence on the observed amplitude of vertical displacement.

Although working well for glacier thicknesses varying smoothly across the grounding zone, synthetic profiles run with an introduced bump in thickness show the limitations of this method. As the flexure profile already produces a smoothing based on the local rigidity, small undulations do not affect the interferogram and cannot be estimated using the inverse model. In particular the model fails to resolve asperities less than two to three ice thicknesses in width. More significant features, however, such as the relatively thin-ice region of rifting around 5 km wide on the Beardmore are still resolved and ice thickness changes able to be identified. In the cross section shown by Figure 4.7a the modelled thickness deviates by up to 150 m from the thickness predicted by an assumption of hydrostatic equilibrium based on ICESat data from 2009. This deviation is similar to that expected if the ice is supported above hydrostatic equilibrium at the grounding line and depressed below hydrostatic equilibrium a few kilometres downstream. In Figure 4.7b and 4.7c, the model agrees reasonably well with radar data although smoothing out large features. Differences in the long profile are likely due to ground-penetrating radar errors induced by side reflectors if the pattern seen in Figure 4.7c is a typical cross-section. Large percentage differences between modelled and hydrostatic thickness on the ice shelf in Figure 4.8e are due to the exaggerated sensitivity of thickness derived from the DEM to small artifacts in the surface elevation. Agreement with BEDMAP-2 thickness (Fretwell et al., 2013) are also within the range of expected error at this location (300 m), except to the east of the rifts where the modelled thickness is much greater but BEDMAP-2 disagrees with GPR measurements (Figure 4.8f).

The sensitivity analysis highlights the importance of a good value of 'effective' E

to ascertain the correct thickness at the grounding line. Although the 'effective' E may vary within a small range for Antarctic outlet glacier grounding zones, a 50% error in E can introduce an approximately 18% error in grounding line thickness. E can be inferred by adjusting the mean modelled thickness at the downstream boundary of the grounding zone (here approximately 10 km) to the value expected from hydrostatic equilibrium. We find a value of 1.4 GPa suitable for the Beardmore grounding zone for this particular time period, which is at the upper limit of values found by Vaughan (1995) in grounding zones around Antarctica but within the range observed by Schmeltz et al. (2002) using a similar approach. Comparison of the tidal flexure pattern from the forward model driven by CATS tidal data and our GPS measurements in the grounding zone (Marsh et al., 2013) suggest that the value of the effective E does not vary over time at this location.

4.8 Conclusion

Inverse flexure modelling has the potential to create 2D maps of ice thickness in the grounding zone without the need for surface or airborne ground penetrating radar measurements. It can also be used to spatially extend existing thickness data generated from existing ice thickness transects. The accuracy of the ice thickness results produced depends on the value taken for effective Young's Modulus, but a good approximation of the Young's Modulus can be made where ice thickness is known, either through a hydrostatic equilibrium calculation outside the grounding zone or preferably using GPR, and then this value extrapolated across the domain. This technique has become possible due to high resolution, low noise interferograms, produced from current and future SAR satellites and allows repeated measurements of ice thickness. Under normal circumstances interferograms which are able to be unwrapped have sufficiently low noise, and can easily be further smoothed with only minor impact on the resulting ice thickness. The improvement in ice thickness at the grounding line compared to the hydrostatic equilibrium thickness method is in the order of 10-15%, even where the quality of the available freeboard data is very high.

The model used here is sensitive to noise in the input interferogram and particularly relies on accurate location of the landward limit of the grounding zone but it is possible to obtain this location to a sufficient degree of accuracy in interfer-

ograms where phase coherence is high. The double difference tidal range of 50cm observed here is relatively small compared to mean tidal range around the perimiter of Antarctica (Padman et al., 2002). Larger differences in tidal displacement increase the ability to model the thickness by reducing both background noise in the interferograms and the contribution of visco-elastic effects to the flexure pattern. Although a large tidal range is preferable for the model inversion, in areas with grounding line migration images could be acquired at selected periods with a smaller difference.

We obtained good agreement at the Beardmore Glacier with reference measurements for ice thickness. Best results were obtained with the model domain extending to around twice the width of the immediate grounding line (grounding line to point of maximum flexure) to avoid bias introduced by boundary conditions close to the freely-floating margin. As the pattern of the tidal flexure depends on the geometry of the grounding line, it remains to be investigated how well the method performs for more complex grounding line configurations. We expect improved results compared to the freeboard-thickness method where the interferometric grounding line position is well defined and the elastic model accurately describes the pattern of tidal flexure.

Table 4.2: Sensitivity of 1D model runs to changes in glaciological and regularization parameters using an exponentially-decaying synthesized thickness profile. Model optimization was continued until a tolerance threshold was reached on the optimality criteria, or a maximum limit on the number of iterations was reached. Unless otherwise stated parameters used are $E = 1$ GPa, $\nu = 0.3$, Noise = 2% and $\lambda = 1\ \mathrm{e}^{-22}$.

Variable parameter	Thickness at grounding line (m)	Mean thickness in grounding zone * (m)	Maximum deviation in grounding zone (m)	RMS Deviation in grounding zone (m)
Input thickness	879.3	659.9	0	0
Noise = 0%	872.9 (-0.7%)	659.9 (-0.0%)	6.4	1.6
Noise = 1%	875.1 (-0.4%)	662.0 (+0.4%)	13.4	4.9
Noise = 2%	877.2 (-0.2%)	663.9 (+0.6%)	20.2	8.0
Noise = 5%	881.7 (+0.3%)	667.7 (+1.2%)	30.0	13.5
Noise = 10%	884.6 (+0.6%)	672.2 (+1.9%)	43.3	21.0
$\lambda = 1\ \mathrm{e}^{-25}$	883.8 (+0.5%)	663.0 (+0.5%)	20.0	8.0
$\lambda = 1\ \mathrm{e}^{-23}$	883.4 (+0.5%)	663.5 (+0.6%)	21.4	8.6
$\lambda = 1\ \mathrm{e}^{-22}$	877.2 (-0.2%)	663.9 (+0.6%)	20.2	8.0
$\lambda = 1\ \mathrm{e}^{-21}$	867.6 (-1.3%)	665.1 (+0.8%)	13.4	8.0
$\lambda = 1\ \mathrm{e}^{-19}$	852.9 (-3.0%)	670.7 (+1.6%)	27.9	16.1
E = 0.88	904.0 (+2.8%)	695.8 (+5.5%)	55.6	38.3
E = 1	877.2 (-0.2%)	663.9 (+0.6%)	20.2	8.0
E = 1.50	723.8 (-17.7%)	581.5 (-11.9%)	155.5	80.9
$\nu = 0.3$	877.2 (-0.2%)	663.9 (+0.6%)	20.2	8.0
$\nu = 0.33$	860.5 (-2.1%)	666.7 (+1.1%)	20.0	11.0

* GZ in this instance is the distance between the grounding line and 6km from the grounding line, which corresponds approximately to the point at which $\Delta w = 0$.

Chapter V

Spatial variability in ice discharge and basal melt rates in the grounding zones of Transantarctic Mountain outlet glaciers

5.1 Introduction

Melting at the base of ice shelves is important for the mass budget of the Antarctic Ice Sheet, ice shelf stability, global ocean circulation and sea ice formation. Recent analyses of the mass balance of Antarctic ice shelves suggests that basal melting exceeds total calving flux and is therefore the process which accounts for the highest volume of mass loss from Antarctica (Rignot et al., 2013). Whilst they are important for ice sheet behaviour, ice shelves also provide an important source of freshwater to the Southern Ocean, contributing to increased sea ice formation which drives the production of Antarctic Bottom Water and convection required to maintain the global ocean circulation (Hellmer, 2004). Increased sea ice extent in Antarctica in the last few decades has been linked to increased meltwater from Antarctic ice shelves (Bintanja et al., 2013). A knowledge of the precise contribution of ice shelf basal melting to regional water masses and the potential future modification of freshwater input to the oceans is therefore important not only for understanding the future of the ice shelves and ice sheets but also in modelling and predicting effects on other physical and ecological systems globally.

Recent increased melting has been linked both to rising local ocean temperatures and redirection of Circumpolar Deep Water onto the continental shelf. Rising ocean temperatures have been observed at depth throughout the world ocean during the latter half of the 20th century, with faster rates of increase observed in the Southern Ocean (Gille, 2002; Levitus et al., 2005). This increase is accompanied by a poleward migration of the Antarctic Circumpolar Current (Gille, 2008). Redirection of warm water onto the continental shelf at Pine Island Glacier related to regional wind patterns has been instrumental in accelerating melting at the ice shelf base (Walker

et al., 2007; Thoma et al., 2008). Some of the greatest increases in temperature have been recorded in the Bellingshausen and Amundsen Seas, with greater than 1°C increase in summer surface temperatures since 1951 observed in the oceans west of the Antarctic Peninsula (Meredith and King, 2005). A smaller increase of 0.3°C over 50 years has also been recorded in the top 300m of the Ross Sea, combined with a significant decrease in salinity (Jacobs et al., 2002). This warming is expected to continue at an average rate of 0.5-0.6 °C over the next century (Yin et al., 2011).

Oceanographic changes are accompanied by observed ice sheet thinning in many areas (Jenkins et al., 1997; Shepherd et al., 2004; Payne et al., 2004) and models predict accelerated thinning in the future in areas that are currently stable (Hellmer et al., 2012). Melt rates appear to be positively correlated to relative ocean temperature with 1°C effective temperature rise linked to 10 ma^{-1} increase in melt rate (Rignot and Thomas, 2002), although recent modelling suggests it is more likely that there will be a quadratic response of melting to temperature rise due to simultaneously increasing ocean convection (Holland et al., 2008).

Observations beneath ice shelves show the importance of ice morphology on melt rates, particularly related to slope of the ice-ocean interface and the presence of subglacial melt channels (Rignot and Steffen, 2008; Little et al., 2009; Vaughan et al., 2012) which can cause melt rates to vary by up to 50% over a few kilometres (Dutrieux et al., 2013). These observations imply that point measurements of melt rates should be interpreted relative to their location and highlights the need for high-spatial resolution satellite mapping methods for model validation. Although regional ice shelf cavity basal melt rates are important both for glaciology and oceanography, it has been shown that melt rates are highest close to the grounding line, where hydrostatic pressure at depth forces a depression of the melting point and subglacial meltwater provides a source of buoyancy to drive convection and heat transfer at the ice-ocean interface (Jenkins, 2011). It is the melt rate near the grounding line which will have the greatest impact on glacier dynamics, grounding-line migration and ice sheet stability (Walker et al., 2008) but it is also the melt rate near the grounding line which is hardest to measure.

Modelling suggests an average basal melt rate of between 0.1 and 0.3 ma^{-1} for the Ross Ice Shelf (Reddy et al., 2010; Loose et al., 2009) but it is likely to be much greater at depths over 1000m close to the grounding lines. These melt rates are also thought to contain a seasonal signature (Reddy et al., 2010). A strong density

gradient caused by brine from the Ross Sea polynya in winter leads to a bimodal seasonal cycle in melt rates beneath the ice shelf, with model values averaging 0.20 to 0.28 ma^{-1} (Assmann et al., 2003). Grounding zones of six outlet glaciers in the Transantarctic Mountains are examined to estimate spatial variability in melt rates in the Ross Sea region. From north to south these glaciers are the David, Mackay, Skelton, Mulock, Darwin-Hatherton (Darwin) and Beardmore Glaciers (Figure 4.1). Rignot et al. (2008) estimate that the glaciers which drain through the Transantarctic Mountains into the Ross Ice Shelf and through Victoria Land discharge ice from an area of 2.089 $\times 10^6$ km^2 or approximately 22% of the area of East Antarctica. The Byrd Glacier is by far the largest of these glaciers and has shown evidence of thinning downstream of the grounding line since 1979, associated with basal melting (Schenk et al., 2005). Studies of ice discharge have suggested that the Byrd Glacier is not in balance (Stearns, 2011) but it is also thought that its velocity may be affected by subglacial lake drainage (Stearns et al., 2008) and the glacier may not be representative of trends across this area. It is necessary to look at surrounding glaciers in more detail to fully understand how this region is responding to changing atmospheric and oceanic conditions and how melt rates vary between grounding zones.

In addition to melt rate calculations, grounding line ice discharge and glacier mass balance are calculated for comparison with catchment-wide accumulation. These glaciers have greatly different volumes of ice discharge and grounding zone characteristics, with the large and fast flowing Beardmore, Mulock and David contrasting against the smaller Skelton, Mackay and Darwin. The David and Mackay also differ in that they terminate in narrow ice tongues rather than directly into the Ross Ice Shelf. Analysis of melt rates gives an indication of how the glaciers are currently influenced by oceanic processes and could change in the future.

5.2 Methodological Overview

Discrepancies in published estimates of grounding line ice discharge from observational data are due to a combination of different estimated grounding line position, or difficulty in estimating ice thickness and ice velocity. Where estimates using different techniques are compared, the results can be highly unrepresentative of actual difference between glaciers. Basal melt rate can be calculated using a conservation

of mass approach, assuming the ice flow is in a steady state and ice is in hydrostatic equilibrium (e.g Horwath et al., 2006; Wen, 2010). The assumptions of steady state are tested by looking at past measurements of ice velocity and independent thickness estimates. The basal melt rate can be isolated by calculating the volume of ice entering finite regions of the ice shelf, both by glacial discharge across the upstream flux gate and surface accumulation; and the volume of ice leaving via glacial discharge through the downstream flux gate (Eq. 5.1).

$$M_b = (h_i v_i) - (h_{i+1} v_{i+1}) + A_s \tag{5.1}$$

where H = thickness, V = velocity, A_s = Surface Accumulation and M_b = Basal Melting. In order to establish a degree of confidence in melt rates and standardise the comparison between glaciers, the highest possible accuracy is required in both velocity measurements and calculations of ice thickness. The relative uncertainties of these quantities must be assessed individually and the best available satellite measurements combined to measure ice discharge in this region.

5.3 Grounding Line Location

The grounding line location must first be accurately determined as the gradient of thickness and velocity can be high in the grounding zone, and discharge and melt rates may be unrepresentative of the highest melt rates if calculated on the ice shelf too far downstream of the grounding line. Photoclinometrically derived grounding lines mapped during the ASAID project (Bindschadler et al., 2011a) are used as grounding line estimates due to good coverage at all glaciers, backed up by interferometrically derived grounding lines where available (Rignot et al., 2011a). ICESat tracks are largely parallel to the grounding line in this region and the method described in Chapter 2 is generally not suitable. The location of the the Moderate Resolution Imaging Spectroradiometer (MODIS) Mosaic of Antarctica (MOA) grounding line is in agreement with the ASAID grounding line at the Transantarctic Mountain outlet glaciers (Bohlander and Scambos, 2007), although ASAID does rely on MOA in some instances. The positional accuracy of the ASAID grounding lines is estimated to be ± 502 m over these outlet glaciers (Bindschadler et al., 2011a). The highest difference between ASAID and MOA occurs on the south branch of the Skelton Glacier, with the MOA grounding line suggesting the ice becomes buoyant

around 8km further upstream than the ASAID grounding line. GPS data acquired during December 2011 and January 2012 are used to constrain the actual location of the grounding line at this location. Uncertainties due to grounding line position are minimised in this study due to the steep nature of the Transantarctic Mountain outlet glaciers and better than 1km agreement between ASAID, ICESat and MOA at the majority of locations. Agreement between different techniques provides a high confidence that accurate grounding line positions have been identified for the Transantarctic Mountain outlet glaciers relative to coastlines in other areas of Antarctica where 'ice-plains' and regions of ephemeral grounding exist (Brunt et al., 2011). The 'hydrostatic line' from Bindschadler et al. (2011a) is also displayed as an approximation of where the hydrostatic equilibrium assumption should be valid, although this line is constrained by ICESat points and has a lower confidence than the grounding line.

5.4 Accumulation Estimates

Snow accumulation is estimated from published datasets using both microwave emission information to interpolate ground measurements (Arthern et al., 2006) and regional atmospheric modelling (Lenaerts et al., 2012; Monaghan et al., 2006). The atmospheric models take into account both surface ablation and accumulation, in contrast to the interpolated ground measurements, which only account for accumulation and are described as likely to be unreliable in areas subject to melt (Arthern et al., 2006). Local variation in surface ablation and wind redistribution is clearly a problem in the lower regions of these outlet glaciers, with blue-ice visible on optical imagery. This is discussed in more detail in relation to the estimation of firn density (Section 5.6.3).

Catchment basins are delineated from a combination of satellite-derived velocities and flow directions (Rignot et al., 2011b) and digital elevation models (Liu et al., 2001) by tracing flow divides and surface contours (Figure 5.1). Derived catchment area estimates agree with previous independent measurements to within 10%, (Stearns, 2011; Riger-Kusk, 2011; Frezzotti, 1997). The variability in accumulation models is however striking in this area as shown in Table 5.1 and makes reliable estimates of glacier-wide mass balance difficult without additional information.

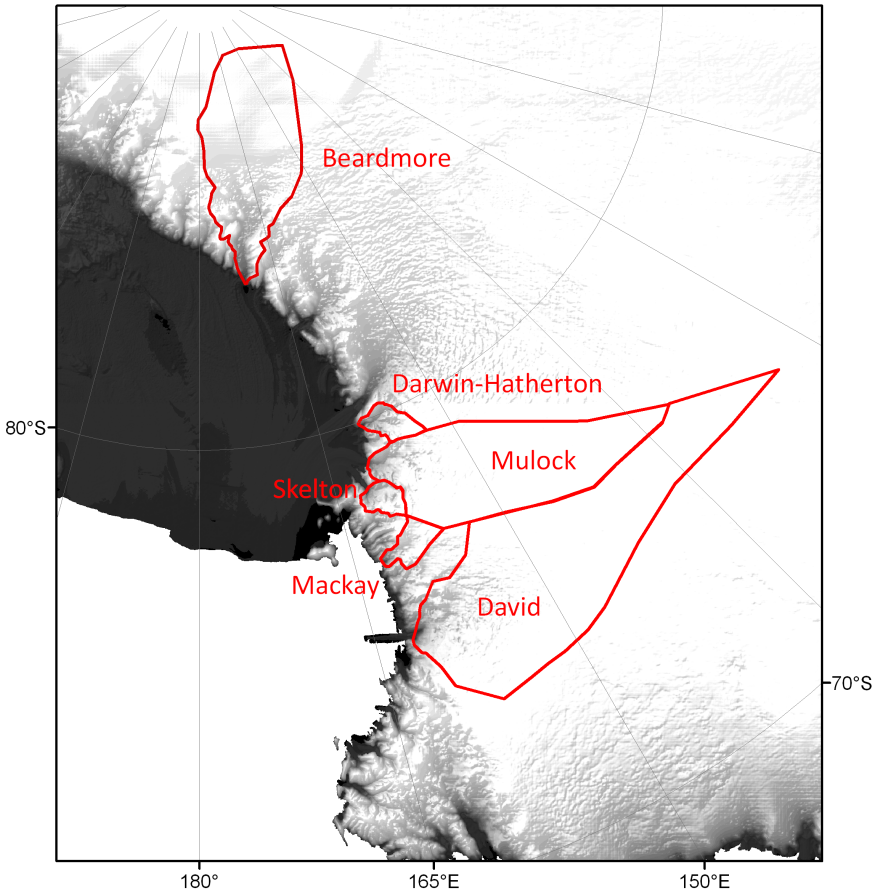

Figure 5.1: Locations of Transantarctic Mountain outlet glaciers and catchment basin outlines

Table 5.1: Modelled accumulation in TAM catchment basins (AMSR (Arthern et al., 2006), IMAU (Lenaerts et al., 2012), PMM5 (Monaghan et al., 2006))

Glacier	Catchment	Surface Mass Balance (kg $a^{-1} \times 10^6$)			
	($\times 10^3$ km^2)	AMSR	IMAU	PMM5	Average
Beardmore	92	7300	2300	8800	6133
Darwin	7.8	1370	630	1360	1120
Mulock	115	10310	3510	6400	6740
Skelton	6.4	1170	1060	890	1040
Mackay	8.6	1240	152	692	695
David	213	20600	5400	9860	11950

5.5 Surface Velocity

On floating ice, velocity at depth may be assumed to be the same as at the surface due to negligible basal shear stress (Budd, 1966). Surface velocity is calculated from TerraSAR-X speckle tracking using 11-day repeat pass acquisitions and assumed to be equivalent to depth-averaged velocity. The speckle-tracking method has low absolute error estimates of around 0.03 md^{-1} (Breit et al., 2010) and performs well when compared against GPS measurements (Chapter 3). Ionospheric perturbations are minimal at this frequency (9.6 GHz) (Mouginot et al., 2012). Speckle tracking is done in radar geometry and output vectors converted into geographic co-ordinates. Correct conversion of velocities and co-ordinates in radar geometry requires georeferencing using a DEM. The 200 m resolution RAMP DEM is used here (Liu et al., 2001).

Image correlation uses a 256^2 pixel region oversampled by a factor of two and stepped in range and azimuth directions by 32 pixels. This gives an effective ground pixel resolution of approximately 50-60 m, although the smoothing effect of the large kernel masks sharp contrasts in velocity on scales less than several hundred metres. Initial image co-registration is performed by masking out non-moving regions such as mountainous areas in each scene and adjusting the slave image so that where signal to noise ratio over the non-moving areas is high the offsets average to zero. A semi-supervised filtering routine has been developed to remove outlying values before interpolation. This code removes unrealistically high velocities and areas where coherence is poor and signal-noise ratio is low. A neighbourhood analysis is run for each point on a 3^2 kernel, discarding points where median directions or velocities

Table 5.2: Orbit and acquisition information for TerraSAR-X scenes used for velocity tracking (θ = scene centre incidence angle)

Glacier	Pairs	Date Range	Orbit	Strip	A/D	θ
Beardmore	5	12/2009 - 06/2012	039	014	D	44.6
Darwin	2	11/2012 - 12/2012	143	007	A	30.1
Mulock	2	04/2013 - 05/2013	036	007	A	31.0
Skelton	3	09/2012 - 11/2012	127	009	A	35.2
Mackay	2	02/2013 - 03/2013	084	009	D	35.3
David	2	02/2013 - 03/2013	160	014	D	44.5

deviate significantly from surrounding points or there are too few surrounding points with a good correlation match. Parameters used to define the 'acceptable degree of agreement' for directions and magnitudes are adjusted after manually checking whether artifacts remain in the final output or whether good quality data are discarded.

Statistically, 1σ random errors in velocity from the TerraSAR-X imagery for speckle tracking calibrated using stationary areas, are around 0.03 md^{-1} after adjustment for vertical tidal movement. This is approximately 1/10th of a pixel in the TerraSAR-X imagery over an 11 day period. This value is verified on the Beardmore Glacier (Chapter 3) and the Skelton Glacier by long duration GPS records. Absolute random noise is taken to be constant at the other glaciers where GPS data are not available, as the same processing methods are used. Although absolute errors remain constant, distinct glaciers produce different relative uncertainties based on glacier velocity, with uncertainty in velocity of >10% at the slowly moving Darwin Glacier and <2% on the David Glacier.

5.5.1 Tidal Effects

The effect of tidal cycles on the observed surface velocity from SAR speckle tracking is discussed in reference to Beardmore Glacier in Chapter 3. As the Beardmore Glacier has the largest individual tidal components of the glaciers studied here (Table 5.3) and the observed effect of ocean tides on actual horizontal velocity in the GPS record at the Beardmore Glacier grounding line is minimal over diurnal periods (Chapter 3), the potential contribution of a real velocity oscillation to the

Table 5.3: Components of tidal vertical motion close to glacier grounding lines

	Amplitude of tidal components (mm)							
Glacier	M2	S2	N2	K2	K1	O1	P1	Q1
Beardmore	57	69	58	27	517	396	156	78
Darwin	22	36	27	15	426	339	130	66
Mulock	21	36	26	16	417	333	127	65
Skelton	21	36	26	16	416	332	127	65
Mackay	49	70	40	29	282	239	89	47
David	57	76	43	30	251	217	79	42

TerraSAR-X long-term average is very likely to be within the stated error margins for this speckle tracking approach. Semi-diurnal tides are small in the western Ross Sea (Figure 5.2) and the flow modulation over fortnightly periods described by Gudmundsson (2006) is therefore also likely to be small for these outlet glaciers, as is observed on the Beardmore Glacier. Velocities measured using TerraSAR-X over 11-days are therefore used to represent annual average velocities in order to calculate annual average discharges and melt rates.

In contrast, the effect of incidence angle on apparent look-direction velocity was shown to be significant at all locations for TerraSAR-X and must be considered when selecting image pairs. The TerraSAR-X acquisitions used to represent mean velocity are chosen based on image coherence, quality of speckle tracking output and the tidal difference between images (Table 5.2). To estimate the incidence angle effect when analysing surface velocity over floating ice and in the grounding zone, tidal information is obtained from the 'CATS2008a_opt' tide model (Padman et al., 2008). Where grounding lines are set back from the ice shelf margin along fiords not resolved in the tide model (i.e. on the Skelton and David Glaciers), tidal values from the model for the nearest ice shelf point within the modelled domain are used.

5.6 Ice Thickness

Ice thickness on ice shelves has been calculated here by assuming that the ice is in hydrostatic equilibrium (e.g. Griggs and Bamber, 2011) and extrapolating ice thickness gradients into the grounding zone. The inverse modelling approach developed in

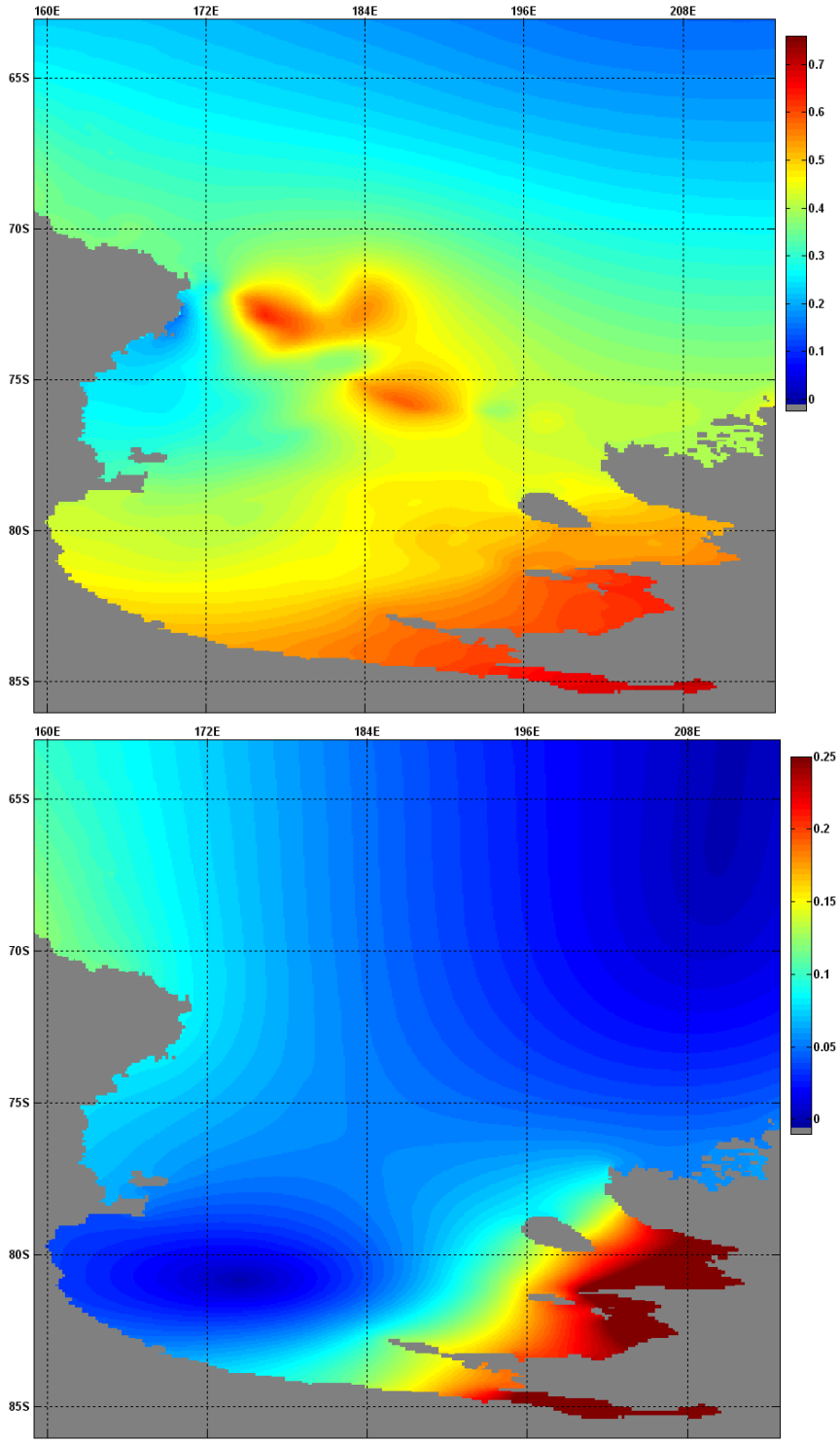

Figure 5.2: Amplitude of (a) K1 diurnal tide and (b) S2 semidiurnal tide showing the dominance of the diurnal tides in the southern and western Ross Ice Shelf and greater influence of semi-diurnal tides to the north of Ross Island. Tides are from the 'Ross_VAMDCP_9cm' model (Erofeeva et al., 2005) with amplitudes in metres. Note different scales.

Chapter 4 was shown to successfully reproduce thicknesses for the Beardmore Glacier but is not used here due to lack of high quality validation data. The variable shape of the grounding zones of outlet glaciers in this region, particularly where the glaciers terminate in narrow fiords, means that the observed flexure patterns are not well described by the elastic plate model. The low tidal amplitudes in the Ross Sea also makes resolving small changes in tidal deflection difficult where satellite acquisition periods are limited. The hydrostatic equilbrium method is improved and used to provide consistency between glaciers where radar data are unavailable. Remaining limitations with this technique are discussed and results are compared against other methods of ice thickness calculation including from BEDMAP-2 (Fretwell et al., 2013), ground-based (Riger-Kusk, 2011) and airborne radar (Gogineni, 2012). The methodology for extracting thickness from freeboard is discussed briefly in Chapter 4 and expanded here. Six parameters influence the calculated thickness (H_{eq}). These are the surface elevation measured relative to the ellipsoid (h_E); the difference between the geoid and the reference ellipsoid (h_G); the difference between local ocean height and the geoid due to dynamic topography (h_O); ice density (ρ_i); ocean water density (ρ_w); and a firn correction (F_c) which accounts for variable density snow in the upper part of the ice shelf. These parameters are related by the following equation, where H_{eq} is the equivalent ice thickness assuming constant density of ice (ρ_i):

$$h_{eq} = \frac{(h_E + h_G + h_O - F_c)\rho_w}{\rho_w - \rho_i} \tag{5.2}$$

5.6.1 Ellipsoidal Surface Elevation

Bindschadler et al. (2011a) provide a useful summary of the likely quality of available DEMs at the grounding zones surrounding Antarctica with corresponding confidence intervals. Photogrammetry performs well at the steep margins of Antarctica and is noted to be particularly good in Victoria Land (Bindschadler et al., 2011a). The SPOT-5 stereoscopic survey of Polar Ice: Reference Images and Topographies (SPIRIT) DEM provides high quality elevation data with validation against ICESat over Jakobshavn Isbrae, Greenland, resulting in elevations within ±6m for 90% of the area surveyed Korona et al. (2009). SPIRIT is, however, only available for the Darwin-Hatheron Glacier (due to its proximity to the Byrd Glacier) and cannot

therefore be used to compare glaciers whilst keeping a consistent methodology. As an alternative the ASTER GDEM v2 is used, which is also photogrammetrically derived. Some problems with the original ASTER GDEM used by Bindschadler et al. (2011a) have been corrected in GDEM-2, particularly related to geolocation. No validation of the ASTER GDEM v2 has been published for data from Antarctica but comparison with airborne data and ICESat over ice sheet margins in Greenland produces reasonable results for partially ice covered areas where more than 6-8 images are stacked, although with significant outliers in flat areas of central Greenland (Carabajal, 2011; Hvidegaard et al., 2012). Due to the high latitude of the glaciers studied here, there are high numbers of repeat passes in the ASTER GDEM-2 for all glaciers (usually greater than 10, but in some areas greater than 70), increasing the confidence in the resulting DEM. The bias and RMS error is high where less than 5 scenes are used but rapidly decreases and stabilises around 10 scenes with a bias of less than 1m and RMS error of under 8m (ASTER GDEM 2 Validation, 2011). This DEM is thought to provide a reasonable vertical accuracy over steep ice sheet margins where surface slopes are high and there is sufficient surface texture (Cook et al., 2012), improving on interpolated altimetry-based methods such as the ICESat/GLAS 500m DEM (DiMarzio et al., 2007) and the 1km DEM produced from ERS-1 Radar and ICESat Laser altimetry, which are known to have problems in steeper topography (Bamber et al., 2009).

The accuracy of the ASTER GDEM-2 at each glacier relative to the ellipsoid is assessed by comparison with ICESat point elevations. ICESat provides some of the best possible estimates of surface elevation available for Antarctica with a nominal vertical resolution of 3cm (Zwally et al., 2002) although these only provide point measurements of surface height relative to the ellipsoid (See Chapter 2). All ICESat points from 2004-2009 with footprints in the grounding zone region and on the ice shelf immediately proximal are compared with the DEM and are used in calibrating the surface elevations. The DEM is linearly shifted to remove the mean offset to the ICESat points and the standard deviation between ICESat and the DEM is used to estimate the relative uncertainty in surface elevation from this technique.

5.6.2 Geoid Correction and Dynamic Ocean Topography

The Transantarctic Mountains cause large spatial variations in the geoid due to local topography, especially further inland. Three of the most recent geoid models (EGM96, EGM2008 and EIGEN-GL04C) are compared in this area to determine the potential error in the representation of the geoid for calculations of freeboard. The GRACE satellites have improved the quality of the geoid over Antarctica but at the Darwin Glacier grounding line EIGEN-GL04C and EGM2008 differ by 2.5m and at the Skelton grounding line EGM96 and EGM2008 differ by almost 5m. EGM2008 statistically improves on EGM96 by a factor of 6 in resolution and 3 to 6 in accuracy (depending on geographic area) (Pavlis et al., 2012) and EIGEN-GL04C improves on the accuracy of EGM96 by one order of magnitude (Förste et al., 2008). Despite the higher quality and degree of expansion of EGM2008, it does not include terrestrial data from Antarctica and therefore does not perform well over the continent (Arabelos and Tscherning, 2010). Corrections for the Transantarctic Mountains are therefore made relative to EIGEN-GL04C geoid. Uncertainties in the local geoid for each glacier are estimated from the standard deviation of the three GEOID models at the grounding line of each glacier. (Table 5.4).

Dynamic ocean topography accounts for the non-tidal difference between the geoid and the mean ocean surface, related to planetary rotation and depth averaged geostrophic currents. It is not possible to accurately measure the dynamic ocean topography over large ice shelves but estimates of the difference between mean sea surface height and the geoid in the Ross Sea are between 0.8 and 1.4 metres. A value of -1.1m $\pm$ 0.3m is applied at all sites as an estimation to correct for this effect based on values close to the ice shelf margin from the DTU10MSS sea surface height model (Knudsen et al., 2011). Temporal variation in dynamic ocean topography due to ocean tides and the inverse barometer effect is not modelled here as the variation is significantly smaller than other uncertainties in both the DEMs and firn corrections.

5.6.3 Firn Correction

A firn correction is an offset applied to calculations of ice thickness using freeboard measurements to account for the variable density snow layer at the surface. It is the difference in distance between actual freeboard and freeboard if all snow was condensed to constant ice density (Eq. 5.2). This firn layer varies in thickness

Glacier	Geoid Correction (m)				Air Firn
	EGM96	EIGEN-GL04C	EGM2008	1σ	Corr. (m)
Beardmore	-41.37	-41.31	-41.50	0.10	14.6
Darwin	-56.39	-51.22	-50.02	3.38	13.7
Mulock	-56.53	-52.40	-51.03	2.86	14.5
Skelton	-55.91	-52.24	-51.19	2.48	18.7
Mackay	-55.78	-53.77	-53.43	1.27	5.5
David	-55.11	-58.50	-59.78	2.41	13.5

Table 5.4: Geoid and air firn correction values at the centre of grounding lines for glaciers in the Transantarctic Mountains. Firn correction from van den Broeke (2008)

.

and density depending on temperature, accumulation rate and wind speed (van den Broeke, 2008). At the coast the firn correction typically varies from 19 m in dry areas to 13m in wetter areas (van den Broeke, 2008) but is significantly reduced in ablation areas and can be zero where blue ice is present at the surface, as is the case in some areas of the Transantarctic Mountains. The firn correction is not well modelled and does not account for surface melting and additional compaction due to refreezing or regions with significant local wind redistribution. Models of accumulation and ablation rates are particularly poor in the complex topography of the mountains and uncertainty in firn correction is therefore estimated to account for a large percentage of the error associated with thickness measurements using the hydrostatic equilibrium approach. Modelling by van den Broeke (2008) shows a firn correction of around 13-14 m for many of the Transantarctic Mountain grounding zones, although this is not reliable on a very local scale and cannot model intra-valley variations in mountainous terrain. Blue ice is visible in optical ASTER imagery over parts of the Darwin Glacier, for example, suggesting that a firn correction of 0 m is appropriate in localised areas. For glaciers without radar measurements estimates for the firn correction at the grounding line are taken from Bindschadler et al. (2011a) based on data from van den Broeke (2008), which are given in Table 5.4. Low confidence in firn correction estimates in the grounding zone, and their amplified effect on resulting thickness, mean that where possible they are checked in an alternative manner. Ground-penetrating radar measurements are available on the

Beardmore, Skelton and Darwin Glaciers and are used to estimate the firn correction required to produce reliable hydrostatic equilibrium estimates of thickness, which often significantly deviates from published values (Section 5.9).

5.6.4 Ice and Ocean Density

The potential for ice density variations associated with the accretion of marine ice at the base of the ice shelf is thought to be minimal in the grounding zone where melting is likely to be dominant due to high pressures associated with thicker ice (e.g. Wen, 2010). Nevertheless published values for the densities of meteoric ice and ocean water vary due to different densification rates and ice impurities, and variable ocean salinity. Ice and ocean water densities of 917 ± 2 kgm^{-3} and 1027 ± 1 kgm^{-3} are used in line with other studies of ice thickness from freeboard measurements (Griggs and Bamber, 2011) and estimates of seawater density in McMurdo Sound (Albrecht et al., 2006).

5.6.5 Hydrostatic Balance in the Grounding Zone

The hydrostatic equilibrium assumption is not always reliable at the grounding line or in the grounding zone where part of the vertical weight of the ice is supported by the land (Fricker et al., 2009; Bindschadler et al., 2011a) and the thickness may deviate from hydrostatic equilibrium by over 10% (Figure 5.3). Rignot et al. (2008) suggest that calculations of ice thickness at the grounding line in Antarctica using the hydrostatic equilibrium assumption may introduce errors of around 80 ± 20 metres. In order to account for the deviation from hydrostatic equilibrium a further correction must be considered in this region. A comparison between hydrostatic-derived thickness from surface elevations with a constant firn correction and measured ice thickness from airborne radar across the grounding zone of the Skelton Glacier (Gogineni, 2012) shows a deviation from the actual thickness within the grounding zone, extending approximately 6 km downstream from the grounding line (Figure 5.3). A similar pattern is also observed in theoretical and modelling studies of the ice in the grounding zone (Sayag and Worster, 2011). In this situation, ice thickness gradient is likely to be underestimated close to the downstream edge of the grounding zone and overestimated close to the grounding line. Applying a smoothing across the grounding zone should reduce these errors, although it is quite

difficult to quantify exactly the extent of the imbalance for specific glaciers without a comprehensive modelling of all stresses acting on the ice in this region. Bindschadler et al. (2011a) calculated hydrostatic equilibrium ice thicknesses at grounding lines around the major Antarctic ice shelves to test the potential errors of assuming hydrostatic equilibrium in this region and observed only small errors in comparison with BEDMAP data around the Ross Ice Shelf, largely over the Siple Coast (9.1 ± 53.5 m difference). Much larger errors were observed on steeper outlet glaciers around the Amery Ice Shelf. Ice thicknesses from BEDMAP-2 are used here to assess the potential errors in thickness in the grounding zone from the hydrostatic equilibrium assumption, although confidence intervals on these data often exceed 300 m which is larger than the expected error using the hydrostatic equilibrium assumption (Fretwell et al., 2013).

5.7 Discharge and Basal Melt Rates

Discharge is calculated at sequential flux gates separated by 1km intervals in the downstream direction. Gates are aligned perpendicular to ice flow so that where ice flow direction varies the gates are not necessarily parallel to each other but their average separation remains constant at 1km. Georeferenced optical ASTER images and TerraSAR-X radar are used to identify surface flowlines to constrain the lateral margins of flux gates. Following the surface flowlines, the width of flux gates generally increases downstream due to horizontal spreading of the ice. Surface velocity and ice thickness are extracted at 200m intervals along each of these flux gates by bilinear interpolation from the thickness and surface velocity maps described above. Discharge through these 200m wide slices of the glacier can then be calculated:

$$D = \sum_{i=1}^{n} \frac{(h_{i+1} + h_i)}{2} w \frac{(v_{i+1} + v_i)}{2} \tag{5.3}$$

where D = discharge (m^3a^{-1}), h = thickness (m), w = width (m), n = number of intervals and v = surface velocity (ma^{-1}). Thickness and surface velocity are averaged and multiplied over each vertical segment and then these discharges summed across the cross-section. Due to the close spacing of flux gates and consequently small change in discharge relative to the associated error in inputs, the flux gate discharges are smoothed to provide average melt rates. It is assumed that noise in

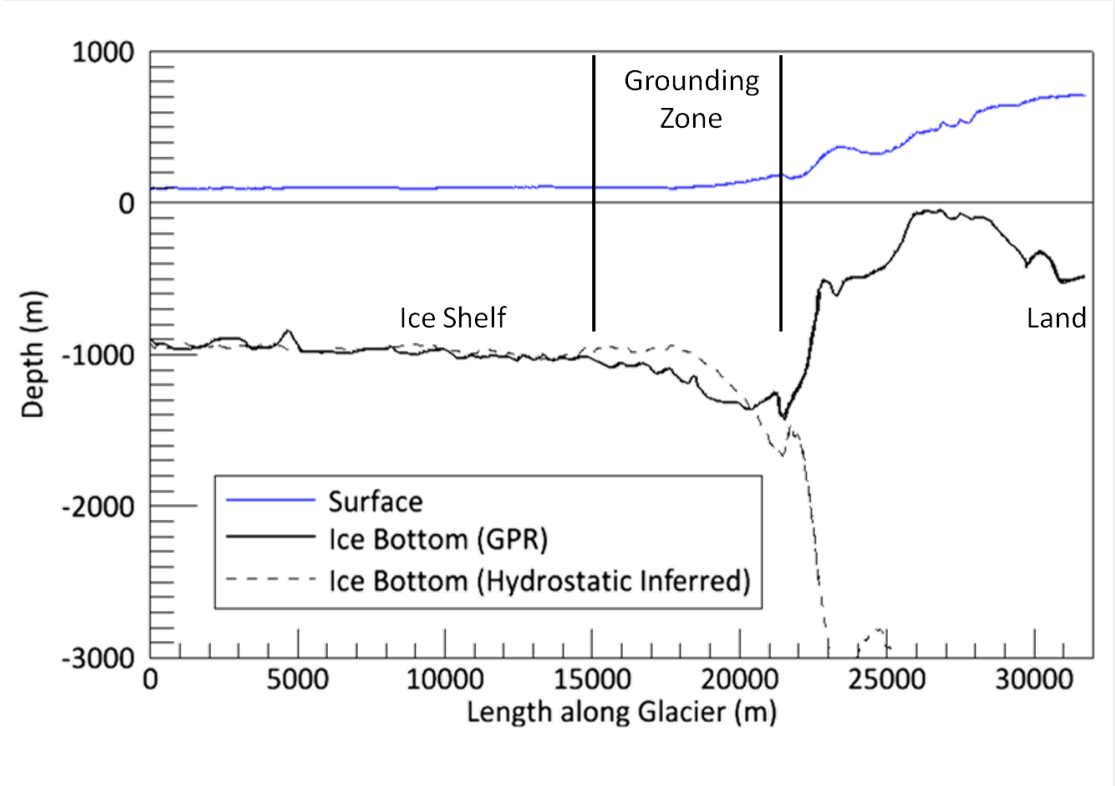

Figure 5.3: Comparison between airborne-radar ice thickness (CReSIS) and thickness assuming hydrostatic equilibrium from accurate surface elevation data for the Skelton Glacier, East Antarctica

the discharge measurements follows a Gaussian distribution with a mean of zero. A non-linear least-squares fitting function, fitting to four unknown parameters in a 'Gaussian plus constant' distribution provides the best fit to data.

$$\begin{aligned} f(x) &= A_0 e^{\frac{-\phi^2}{2}} + A_3 \\ \phi &= \frac{x - A_1}{A_2} \end{aligned} \tag{5.4}$$

where x is distance from the grounding line and A is an array representing the fitting parameters. This fit is as a substitute for a weighted moving average incorporating all data points which statistically performs significantly better than least-squares polynomial fits. The fit is made using flux gates close to the grounding line and extrapolated to the grounding line to circumvent the hydrostatic equilibrium problem in the grounding zone (Table 5.5). The total local mass balance between flux gates is calculated by differencing the discharge at consecutive gates and dividing by the area of a horizontal plane at the ice surface. This value includes surface accumulation, which is corrected for afterwards using the local value of surface mass balance from the average of the datasets described in Section 5.4 to give average local basal melt rate in metres per year (Eq. 5.1).

5.8 Results Overview

Results are described in detail at an exemplary site (Skelton Glacier) and then summarised for the other glaciers with reference to past measurements. An overview of the input data is shown in Figures 5.4 and 5.7 to 5.11 with results in Table 5.5.

5.9 Skelton Glacier

The Skelton Glacier ($78.5°S, 161.5°E$) is a moderate sized glacier and is constrained by a narrow fiord along its lower section, with its grounding line around 50km further inland than where it meets the Ross Ice Shelf. This configuration means that lateral spreading of the ice is limited and good quality measurements of basal melting can be made. Flow stripes are clearly identified on the surface from ASTER imagery and good quality airborne radar data are available for validation of this technique (Figure 5.3). Cross-sectional area and ice discharge are calculated for a series of 40 flux gates starting around 2km downstream of the grounding line (Figure 5.4).

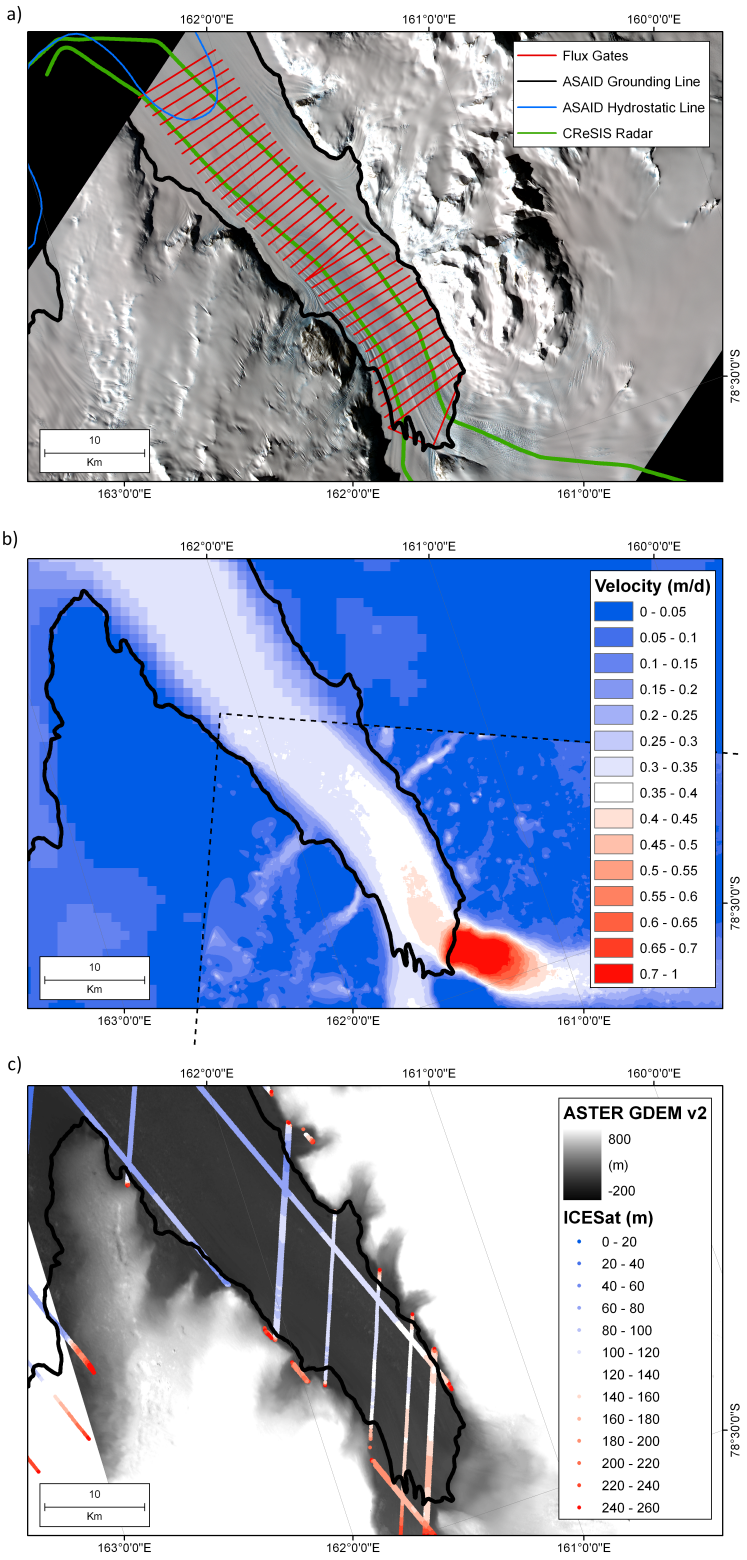

Figure 5.4: a) Flux Gates superimposed over an ASTER image, b) TerraSAR-X speckle tracking derived ice velocity (in dashed box) and MEaSUREs velocity data and c) ICESat Tracks and ASTER GDEM at the Skelton Glacier grounding line.

Velocity measurements on the Skelton Glacier from the IGY of ~ 0.24 md^{-1} close to the junction with the Ross Ice Shelf and 0.28 md^{-1} at an unspecified location on the centreline show reasonable agreement with the TerraSAR-X velocities derived here (Wilson and Crary, 1961; Cameron and Goldthwait, 1961). Velocity measurements from 1996 using ERS-1 InSAR show velocities approximately 20% higher than in this study, possibly indicating a recent slowing down in this area (McLay, 2013) however agreement is good between 2012 TerraSAR-X data and 2011 GPS measurements and between TerraSAR-X and ERS-1 and Radarsat velocities collected largely during 2007-09 from the MEaSUREs project (Rignot et al., 2011b). The glacier is assumed to be in balance over this period for calculations of melt rate. The quality of the DEM near the Skelton grounding line is high, with over 20 ASTER scenes used to estimate the elevations for most pixels. Confidence is slightly lower further out in the fiord with less than 10 scenes in some areas further downstream, possibly due to cloud coverage or fewer observable surface features suitable for photoclinometry. As the ASTER GDEM has been adjusted to the EGM96 geoid, this adjustment is first removed to obtain a geodetic height. A correlation between the ASTER DEM adjusted to the WGS-84 ellipsoid and ICESat points also referenced to the WGS-84 ellipsoid produces a median bias of 8.79m (mean 9.62 m) and RMS error of 8.83 m, with the ASTER overestimating geodetic height compared to the ICESat data. There is no spatial gradient in this bias and a value of 8.79m is used to shift the entire ASTER DEM to align with ICESat points. In comparison, the Bamber DEM in this area produces a median bias of 0.07m and RMS Error of 12.84 m. This much lower median bias is expected, as processing for the Bamber DEM uses ICESat data for calibration (Bamber et al., 2009), however the higher standard deviation suggests that ASTER is more suitable in this area.

Thickness is initially derived using a firn correction of 18.7m (Table 5.4) and dynamic ocean topography of -1.1 m. Thickness is then compared against radar measurements of ice thickness from an airborne survey conducted in 2011 (Gogineni, 2012). Range resolution from the airborne radar is less than 1 m for a frequency of greater than 180 MHz and flightlines are shown in Figure 5.4a. Where flightlines cross the flux gates, freeboard-derived thicknesses are compared against radar measurements of thickness (Figure 5.5). To convert radar data from two-way travel time to thickness, the ice is initially treated as a homogeneous medium with no adjustment for potentially lower travel time through firn layers. Processing uses

a constant dielectric (ϵ_i) of 3.15, which may introduce errors of approximately 1% or ∼10 m for dry ice (Fujita et al., 2000). A separate radar correction (R_c)can be applied afterwards using information about the air layer thickness from van den Broeke (2008). Air layer thickness (F_c) is transformed into radar correction (R_c) using the following equation (Horwath et al., 2006):

$$R_c = \frac{\sqrt{\epsilon_i} - 1}{\sqrt{\epsilon_i}} F_c \tag{5.5}$$

which produces a radar correction of 8.2 m. Despite uncertainty related to the thickness of the firn layer, and therefore the radar correction, the radar data are assigned the highest confidence in these analyses, with less potential for significant errors and a lower dependence on the uncertainty in thickness of the firn layer than the DEMs and the hydrostatic equilibrium method. Thicknesses of 1500-1600m are observed in these radar measurements at the grounding line which is more than double the peak thickness from the BEDMAP-2 dataset (Fretwell et al., 2013).

Linear regression between the radar and freeboard methods shows good correlation (R^2 = 0.79). Surface variability of 8.83m in the ASTER elevations should translate into roughly 82.5m variability in thickness (due to exaggeration of uncertainty in the conversion of freeboard to thickness and additional uncertainy in the geoid and ice and ocean densities). A bias of 121.9 m and RMS error of 100.4 m with higher radar-derived thickness suggest that the van den Broeke (2008) value for firn correction is on the order of 10-13 m too high at this location. A firn correction of 5.7 m produces the best fit against the re-adjusted radar data. Additional variability in thickness in relation to the radar-derived thickness may be due to variation in the firn density across the glacier, which is unmodelled in this analysis.

Thicknesses and therefore fluxes are calculated with a modified firn correction of 5.7 m. A velocity profile for the glacier is shown in Figure 5.4 and ice fluxes at 1km intervals in Figure 5.6. Fluxes are also calculated using thicknesses derived from the Bamber DEM for comparison. As these fluxes show some variability due to individual uncertainties, a smoothing fit is applied and melt rates calculated from the fitted curve. The standard error on the fit is 0.021 and 0.032 km^3a^{-1} for the ASTER GDEM v2 and Bamber DEM respectively. The Skelton Glacier undergoes a halving of thickness from around 1400 m close to the grounding line to 700 m near the mouth of the fiord with only a small decrease in velocity. As there is little

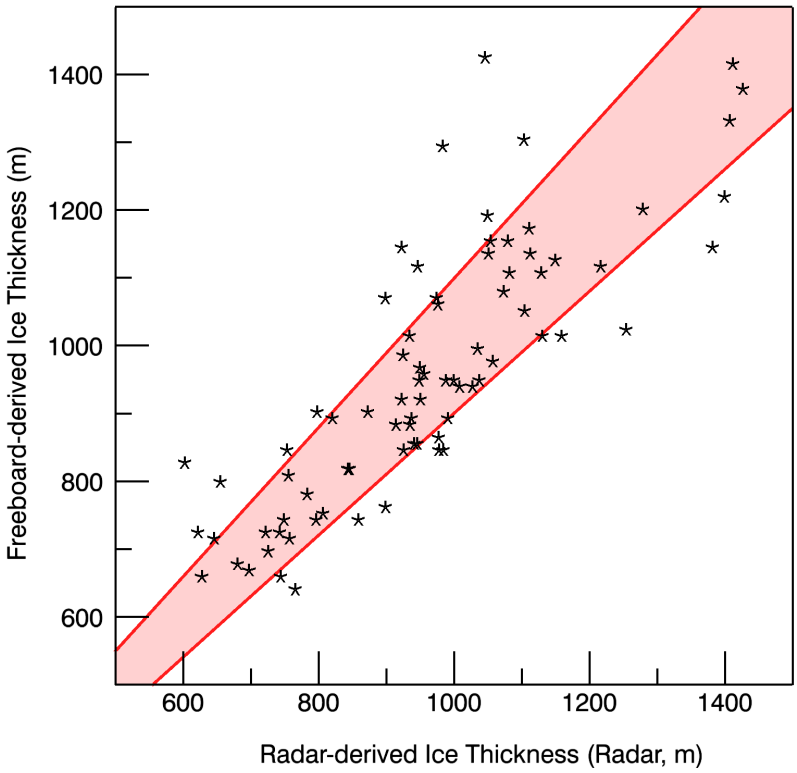

Figure 5.5: Comparison between freeboard- and radar-derived ice thicknesses for the Skelton Glacier. Measurements of thickness taken at 80 locations where airborne radar measurements cross flux gates. Red band indicates agreement within 10%.

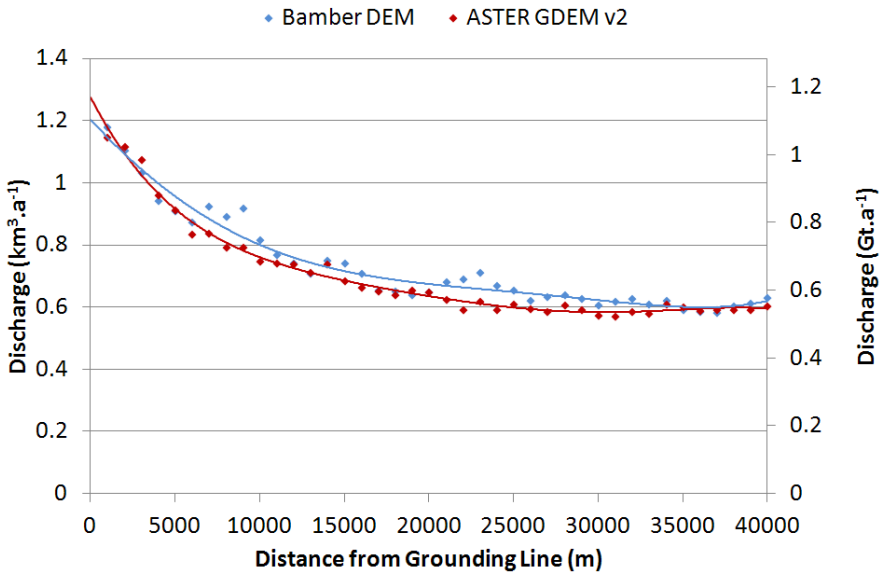

Figure 5.6: Discharge through flux gates downstream of the Skelton Glacier grounding line with Gaussian fit across all flux gates. Location of flux gates are shown in Figure 5.4

possibility of lateral spreading of the ice, the decrease in thickness is attributed to high basal melt rates within the first 10 km from the grounding line. At the closest flux gate to the grounding line there is a negative local mass balance of 5.5 ma^{-1} (Bamber) and 6.5 ma^{-1} (ASTER), decreasing to less than 0.3 ma^{-1} in the last 10 km further out in the fiord.

Adding the effect of surface accumulation of 333 kg $m^{-3}a^{-1}$ (0.36ma^{-1} ice equivalent) gives a best estimate of melt rate of 6.86 ma^{-1} close to the grounding line using hydrostatic equilibrium on the ASTER DEM. Agreement between radar-derived thickness and thickness from hydrostatic equilibrium extends significantly further up the fiord than the hydrostatic line recorded by Bindschadler et al. (2011a) and ice fluxes are reliably calculated to within 5 kilometres of the grounding line. Extrapolating the trend upstream produces a discharge of 1.15 km^3a^{-1} or 1.05 Gt a^{-1} at the grounding line, which is consistent with accumulation of 1.04 Gt a^{-1}.

For the Skelton, the mean thickness is 880 m with uncertainty from the hydrostatic method of 100.4 m. The mean flux gate width is 8140 m, with uncertainty of 30 m and the mean velocity is 88.4 $\pm$ 11.0 ma^{-1}. The uncertainty in flux gate width estimation becomes negligible where good flowlines can be identified, as is the case

on the Skelton. Assuming discharge (D) depends on the independent observables thickness (T), width (W) and velocity (V) with associated mean errors (σ_D, σ_W and σ_V), the total error in ice flux can be estimated via a simple error propagation equation (e.g. Drosg, 2009):

$$\frac{\sigma_D^2}{D^2} = \frac{\sigma_h^2}{h^2} + \frac{\sigma_w^2}{w^2} + \frac{\sigma_v^2}{v^2} \tag{5.6}$$

$$= \frac{100.4^2}{880.9^2} + \frac{30^2}{8140^2} + \frac{11.0^2}{88.4^2} \tag{5.7}$$

This produces an uncertainty in a discharge of 16.8% or 0.118 $\mathrm{km^3 a^{-1}}$ for an average flux gate with 0.7 $\mathrm{km^3 a^{-1}}$ discharge. For a slowly flowing glacier such as the Skelton the percentage uncertainty in surface velocity is higher than the uncertainty in thickness, while at the faster glaciers uncertainty in thickness is dominant.

In the calculation of melt rate, multiple discharge measurements are combined, using a weighting of their individual measurement errors (Eq. 5.7) to produce a smoothed curve with a non-linear least-squares best fit. The fitting routine rapidly converges on a minimum value for χ^2 which is used to indicate the goodness of fit to the data. For the Skelton, $\chi^2 = 4.5 \times 10^{-4}$, whilst the standard error between the fit and the data equals 0.021 $\mathrm{km^3 a^{-1}}$. This standard error is then used in calculation of the uncertainty for melt rate predictions, 1 σ uncertainty in melt rate for an average flux gate for the Skelton Glacier is 2.61 $\mathrm{m a^{-1}}$ for the ASTER DEM and 3.97 $\mathrm{m a^{-1}}$ for the Bamber DEM.

5.10 Darwin Glacier

The same analysis has been conducted on the Darwin-Hatherton Glacier System which drains a relatively small catchment to the north of the Byrd Glacier with a grounding line at approximately 80 °S. The ice thickness was measured using GPR to be approximately 1050 m at the grounding line (Riger-Kusk, 2011). As well as the standard ASTER GDEM, surface elevation data from stereo SPOT imagery created under the SPIRIT project are of high quality in this region (Korona et al., 2009) and the DEMs may be compared.

Spatial correlation between airborne radar data collected in the grounding zone as part of the IPY ICECAP project (D. Blankenship, unpublished) and a hydrostatic

thickness derived from a SPIRIT DEM is high (R^2) = 0.914. The best correlation is obtained with a firn correction of 7.1 m. This is again significantly below the range described by van den Broeke (2008) but close to that modelled on a local scale by Riger-Kusk (2011). Discharge across flux gates delineated by flowlines close to the lateral margins of the glacier peaks at 0.31 km^3a^{-1} from the ASTER GDEM, 0.32 km^3a^{-1} from the Griggs and Bamber (2011) thickness estimates and 0.34 km^3a^{-1} from the SPIRIT DEM. These values agree to within 5% with a ground-based thickness profile between the same flowlines of 0.337 km^3a^{-1} (personal comm, Mette Riger-Kusk). The sheared and more slowly flowing outer margins not included in the flux gate calculations would likely contribute an additional $< 5\%$ to overall discharge from this glacier.

Melt rate calculations from the SPIRIT DEM show net melt rates 2 km downstream of the grounding line of 1.0 $\pm$ 0.42 ma^{-1} with 1.4 $\pm$ 0.64 ma^{-1} from the ASTER thickness data. Blue ice at the surface indicates that these basal melt rates may in fact be lower to account from thinning due to sublimation.

5.11 Mulock Glacier

The Mulock Glacier at $(79.0°S, 160.5°E)$ drains a relatively large catchment between the Byrd and David Glaciers into the Ross Ice Shelf. The glacier accelerates as it approaches the grounding line with a peak velocity in TerraSAR-X speckle tracking of around 460 ma^{-1} where it meets the ice shelf and significant surface crevassing. Ice then spreads out and slows as it becomes unconfined by the valley sides. Swithinbank (1963) recorded a centreline velocity of $\sim$ 387 ma^{-1} at the grounding line (Stearns, 2007), although the Swithinbank measurements are approximately 9km upstream of the grounding line, where TerraSAR-X measurements are also lower, around 370 ma^{-1}. Although (Stearns, 2011) observes a speeding up of the Mulock between 2001-02 and 2006-07 of around 10%, this trend does not continue through to 2013, where TerraSAR-X velocities from April 2013 more closely match 2001-02 measurements.

Currently published values of discharge at the Mulock grounding line range from 2.1 km^3a^{-1} (Humbert et al., 2005) to 6.8 $\pm$ 1.0 km^3a^{-1} (Rignot and Thomas, 2002) and in this analysis extrapolation of flux gates on the ice shelf gives a discharge across the grounding line of 6.28 km^3a^{-1} and melt rate of 7.4 $\pm$ 5.35 ma^{-1}. The ASTER GDEM shows good agreement with the ICESat with a 6.4m bias and standard

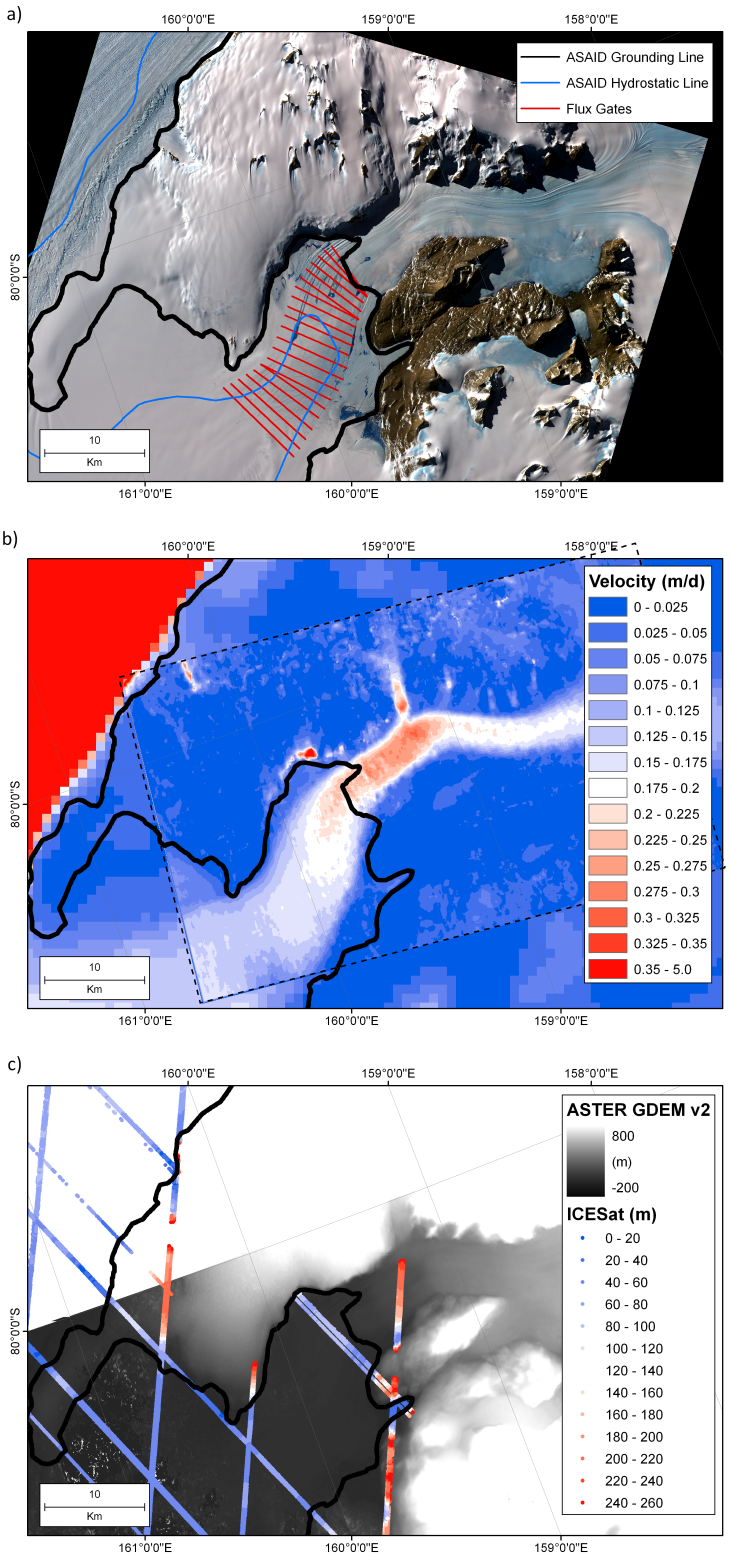

Figure 5.7: a) Flux Gates superimposed over an ASTER image, b) TerraSAR-X speckle tracking derived ice velocity (in dashed box) and MEaSUREs velocity data and c) ICESat Tracks and ASTER GDEM at the Darwin Glacier grounding line.

deviation of 7.6 m, however as radar data are not available to constrain the firn correction, there is a much higher uncertainty in overall discharge at this location. The glacier spreads significantly as it becomes buoyant and the ice shelf is heavily crevassed (Figure 5.8).

5.12 David Glacier

The David Glacier drains into the Drygalski Ice Tongue at $(75.4°S, 161.0°E)$. GPS measurements from the period 1991-1994 were made by Frezzotti et al. (1998) on the upper part of the floating ice on the David Glacier. These values are approximately 5-10% slower than recorded with TerraSAR-X in 2013 although TerraSAR-X velocities do agree closely with those derived from ASTER feature tracking from 2001 to 2006 (Stearns, 2011) with values of 542 ma^{-1} and 530 ma^{-1} at the grounding line respectively.

Published values for ice flux at the grounding line vary from 6.9 $\pm$ 0.6 km^3a^{-1} (Frezzotti et al., 2000) to 15.6 $\pm$ 1.0 km^3a^{-1} (Rignot and Thomas, 2002) and Wuite et al. (2009) predict melt rates of over 20 ma^{-1} close to the grounding line. Using the ASTER GDEM we calculate consistent values for melt rate of 10-12 ma^{-1} in the upper part of the fiord with 11.8 $\pm$ 3.6 ma^{-1} at line 'A' (Figure 5.9a) although due to the irregular shape of the grounding zone and highly variable ice flow velocities and crevassing in the region known as 'the cauldron' (e.g. Frezzotti et al., 2000) a precise discharge across the sinuous grounding line is difficult to calculate. Based on a discharge of 6.44 km^3a^{-1} at line A (Figure 5.9), and extrapolated average melt rate over the floating area upstream of this point of 15 $\pm$ 5 ma^{-1}, a discharge of 7.86 $\pm$ 0.48 km^3a^{-1} across the upper part of the grounding line is inferred. This is less than the mean accumulation from accumulation models, but does not account for additional discharge across the grounding zones at the sides of the fiord and ice from the slower northern branch.

5.13 Mackay Glacier

The Mackay is a very small outlet glacier feeding directly into a small ice tongue at $(77.0°S, 162.5°E)$. The area of the floating ice tongue over which melt rates can be calculated is less than 30 km^2. The glacier does not occupy an overdeepened fiord and so limited ice flux measurements are possible using the hydrostatic equilibrium

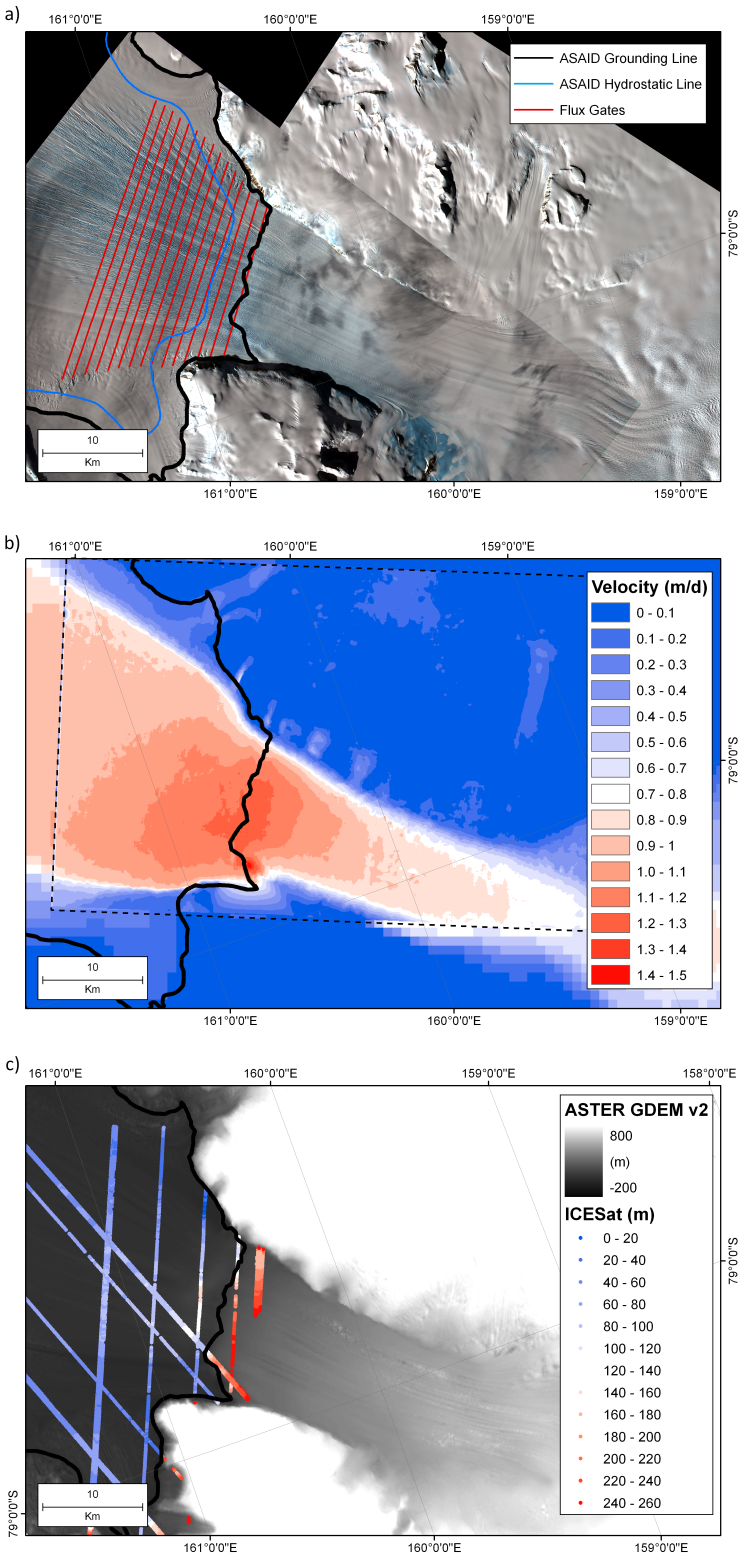

Figure 5.8: a) Flux Gates superimposed over an ASTER image, b) TerraSAR-X speckle tracking derived ice velocity (in dashed box) and MEaSUREs velocity data and c) ICESat Tracks and ASTER GDEM at the Mulock Glacier grounding line.

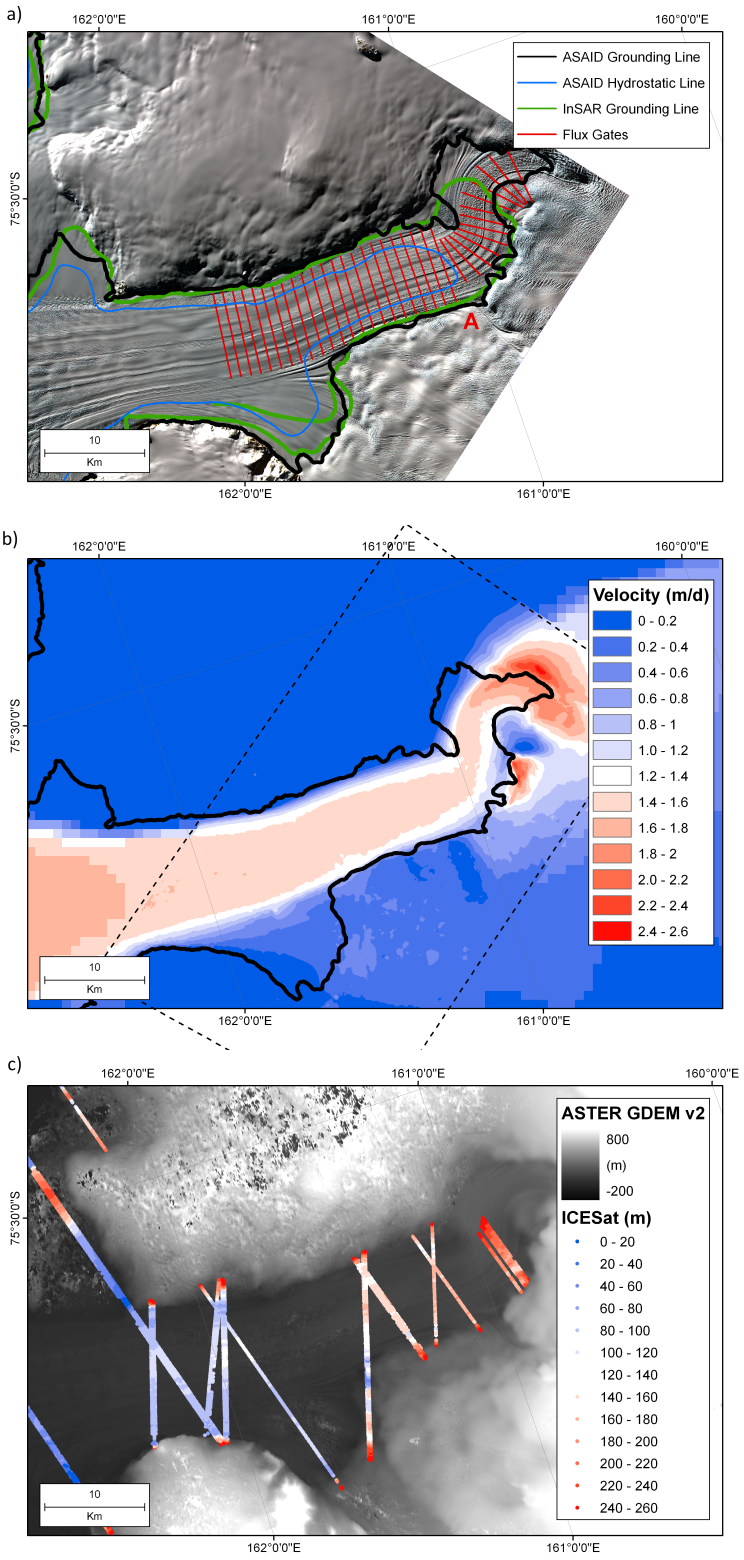

Figure 5.9: a) Flux Gates superimposed over an ASTER image, b) TerraSAR-X speckle tracking derived ice velocity (in dashed box) and MEaSUREs velocity data and c) ICESat Tracks and ASTER GDEM at the David Glacier grounding line.

method. A discharge value of 0.33 ± 0.06 km^3a^{-1} was noted by Frezzotti (1997) although this used estimates of thickness derived from measurement of icebergs originating from the Mackay ice tongue where significant melting may have already occurred (Keys and Fowler, 1989). We record a discharge of 0.20 km^3a^{-1} at the most downstream of our flux gates. Downstream of this point the ice tongue is visibly fractured and it is not clear whether ice is already lost to calving from the side of the ice tongue. Ice flux at the ASAID grounding line is greater than 1.0 km^3a^{-1} using the hydrostatic equilibrium assumption on the ASTER GDEM due to an estimated thickness of 2500m, which is clearly an overestimation based on the low surface velocity of ice upstream of the grounding line and the small catchment area. For comparison the BEDMAP-2 thickness is estimated at 341 m.

Unfortunately, ICESat tracks do not run perpendicular to the grounding line and interferograms lose coherence in the heavily crevassed grounding zone. Due to the rapidly changing velocity and surface slope in the grounding zone and additional uncertainty about the quality of the grounding line position on such a small glacier it is not possible to calculate representative values for basal melt rate using satellite methods alone.

5.14 Beardmore Glacier

The Beardmore Glacier at $83.5°S, 172°E$ has a curved grounding zone where it flows between the solid granite outcrops of Mt Hope and Mt. Kyffin, and surface elevation decreases steeply towards the grounding line where it meets the Ross Ice Shelf. The Beardmore Glacier velocity was measured in 1960-61 as 364.5 ma^{-1} (Swithinbank, 1963) and has changed little in the last 50 years when compared with 2010-11 measurements (Chapter 3). With a thickness of just under 1 km at the grounding line (Chapter 4) it discharges 4.8 km^3a^{-1} into the Ross Ice Shelf and produces estimated melt rate of 7.1 ± 3.3 ma^{-1} close to the grounding line.

5.15 Discussion

Melt rates at all locations are highest close to the grounding line, as would be expected by the greater ice thickness. Melt rates for all glaciers are also higher than beneath the Eastern Ross Ice Shelf around the Siple Coast (e.g. Catania et al., 2010), possibly due to the generally clockwise circulation in the Ross Ice Shelf cavity

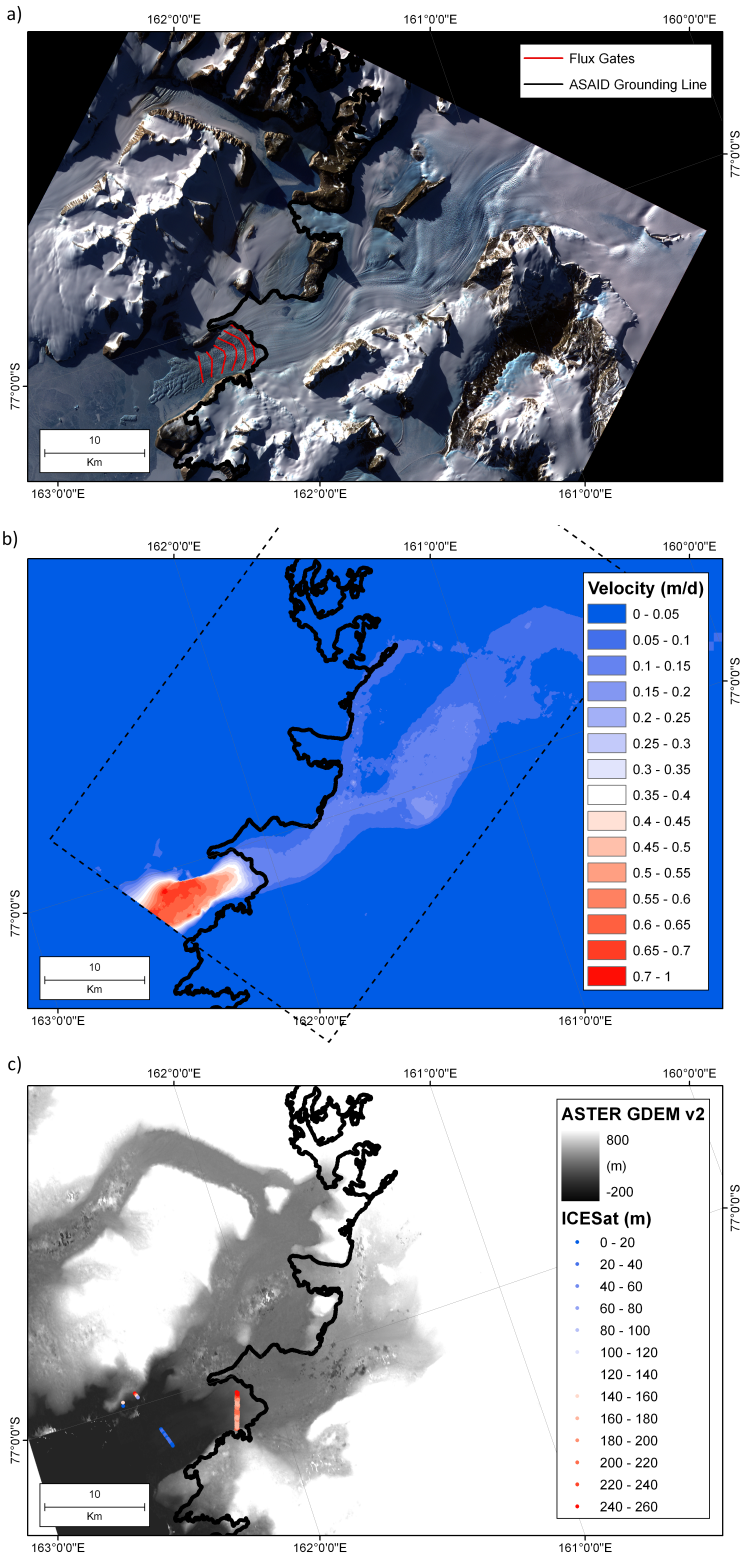

Figure 5.10: a) Flux Gates superimposed over an ASTER image, b) TerraSAR-X speckle tracking derived ice velocity (in dashed box) and MEaSUREs velocity data and c) ICESat Tracks and ASTER GDEM at the Mackay Glacier grounding line.

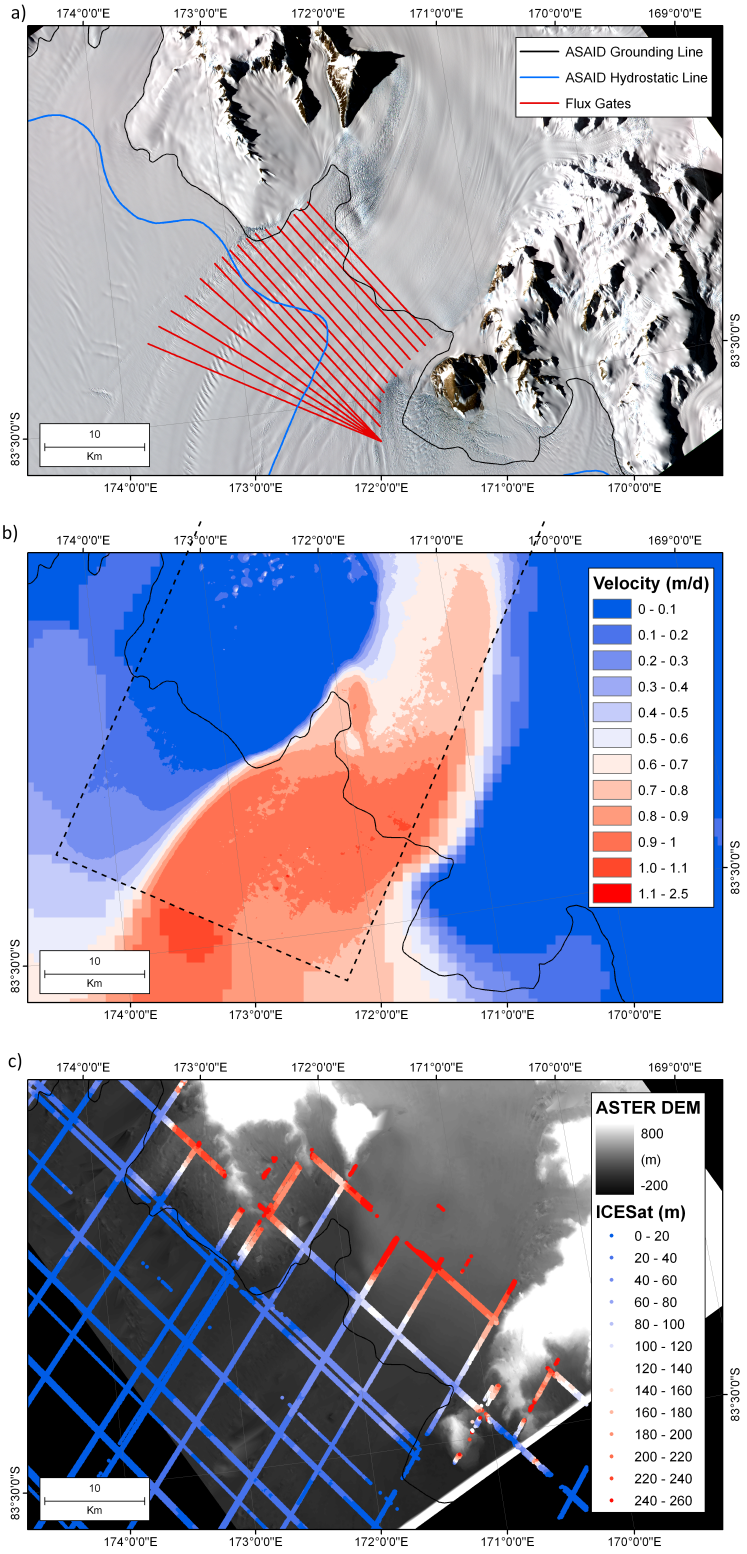

Figure 5.11: a) Flux Gates superimposed over an ASTER image, b) TerraSAR-X speckle tracking derived ice velocity (in dashed box) and MEaSUREs velocity data and c) ICESat Tracks and ASTER GDEM at the Beardmore Glacier grounding line.

Table 5.5: Ice thickness and velocity at the grounding line centreline; ice discharge at the grounding line from the hydrostatic equilibrium method and from linear and gaussian fit extrapolation of flux gates downstream of the grounding line; highest melt rates in the grounding zone; and net mass balance compared to average catchment wide accumulation from Table 5.1

Glacier	GL Thickness (m)			GL Velocity (ma^{-1})		GL Discharge (Gta^{-1})				Melt	Mass Balance
	Hydro. Eq.	BED-MAP2	GPR	TSX (12-3)	Rignot (07-9)	Hydro. Eq.	BED-MAP2	Extrap Lin.	Extrap. Gauss.	(ma^{-1})	(Gta^{-1})
Beardmore	904	803	921	343	368	4.74	3.34	3.97	4.40	7.1	+1.733
Darwin	849	705	983	95	65	0.288	0.240	0.300	0.291	1.4	+0.829
Mulock	1232	754	N/A	460	463	6.03	3.62	4.38	5.14	7.7	+1.600
Skelton	1770	696	1598	343	179	1.05	0.522	0.972	1.01	6.9	+0.030
Mackay	2778	341	N/A	59	68	0.893	0.091	N/A	N/A	N/A	+0.604*
David	1583	1161	N/A	891	695	5.91 †	4.27†	6.86	7.21	11.8	+4.74‡

* Discharge from BEDMAP-2 thickness used due to limited flux gates

† Discharge at point 'A', downstream of the grounding line

‡ Mass balance for the David Glacier does not include the discharge contribution from fiord sides or the northern branch of the glacier

(Reddy et al., 2010) and alternating deep grounding lines and thinner areas beneath the western Ross Ice Shelf. The observed pattern of melt rates close to the grounding line does not appear to be strongly related to latitude, however, but is dependent on localised effects of grounding zone structure, ice thickness, velocity and location relative to surrounding glaciers. Melt rates are broadly consistent across all glaciers, with slightly higher melt rates for the larger glaciers.

Melt rates on the Darwin Glacier are significantly lower than would be expected for their location and ice thickness based on the results for surrounding glaciers. A melt rate for the Byrd of 12 ± 2 ma^{-1} was given by (Kenneally and Hughes, 2003) but could be significantly higher at depth at the grounding line and the volume of freshwater produced here, driven north by the ice shelf cavity circulation, is thought to play an important role in the reduction in melt rate at the Darwin grounding line. The highest melt rates are observed at the grounding lines of the David and Mulock Glaciers, likely due to their greater depth at the distance from the grounding line where melt rates are calculated.

The 'flux gate' approach adopted here is a simple method of estimating melt rate where flow and thickness (or change in thickness) is expected to be relatively constant across the width of the glacier. Closely spaced flux gates allow an error estimation to be made and generally trends can be obtained through a fitting routine with extrapolation upstream to the grounding line. Although this is useful as a simple approximation of melt rate and pattern of change in melt rate with distance from the grounding line, it may smooth out local effects of ice shelf cavity shape and bathymetry (Williams et al., 2001).

Given that there is high uncertainty in thickness at the grounding line using the hydrostatic equilibrium assumption, melt rates are calculated using a weighting of ice fluxes further downstream. Melt rates observed here are sensitive to glacier velocity, particularly where the gradient in melt rate is high. By extrapolating the melt rates close to the hydrostatic line towards the grounding line (usually a fairly constant distance for ice of similar thickness), rapidly increasing melting upstream of this point is disregarded. The speed at which ice moves through the grounding zone therefore affects the amount of time that ice is subject to higher melt rates near the grounding line before reaching the measurement point. Ice in contact with warm ocean waters may melt at a constant rate at the grounding line, but the thickness gradient will become steeper as ice moves more slowly across this zone and is subject

to higher melt rates for longer.

The difference of over 10m between the modelled firn correction in van den Broeke (2008) and the best fit firn correction to radar data, both at the Skelton and the Darwin, highlights a significant weakness in estimating ice discharge and melt rate solely using satellite techniques. Error in firn correction of 10m may introduce an error in thickness of over 90m and corresponding error in glacier discharge. A greater problem in the calculation of melt rates, however, remains in identifying the local variability in firn correction and surface accumulation, particularly in steep topography. When attempting to calculate melt rates from surface freeboard data, an unmodelled local change in firn density at the surface of 1m per 1km, translates to a difference in observed melt rate of ± 3 ma^{-1} for a glacier moving at 300 ma^{-1}.

Chapter VI

Synthesis and Conclusions

The work presented here has focused on the outlet glaciers of the Transantarctic Mountains, and particularly the Beardmore Glacier. The methods developed in Chapters 2 to 4 are equally applicable elsewhere in Antarctica and can be used to constrain and compare both ice discharge at the grounding line and melting in the grounding zone. The main conclusions fall into two categories: conclusions about the applicability of the new satellite methodologies discussed here, fulfilling objectives 1-3 (Section 1.2), and conclusions about the mass balance and dynamics of Transantarctic Mountain outlet glaciers from objective 4.

This work shows that rapid changes in outlet glacier velocity may be observed close to their grounding lines on timescales of days and weeks, and further highlights the importance of high accuracy and repeatability for measurements of glacier flow (Chapter 3). The development of new and better remote sensing methods enables this repeatability across Antarctica. This research has shown the potential for new satellite techniques using existing sensors, as well as examining the limits on the applicability and inherent errors within each technique. This has been achieved using measurements from two field seasons on glaciers in the Transantarctic Mountains in combination with airborne and satellite data. The following section summarises the main conclusions from the work described in Chapters 2 to 5, identifying how each section contributes to the research aims outlined in Chapter 1 and develops our understanding of approaches to measure glacier mass-balance and dynamics in the grounding zone.

6.1 Grounding Line Position

One objective of this research was to identify possible new methods of identifying grounding line position. High resolution altimetry, such as the GLAS sensor on ICESat, now allows three methods of identifying the grounding line: the break of

slope technique (e.g. Fricker et al., 2009), the limit of flexure technique (e.g. Brunt et al., 2010a) and a new technique using the limit of downstream displacement of large scale surface features associated with the removal of shear stress below the grounding line as developed here (Marsh et al., 2012). This new technique is a by-product of the altimetry-based feature tracking method described, which produces consistent positive velocities over the ice-shelf but not over grounded ice. By identifying where internal stresses no longer deform the ice, information can be obtained about the point in the grounding zone at which ice completely loses contact with the bed. Identification of this point at which deformational stresses no longer affect the ice surface is important for modelling ice flow and the difference between this point and the upstream limit of flexure may provide useful additional information on grounding zone width and basal slope for modelling the grounding zone. Limitations with the GLAS sensor and orbit direction mean that it is not currently viable at all grounding lines but it should be considered as an additional application of satellite altimetry for monitoring grounding line movement when planning future satellite campaigns.

The grounding zone is also identified in Chapter 3 using TerraSAR-X imagery with the limit of flexure technique, but instead of looking directly at change in surface elevation, the relative change in displacement in satellite look direction is used as a proxy for displacement in the z direction assuming a constant horizontal velocity. This approach is well established using phase information, but here uses the same principles as interferometry except with amplitude speckle tracking, a method not well documented elsewhere. Although tidal motion recorded by speckle tracking is subject to greater noise levels than by interferometry, there are advantages in the grounding zone with high frequency sensors such as TerraSAR-X where phase information is often not continuous across highly crevassed regions and cannot be correctly and continuously unwrapped to a stationary point or ground control point.

As discussed in Section 1.4, comprehensive grounding line mapping has rapidly improved in the last couple of years, but it remains vital to develop methods of repeat grounding line mapping which are both readily repeatable and not as processing-intensive as interferometry in order to identify grounding line migration and predict ice sheet stability. The techniques described in Chapters 2 and 3 make progress towards these easily repeatable and automated grounding line mapping methods.

6.2 Grounding Zone Velocity

Velocity fluctuations related to ocean tides have been observed in GPS records at the grounding zones of fast-flowing ice streams for the last decade (Anandakrishnan et al., 2003; Bindschadler et al., 2003; Gudmundsson, 2006). Velocity information collected and processed from GPS receivers on the Beardmore Glacier shows that diurnal tides which dominate in the Ross Sea also produce fluctuations for East Antarctic outlet glaciers constrained by rock at their margins. The Beardmore Glacier has significantly higher surface slopes and expected basal shear stresses than at previous study sites where high-resolution GPS surveys have been conducted. The observed velocity changes are directly correlated with the tidal amplitude but are damped more rapidly upstream of the grounding line than on the Rutford Ice Stream, where detailed measurements have been made previously (King et al., 2010; Gudmundsson, 2006). While exhibiting a stronger damping upstream, potentially due to higher basal shear stress, phase analysis shows a similar pattern in delayed response and propagation of velocity changes upstream.

For the first time these tidal velocity fluctuations, which are evident in GPS data, are observed in satellite imagery from repeat TerraSAR-X speckle tracking measurements. Although the magnitude of the expected and observed velocity change at the Beardmore is approximately equal to the resolution for this technique, elsewhere in Antarctica the tidal range is greater, and TerraSAR-X may allow a more detailed spatial analysis of short term velocity fluctuations. Differences in ground-based GPS data allow us to quantify the fluctuation accurately over time, but satellite methods as demonstrated here will allow the spatial extent of these patterns to be mapped. The effect of these tidally-induced modulations on satellite measurements at other frequencies is also described, and it will become increasingly important to add tidal models into velocity calculations and to stack multiple pairs of images with consideration of their acquisition date relative to tides to calculate annual velocities for short-repeat-interval satellites, without introducing a tide-dependent bias. The GPS data acquired and processed here provide valuable additional tidal information in a new region of Antarctica for use in the development of models of how glaciers respond to ocean tides in different settings.

Altimetry-based velocity estimation is also investigated for the grounding zone of the Beardmore Glacier and the Ross Ice Shelf in Chapter 2 and although issues

with the orbital repeat accuracy of ICESat and low spatial resolution mean that it is not currently possible to improve on the accuracy of InSAR measurements in this area, this technique has the advantage of accurate spatial geolocation of the resulting velocities and is a promising technique for calibration of InSAR and feature tracking velocity measurements. With future altimeters with improved across-track positioning it will be possible to simultaneously calculate ice thickness change and velocity over ice shelves with a single sensor.

6.3 Grounding Zone Ice Thickness

A new technique for inferring ice thickness at the grounding line and in the grounding zone has been developed based on the assumption that ice thickness has the greatest influence on ice rigidity, which in turn influences how oceanic tidal forcing is observed in the pattern of vertical flexure seen in differential interferograms (Chapter 4). Demonstration that the ill-posedness of the inverse formulation of the Euler-Bernoulli equations for bending can be overcome and produce stable ice thickness maps is the first step towards a fully independent satellite remote sensing technique for measuring ice thickness in this sensitive area.

An elastic-plate model is shown to perform well in the grounding zone of the Beardmore Glacier. This method is an alternative to the more regularly used 'hydrostatic equilibrium' assumption, and avoids potential issues with inaccuracies in surface DEMs. Accurate identification of mean ocean surface height, which is difficult beneath large ice shelves, along with geoid and firn correction information is not needed. The inverse model is shown to be robust when regularisation is applied and produces consistent results in one- and two-dimensional sensitivity studies. Although working well and resolving thickness variation across the relatively linear grounding zone of the cold based Beardmore Glacier, the application of this model to additional grounding zones requires further investigation of how ice rheology varies between grounding zones and over what tidal periods the assumption of purely elastic deformation is applicable. Where ice temperatures are higher and viscous response more important it is expected that a time-dependent model of ocean forcing will be required.

The inverse model is shown to recreate flexure for an irregular 2-D geometry with steadily varying thickness but further work needs to be done to investigate

how particularly irregular shaped grounding zones perform in the inverse model. In an extreme case, tidal forcing is heavily damped in narrow fiord-type grounding zones such as the Skelton Glacier (Figure 5.4). The shape of the grounding zone is especially important where ice flow is parallel to the grounding line and shearing at lateral margins has a large effect on ice rigidity and therefore calculated thickness.

Ice discharge and melt rates calculated from the modelled thickness (Figure 4.8) and ice discharge and melt rates from the hydrostatic equilibrium flux gate extrapolation are in good agreement, with modelled thickness showing slightly higher melt rates close to the grounding line than with the extrapolation technique but significantly lower than where ice is assumed to be in hydrostatic equilibrium throughout the grounding zone. The modelled thickness should allow better quantification of melt rates and melting distribution where large spatial variability in melt rates might be expected. This remains to be tested at locations where more validation data are available.

6.4 Grounding Zone Mass-Balance in the Transantarctic Mountains

On the Beardmore Glacier, velocity at the grounding line was the same in 2010 as in 1960 to within 1%. The flow of the Beardmore Glacier therefore appears unaffected by the recent and continuing deceleration of the nearby Mercer and Whillans Ice Streams, which has caused a decrease in ice shelf velocity of over 50 ma^{-1} more than 500 km downstream of the grounding line (Joughin et al., 2002; Catania et al., 2012; Scheuchl et al., 2012). Velocity measurements from the nearby Byrd Glacier also show no detectable long-term changes in speed between 1960 and 2005 (Stearns et al., 2008). This long time-series suggests that despite a small increase in accumulation over central East Antarctica since the 1960s (Frezzotti et al., 2013), glaciers in this region are currently not experiencing major changes in their outflow. Similar stability has been observed at other high latitude sites feeding the Ronne-Filchner Ice Shelf (Gudmundsson and Jenkins, 2009; Scheuchl et al., 2012).

For the Mulock Glacier, while Stearns (2011) recorded acceleration at the grounding line between 2001 and 2007, the TerraSAR-X observed velocities from 2013 are close to 2001-02 levels, suggesting that the earlier increase in velocity was likely a local and short-term effect not related to any wider change in ice sheet dynamics. Further north on the David Glacier, a comparison between GPS velocities from 1991-

94 (Frezzotti et al., 1998) against 2013 TerraSAR-X data shows a slight decrease in glacier velocity close to the grounding line (3.5%) but comparison with satellite data along the centreline from 2001-06 suggest no significant change in velocity since this period (Stearns, 2011). The Transantarctic Mountain outlet glaciers currently show stability without noticeable increase in discharge in response to increased accumulation or deceleration of the Ross Ice Shelf (Chapter 5). Any long-term changes in velocity are therefore within the range of velocities that may occur over tidal periods, further reinforcing the need for reliable modelling of short-term fluctuations and better interpretation of satellite data.

Conclusions on distribution of basal melt rates may also be made on the evidence presented here from Transantarctic Mountain outlet glaciers. Generally uncertainties in melt rate calculations are high using the hydrostatic equilibrium technique due to the variability in DEM accuracy around the steep margins of Antarctica and at the grounding line. Uncertainties are particularly high where no radar-derived ice thickness data are available to constrain the measurements. Large differences between published estimates of firn density and those calibrated using radar measurements highlight the need for much improved local atmospheric modelling or satellite techniques for identifying snow distribution and redistribution before satellite measurements of ice thickness can be relied on using the hydrostatic equilibrium assumption. The highest confidence in melt rates were obtained for ice draining from the Skelton Glacier, with a melt rate near the grounding line of 6.86 ± 2.6 ma^{-1}. This is significantly higher than the average modelled for the Ross Ice Shelf, but lower than at grounding lines elsewhere in Antarctica. Despite this relatively low melt rate, approximately half of the ice discharged across the grounding line is lost within the first 40 km, before reaching the ice shelf. Holland et al. (2003) suggest the highest melt rates beneath the Ross Ice Shelf should occur on the western side of the cavity south of Ross Island where the water column is thickest. Although this does seem to be the case when comparing melt rates with estimates from the Eastern Ross Ice Shelf, there does not appear to be a significant influence on melt rate due to location, with a greater influence due to ice thickness at the grounding line. This is related to the depression of relative melting point due to increased pressure. Melting depends very much on the geometry of the ice shelf cavity and the proximity of the continental shelf break but reasonably consistent melt rates for the outlet glaciers in this study suggest that ocean temperatures and properties are

also relatively consistent in this region. A noticeably smaller melt rate is observed at the grounding line of the Darwin-Hatherton glacier system relative to the other glaciers, despite its similar thickness, thought to be related to the close proximity of outflow and freshwater input from the much larger and rapidly melting Byrd Glacier (Kenneally and Hughes, 2003). Continued monitoring of the discharge of these glaciers is needed to predict the future response to increased snowfall and observe changes in the ice shelf. Improved observations leading to better calculations of melt rates are also needed to improve constraints on ocean cavity models at this significant boundary.

6.5 Implications for Future Work

The use of altimetry on ice shelves to map surface flow has been demonstrated in Chapter 2 using the Geoscience Laser Altimetry System from the ICESat mission. This approach has only recently become possible from satellite due to the high vertical precision of the elevation data and reliability in repeat coverage, but the technique described here loses resolution due to problems associated with across-track slope and a high spatial separation of crossing points. The concept for NASA's Advanced Topographic Laser Altimeter System (ATLAS) aboard ICESat-2, now scheduled for launch in 2016 (NASA, 2013), solves many of the problems highlighted here: by including multiple beams across-track it will be able to identify surface slope on individual passes and increase the proximity of repeat ground-tracks to original ground-tracks; by decreasing the footprint size it will better resolve small surface features; and by increasing the sampling interval from 40 Hz to 10 kHz, along track resolution will be improved to <1m (McGill et al., 2013). A modification of the technique described here may be able to provide unprecedented accuracy in both vertical and horizontal movement over Antarctic ice shelves.

As the resolution of velocity measurements over ice shelves and in the grounding zone increases, the effect of short-term velocity fluctuations on satellite-derived annually-averaged velocities will be increased. Future satellites such as the C-band SAR ESA Sentinel-1A and 1B are planned to continue the good coverage of grounding zones provided by the ERS and Radarsat missions, and the C-band frequency will increase the likelihood of coherence in the grounding zone. The Sentinel 1-A satellite is planned for launch in 2013 with a revisit period of 12 days. Its twin

satellite, Sentinel 1-B, will fly in the same orbital plane ± 50 m (Geudtner et al., 2012) but 180°out of phase in orbit, reducing the repeat interval for InSAR from the combined satellite array to only 6 days. It is shown in Chapter 3 that longer revisit periods such as the 11 days of TerraSAR-X improve the smoothing of short-term fluctuations in velocity in comparison to the 3 days of ERS-1/2. While an interval of 6 days will not greatly improve the identification of diurnal change over TerraSAR-X it is close to the ideal repeat interval to more easily identify fortnightly velocity fluctuations and their spatial distribution, particularly on glaciers with a strong fortnightly response (Gudmundsson, 2006).

While new satellites may improve on the widespread repeatability of velocity measurements, knowledge of the pattern in diurnal signals will remain most accurately identifiable in ground-based GNSS data. It would be of interest to instrument the outlet glaciers in the Transantarctic Mountains for a longer period and at higher resolution in the grounding zone to assess the different effects of similar diurnal tides on glacier grounding zones with different geometry and confirm the applicability of a model of basal shear stress and sliding. There is a markedly damped oscillation in velocity in GPS data from the Skelton Glacier in comparison to the Beardmore Glacier, but it has not yet been possible to record the short-term fluctuations further north and make any inferences about the relative importance of local bathymetry and/or glacier grounding zone characteristics for these oscillations.

ALOS-2, also planned for launch in 2013, has a revisit period of 14 days and will ensure the extended availability of SAR imagery and along with the Sentinel and TerraSAR-X missions will continue to provide the possibility of differential interferograms at outlet glacier grounding zones. The inverse model of elastic flexure has shown that it is possible to resolve ice thickness using these differential interferograms on relatively cold glaciers by estimating an 'effective Young's Modulus' to relate ice stiffness to thickness. More work is needed in this area to identify whether this model is universally applicable or whether a model using visco-elastic rheology could be inverted for thickness in other areas. Grounding zones with stable or zero velocity, for instance around ice rises and stagnant ice shelves, and multiple coherent interferograms could be used to identify the pattern of delayed elastic response or observe 'effective change in ice stiffness' in an elastic model related to viscous deformation under certain tidal periods.

Although the flexure technique improves measurements of grounding zone ice

thickness, calculating melt rates over ice shelves remotely requires high resolution DEMs. The TanDEM-X and TerraSAR-X constellation will provide significantly better coverage and spatial resolution than the best DEMs currently available over Antarctica, with better than 10m absolute vertical accuracy and 2m relative vertical accuracy at a horizontal resolution of 12m (Krieger et al., 2005). This DEM is currently in acquisition and should be available from 2014. Combined with the accurate altimetry of ICESat-2 and improved resolution atmospheric modelling and knowledge of firn densification it should become possible to also better constrain the variability of the firn layer in grounding zones.

While improved satellite techniques will provide better estimates of melt rates beneath ice shelves, the grounding zone ice thickness will never be accurately characterised using the hydrostatic assumption alone. This work has shown the applicability of an inverse model to predict ice thickness on the Beardmore Glacier which improves on this hydrostatic assumption. Application of this model to other glaciers and for other tidal periods will allow a better estimate of glacier thickness in comparison to the hydrostatic method. This technique will not supercede ice thickness measurements by radar for high spatial resolution or for validation, but in combination with the better quantification of short-term velocity change identified here, it will improve on current estimates of melt rates and glacier discharge for widespread applicability. Improvements to measurements of ice discharge and mass balance are vital for measuring change and will only be known accurately everywhere by improving methods of measuring ice thickness and velocity from satellite, as demonstrated here.

Bibilography

Abdalati, W., H.J. Zwally, R. Bindschadler, B. Csatho, S.L. Farrell, H.A. Fricker, D. Harding, R. Kwok, M. Lefsky, T. Markus, A. Marshak, T. Neumann, S. Palm, B. Schutz, B. Smith, J. Spinhirne and C. Webb, 2010. The ICESat-2 laser altimetry mission, Proceedings of the IEEE, 98(5), 735-751, doi:10.1109/JPROC.2009.2034765.

Abdalati, W. and W.B. Krabill, 1999. Calculation of ice velocities in the Jakobshavn Isbrae area using airborne laser altimetry, Remote Sensing of Environment, 67, 194-204, doi:10.1016/S0034-4257(98)00086-8.

Alberti, M. and D. Biscaro, 2010. Height variation detection in polar regions from ICESat satellite altimetry, Computers and Geosciences, 36, 1-9, doi:10.1016/j.cageo.2009.07.002.

Albrecht, N., R. Vennel, M. Williams, C. Stevens, P. Langhorne, G. Leonard and T. Haskell, 2006. Observation of sub-inertial internal tides in McMurdo Sound, Antarctica, Geophysical Research Letters, 33, L24606, doi:10.1029/2006GL027377.

Anandakrishnan, S., D.D. Blakenship, R.B. Alley and P.L. Stoffa, 1998. Influence of subglacial geology on the position of a West Antarctic ice stream from seismic observations, Nature, 394(6688), 62-65, doi:10.1038/27889.

Anandakrishnan, S., D.E. Voigt, R.B. Alley and M.A. King, 2003. Ice stream D flow speed is strongly modulated by the tide beneath the Ross Ice Shelf, Geophysical Research Letters, 30, doi:10.1029/2002GL016329

Arabelos, D.N. and C.C. Tscherning, 2010. A comparison of recent Earth gravitational models with emphasis on their contribution in refining the gravity and geoid at continental or regional scale, Journal of Geodesy, 84(11), 643-660, doi:10.1007/s00190-010-0397-z.

Arthern, R.J., D.P. Winebrenner and D.G. Vaughan, 2006. Antarctic snow accumulation mapped using polarization of 4.3-cm wavelength microwave emission, Journal of Geophysical Research, 111(D6), D06107, doi:10.1029/2004JD005667.

Assmann, K., H.H. Hellmer and A. Beckmann, 2003. Seasonal variation in circulation and water mass distribution on the Ross Sea continental shelf, Antarctic Science, 15(1), 3-11, doi:10.1017/S0954102003001007.

ERSDAC, 2011. ASTER GDEM Version 2 Validation Report, published online at http://www.jspacesystems.or.jp/ersdac/GDEM/ver2Validation/.

Baessler, M., R. Rosenau, R. Dietrich, K. Shibuya and K. Doi, 2012. Utilizing InSAR for the measurement of ice flow velocities and ocean tide induced height changes of ice shelves at their grounding zones and surroundings, Proc. IEEE Int. Geoscience and Remote Sensing Symposium (IGARSS), Munich, July 2012, 3249-3252.

Bamber, J.L., Gomez-Dans, J.L. and Griggs, J.A., (2009), A new 1km digital elevation model of the Antarctica derived from combined satellite radar and laser data Part 1: Data and methods, The Cryosphere, 3, 101-111, doi:10.5194/tc-3-101-2009.

Bindschadler, R.A., M.A. King, R.B. Alley, S. Anandakrishnan and L. Padman, 2003. Tidally controlled stick-slip discharge of a West Antarctic ice stream. Science, 301(5636), 1087-1089, doi:10.1126/science.1087231.

Bindschadler, R., H. Choi, A. Wichlacz and 15 others, 2011. Getting around Antarctica: new high-resolution mappings of the grounded and freely-floating boundaries of the Antarctic Ice Sheet created for the International Polar Year, Cryosphere, 5(3), 569-588, doi:10.5194/tc-5-569-2011.

Bindschadler, R., Vaughan, D.G. and Vornberger, P., 2011. Variability of basal melt beneath the Pine Island Glacier ice shelf, West Antarctica, Journal of Glaciology, 57(204), 581-595, doi:10.3189/002214311797409802.

Bindschadler, R.A. and T.A. Scambos, 1991. Satellite-image-derived velocity field of an Antarctic Ice Stream, Science, 252(5003), 242-246, doi:10.1126/science.252.5003.242.

Bintanja, R., G.J. van Oldenborgh, S.S. Drijfhout, B. Wouters and C.A. Katsman, 2013. Important role for ocean warming and increased ice-shelf melt in Antarctic sea-ice expansion, Nature Geoscience, 6, 376-379, doi:10.1038/ngeo1767.

Boening, C., M. Lebsock, F. Landerer and G. Stephens, 2012. Snowfall-driven mass change on the East Antarctic ice sheet, Geophysical Research Letters, 39, L21501, doi:10.1029/2012GL053316.

Bohlander, J. and T. Scambos, 2007. Antarctic coastlines and grounding line derived from MODIS Mosaic of Antarctica (MOA), Boulder, Colorado USA: National Snow and Ice Data Center, Digital Media, 2007.

Breit, H., T. Fritz, U. Balss, M. Lachaise, A. Niedermeier and M. Vonavka, 2010. TerraSAR-X SAR Processing and Products, IEEE TGRS, 48(2), 727-740, doi:10.1109/TGRS.2009.2035497.

Brunt, K.M., H.A. Fricker, L. Padman, T.A. Scambos, S. O'Neel, 2010. Mapping the grounding zone of the Ross Ice Shelf, Antarctica, using ICESat laser altimetry, Annals of Glaciology, 51(55), 71-79, doi:10.3189/172756410791392790.

Brunt, K.M., M. King, H.A. Fricker and D.R. MacAyeal, 2010. Flow of the Ross Ice Shelf, Antarctica, is modulated by the ocean tide. Journal of Glaciology, 56(195), 157-161, doi:10.3189/002214310791190875.

Brunt, K.M., H.A. Fricker and L. Padman, 2011. Analysis of ice plains of the Filchner-Ronne Ice Shelf, Antarctica, using ICESat laser altimetry, Journal of Glaciology, 57(205), 965-975, doi:10.3189/002214311798043753.

Budd, W., 1966. The dynamics of the Amery Ice Shelf, Journal of Glaciology, 6(45), 335-358.

Burgess, D.O., M.J. Sharp, D.W.F. Mair, J.A. Dowdeswell and T.J. Benham, 2005. Flow dynamics and iceberg calving rates of Devon Ice Cap, Nunavut, Canada, Journal of Glaciology, 51, 219–230, doi:10.3189/172756505781829430.

Cameron, R.L. and R.P. Goldthwait, 1961. The US-IGY contribution to Antarctic Glaciology, International Association of Scientific Hydrology, 55, 7-13.

Carabajal, C.C., 2011. ASTER global DEM version 2.0 evaluation using ICESat geodetic ground control. Report to the ASTER GDEM Version 2 Validation Team. Available online at www.jspacesystems.or.jp/ersdac/GDEM/E/4.html

Catania, G., C. Hulbe and H. Conway, 2010. Grounding-line basal melt rates determined using radar-derived internal stratigraphy, Journal of Glaciology, 56(197), 545-554, doi:10.3189/002214310792447842.

Catania, G., C. Hulbe, H. Conway, T.A. Scambos and C.F. Raymond, 2012. Variability in the mass flux of the Ross Sea ice streams, Antarctica, over the last millennium, Journal of Glaciology, 58, 741-751, doi:10.3189/2012JoG11J219.

Chen, J.L., C.R. Wilson, D. Blankenship and B.D. Tapley, 2009. Accelerated Antarctic ice loss from satellite gravity measurements, Nature Geoscience, 2(12), 859-862, doi:10.1038/ngeo694.

Collins, I.F., and C.W.M. Swithinbank, 1968. Rifts at the foot of the Beardmore Glacier, Antarctica, Union de Geodesie, 109-114.

Conway, H., B.L. Hall, G.H. Denton, A.M. Gades and E.D. Waddington, 1999. Past and future grounding-line retreat of the West Antarctic Ice Sheet, Science, 286(5438), 280-283, doi:10.1126/science.286.5438.280.

Cook, A.J., A.J. Fox, D.G. Vaughan and J.G. Ferrigno, 2005. Retreating glacier fronts on the Antarctic Peninsula over the past half-century, Science, 308(5721), 541-544, doi:10.1126/science.1104235.

Cook, A.J., T. Murray, A. Luckman, D.G. Vaughan and N.E. Barrand, 2012. A new 100-m digital elevation model of the Antarctic Peninsula derived from ASTER

Global DEM: methods and accuracy assessment, Earth System Science Data, 4, 129-142, doi:10.5194/essd-4-129-2012.

Corr, H.F.J., C.S.M. Doake, A. Jenkins and D.G. Vaughan, 2001. Investigations of an 'ice plain' in the mouth of Pine Island Glacier, Antarctica, Journal of Glaciology, 47, 51-57, doi:10.3189/172756501781832395.

Corr, H.F.J., A. Jenkins, K.W. Nicholls and C.S.M. Doake, 2002. Precise measurement of changes in ice-shelf thickness by phase-sensitive radar to determine basal melt rates, Geophysical Research Letters, 29(8), L01232, doi:10.1029/2001GL014618.

Csatho, B., Y. Ahn, T. Yoon, C.J. van der Veen, S. Vogel, G. Hamilton, D. Morse, B. Smith and V.B.Spikes, 2005. ICESat measurements reveal complex pattern of elevation changes on Siple Coast ice streams, Antarctica, Geophysical Research Letters, 32, L23S04, doi:10.1029/2005GL024289

Cuffey, K.M and Paterson, W.S.B., 2010. The Physics of Glaciers, 4th Edition. Elsevier.

Davis, C.H., Y.H. Li, J.R. McConnell, M.M. Frey and E. Hanna, 2005. Snowfall-driven growth in East Antarctic ice sheet mitigates recent sea-level rise, Science, 308(5730), 1898-1901, doi:10.1126/science.1110662.

Doake, C.S.M., H.F.J. Corr, K.W. Nicholls, A. Gaffikin, A. Jenkins, W.I. Bertiger and M.A. King, 2002. Tide-induced lateral movement of Brunt Ice Shelf, Antarctica, Geophysical Research Letters, 29, 1226, doi:1029/2001GL014606.

DiMarzio, J., A. Brenner, R. Schutz, A. Shuman and H.J. Zwally, 2007. GLAS/ICESat 500m laser altimetry digital elevation model of Antarctica. Boulder, Colorado, USA: National Snow and Ice Data Center.

Drosg, M., 2009. Dealing with uncertainties: a guide to error analysis, 2nd ed., 235 pp., Springer, Dordrecht, New York.

Dutrieux, P., D.G. Vaughan, H.F.J. Corr, A. Jenkins, P.R. Holland, I. Joughin and A. Fleming, 2013. Pine Island Glacier ice shelf melt distributed at kilometre scales, The Cryosphere Discuss, 7, 1591-1620, doi:10.5194/tcd-7-1591-2013.

Erofeeva, S.Y., L. Padman and G. Egbert, 2005. Assimilation of ship-mounted ADCP data for barotropic tides: application to the Ross Sea, Journal of Atmospheric and Oceanic Technology, 22(6), 721-734, doi:10.1175/JTECH1735.1.

Evans, S., 1963. Radio-echo techniques for the measurement of ice thickness, Polar Record, 11, 406-410.

Förste, C., R. Schmidt, R. Stubenvoll, F. Flechtner, U. Meyer, R. König, H. Neumayer, R. Biancale, J.M. Lemoine, S. Bruinsma, S. Loyer, F. Barthelmes and S. Esselborn, 2008. The GeoForschungsZentrum Potsdam/Groupe de Recherche de Gèodésie Spatiale satellite-only and combined gravity field models: EIGEN-GL04S1 and EIGEN-GL04C, Journal of Geodesy, 82, 331-346, doi:10.1007/s00190-007-0183-8.

Fretwell, P., H.D. Pritchard, D.G. Vaughan and 57 others, 2013. Bedmap2: improved ice bed, surface and thickness datasets for Antarctica. Cryosphere, 7, 375-393, doi:10.5194/tc-7-375-2013.

Frezzotti, M., 1997. Ice front fluctuation, iceberg calving flux and mass balance of Victoria Land glaciers, Antarctic Science, 9(1), 61-73, doi:10.1017/S0954102097000096.

Frezzotti, M., A. Capra and L. Vittuari, 1998. Comparison between glacier ice velocities inferred from GPS and sequential satellite images, Annals of Glaciology, 27, 54-60.

Frezzotti, M., I.E. Tabacco and A. Zirizotti, 2000. Ice discharge of eastern Dome C drainage area, Antarctica, determined from airborne radar survey and satellite image analysis, Journal of Glaciology, 46(153), 253-264, doi:10.3189/172756500781832855.

Frezzotti, M., S. Gandolfi and S. Urbini, 2002. Snow megadunes in Antarctica: sedimentary structure and genesis, Journal of Geophysical Research, 107, (D18), 4344, doi:10.1029/2001JD000673.

Frezzotti, M., C. Scarchilli, S. Becagli, M. Proposito and S. Urbini, 2013. A synthesis of the Antarctic surface mass balance during the last 800 yr, The Cryosphere, 7, 303-319, doi:10.5194/tc-7-303-2013.

Fricker, H.A., J.N. Bassis, B. Minster and D.R. MacAyeal, 2005. ICESat's new perspective on ice shelf rifts: the vertical dimension, Geophysical Research Letters, 32, L23S08, doi:10.1029/2005GL025070.

Fricker, H.A., R. Coleman, L. Padman, T.A. Scambos, J. Bohlander and K.M. Brunt, 2009. Mapping the grounding zone of the Amery Ice Shelf, East Antarctica using InSAR, MODIS and ICESat, Antarctic Science, 21(5), 515-532, doi:10.1017/S095410200999023X.

Fricker, H.A. and L. Padman, 2006. Ice shelf grounding zone structure from ICESat laser altimetry, Geophysical Research Letters, 33, L15502, doi:10.1029/2006GL026907.

Fujita, S., T. Matsuoka, T. Ishida, K. Matsuoka and S. Mae, 2000. A summary of the complex dielectric permittivity of ice in the megahertz range and its application for radar sounding of polar ice sheets, Physics of Ice Core Records, Edited by T. Hondoh, Hokkaido University Press, Sapporo, 185-212.

Geudtner, D., P. Pontin, R. Torres, P. Snoeij and D. Bibby, 2012. Overview of the GMES Sentinel-1 Mission, Proceedings of EUSAR 2012, Nuremberg, Germany.

Giles, A.B., R.A. Massom and R.C. Warner, 2009. A method for sub-pixel scale feature-tracking using Radarsat images applied to the Mertz Glacier Tongue, East Antarctica, Remote Sensing of Environment, 113, 1691-1699, doi:10.1016/j.rse.2009.03.015.

Gille, S.T., 2002. Warming of the Southern Ocean since the 1950s, Science, 295(5558), 1275-1277, doi:10.1126/science.1065863.

Gille, S.T., 2008. Decadal-scale temperature trends in the Southern Hemisphere ocean, Journal of Climate, 21(18), 4749-4765, doi:10.1175/2008JCLI2131.1.

Glasser, N.F. and T.A. Scambos, 2008. A structural glaciological analysis of the 2002 Larsen B Ice Shelf collapse, Journal of Glaciology, 54, 3-15, doi:10.3189/002214308784409017.

Gogineni, S., T. Chuah, C. Allen, K. Jezek and R.K. Moore, 1998. An improved coherent radar depth sounder. Journal of Glaciology, 44(148), 659-669.

Gogineni, P., 2012. CReSIS Radar Depth Sounder Data, Lawrence, Kansas, USA. Digital Media. http://data.cresis.ku.edu/.

Goldstein, R.M, H. Engelhardt, B. Kamb and R.M. Frolich, 1993. Satellite radar interferometry for monitoring ice sheet motion: application to an Antarctic Ice Stream. Science, 262(5139), 1525-1530, doi:10.1126/science.262.5139.1525.

Golledge, N.R., O.J. Marsh, W. Rack, D. Braaten and R.S. Jones, submitted. Basal conditions of two Transantarctic Mountain outlet glaciers from observation-constrained diagnostic modelling, Journal of Glaciology

Gray, L., N. Short, R. Bindschadler, I. Joughin, L. Padman, P. Vornberger and A. Khananian, 2002. RADARSAT interferometry for Antarctic grounding-zone mapping, Annals of Glaciology, 34, 269-276, doi:10.3189/172756402781817879.

Griggs, J.A. and J.L. Bamber, 2009. A new 1km digital elevation model of Antarctica derived from combined radar and laser data - Part 2: Validation and error estimates, The Cryosphere, 3(1), 113-123, doi:10.5194/tc-3-113-2009.

Griggs, J.A. and J.L. Bamber, 2011. Antarctic ice-shelf thickness from satellite radar altimetry. Journal of Glaciology, 57(203), 485-498, doi:10.3189/002214311796905659.

Gudmundsson, G.H., 2003. Transmission of basal variability to a glacier surface, Journal Geophysical Research, 108, B52253, doi:10.1029/2002JB002107.

Gudmundsson, G.H., 2006. Fortnightly variations in the flow velocity of Rutford Ice Stream, West Antarctica. Nature, 444(7122), 1063-1064, doi:10.1038/nature05430.

Gudmundsson, G.H., 2007. Tides and flow of Rutford ice stream, West Antarctica. Journal of Geophysical Research, 112(F4), F04007, doi:10.1029/2006JF000731.

Gudmundsson, G.H., 2011. Ice-stream response to ocean tides and the form of the basal sliding law, The Cryosphere, 5, 259–270, doi:10.5194/tc-5-259-2011.

Gudmundsson, G.H. and A. Jenkins, 2009. Ice-flow velocities on Rutford Ice Stream, West Antarctica, are stable over decadal timescales, Journal of Glaciology, 55(190), 339-344, doi:10.3189/002214309788608697.

Hattermann, T., O.A. Nost, J.M. Lilly and L.H. Smedsrud, 2012. Two years of oceanic observations below the Fimbul Ice Shelf, Antarctica, Geophysical Research Letters, 39, L12605, doi:10.1029/2012GL051012.

Haug, T., A. Kaab and P. Skvarca, 2010. Monitoring ice shelf velocities from repeat MODIS and Landsat data a method study on the Larsen C ice shelf, Antarctic Peninsula, and 10 other ice shelves around Antarctica, The Cryosphere, 4, 161-178, doi:10.5194/tc-4-161-2010.

Heliere, F., C.C. Lin, H. Corr and D. Vaughan, 2007. Radio echo sounding of Pine Island Glacier, West Antarctica: aperture synthesis processing and analysis of feasibility from space, IEEE Transactions on Geoscience and Remote Sensing, 45(8), 2573-2582, doi:10.1109/TGRS.2007.891433.

Hellmer, H.H., 2004. Impact of Antarctic ice shelf basal melting on sea ice and deep ocean properties, Geophysical Research Letters, 31(10), L10307, doi:10.1029/2004GL019506.

Helmer, H.H., F. Kauker, R. Timmermann, J. Determann and J. Rae, 2012. Twenty-first-century warming of a large Antarctic ice-shelf cavity by a redirected coastal current. Nature, 485(7397), 225-228, doi:10.1038/nature11064.

Holdsworth, G., 1969. Flexure of a floating ice tongue, Journal of Glaciology, 8(54), 385-397.

Holland, P.R., 2008. A model of tidally dominated ocean processes near ice shelf grounding lines, Journal of Geophysical Research, 113, C11002, doi:10.1029/2007JC004576.

Holland, D.M., S.S. Jacobs and A. Jenkins, 2003. Modelling the ocean circulation beneath the Ross Ice Shelf, Antarctic Science, 15(1), 13-23, doi:10.1017/S0954102003001019.

Holland, P.R., A. Jenkins and D.M. Holland, 2008. The response of ice shelf basal melting to variation in ocean temperature, Journal of Climate, 21(11), 2558-2572, doi:10.1175/2007JCL1909.1.

Horgan, H.J., R.T. Walker, S. Anandakrishnan and R.B. Alley, 2011. Surface elevation changes at the front of the Ross Ice Shelf: implications for basal melting, Journal of Geophysical Research, 116, C02005, doi:10.1029/2010JC006192.

Horgan, H.J. and S. Anandakrishnan, 2006. Static grounding lines and dynamic ice streams: evidence from the Siple Coast, West Antarctica, Geophysical Research Letters, 33(18), L18502, doi:10.1029/2006GL027091.

Horwath, M., R. Dietrich, M. Baessler, U. Nixdorf, D. Steinhage, D. Fritzsche, V. Damm and G. Reitmayr, 2006. Nivlisen, an Antarctic ice shelf in Dronning Maud Land: geodetic-glaciological results from a combined analysis of ice thickness, ice surface height and ice-flow observations, Journal of Glaciology, 52(176), 17-30, doi:10.3189/172756506781828953.

Hughes, T., 1977. West Antarctic ice streams, Reviews of Geophysics and Space Physics, 15(1), 1-46.

Hughes, T. and J.L. Fastook, 1981. Byrd Glacier: 1978-1979 field results, Antarctic Journal of the US, 16(5), 86-89.

Hulbe, C.L., T.A. Scambos, T. Youngberg and A.K. Lamb, 2008. Patterns of glacier response to disintegration of the Larsen B ice shelf, Antarctic Peninsula, Global and Planetary Change, 63, 1-8, doi:10.1016/j.gloplacha.2008.04.001.

Humbert, A., R. Greve and K. Hutter, 2005. Parameter sensitivity studies for the ice flow of the Ross Ice Shelf, Antarctica, Journal of Geophysical Research, 110(F4), F04022, doi:10.1029/2004JF000170.

Hvidegaard, S.M., L.S. Sorensen and R. Forsberg, 2012. ASTER GDEM validation using LiDAR data over coastal regions of Greenland, Remote Sensing Letters, 3(1), 85-91, doi:10.1080/01431161.2010.527389.

Jacobs, S.S., H.H. Helmer, C.S.M. Doake, A. Jenkins and R.M. Frolich, 1992. Melting of ice shelves and the mass balance of Antarctica, Journal of Glaciology, 38(130), 375-387.

Jacobs, S.S., C.F. Giulivi and P.A. Mele, 2002. Freshening of the Ross Sea during the late 20th century, Science, 297(5580, 386-389, doi:10.1126/science.1069574.

Jacobs, S.S., A. Jenkins, C.F. Giulivi and P. Dutrieux, 2011. Stronger ocean circulation and increased melting under Pine Island Glacier ice shelf, Nature Geoscience, 4(8), 519-523, doi:10.1038/NGEO1188

Jenkins, A., 2011. Convection-driven melting near the grounding lines of ice shelves and tidewater glaciers, Journal of Physical Oceanography, 41(12), 2279-2294, doi:10.1175/JPO-D-11-03.1.

Jenkins, A., D.G. Vaughan, S.S. Jacobs, H.H. Hellmer and J.R. Keys, 1997. Glaciological and oceanographic evidence of high melt rates beneath Pine Island Glacier, West Antarctica, Journal of Glaciology, 43(143), 114-121.

Jenkins, A., H.F.J. Corr, K.W. Nicholls, C.L. Stewart and C.S.M. Doake, 2006. Interactions between ice and ocean observed with phase-sensitive radar near an Antarctic ice-shelf grounding line, Journal of Glaciology, 52(178), 325-346, doi:10.3189/172756506781828502.

Jenkins, A., P. Dutrieux, S.S. Jacobs, S.D. McPhail, J.R. Perrett, A.T. Webb and D. White, 2010. Observations beneath Pine Island Glacier in West Antarctica and implications for its retreat, Nature Geoscience, 3(7), 468-472, doi:10.1038/NGEO890.

Jenkins, A. and C.S.M. Doake, 1991. Ice-ocean interaction on Ronne Ice Shelf, Antarctica, Journal of Geophysical Research, 96(C1), 791-813, doi:10.1029/90JC01952.

Jezek, K., W. Abdel Jaber and D. Floricioiu, 2011. TerraSAR-X observations of Antarctic outlet glaciers in the Ross Sea sector, 2011 Proc. IEEE Int. Geoscience and Remote Sensing Symposium (IGARSS), 3855–3858, doi:10.1109/IGARSS.2011.6050072.

Joughin, I., 2002. Ice-sheet velocity mapping: a combined interferometric and speckle-tracking approach, Annals of Glaciology, 34, 195–201, doi:10.3189/172756402781817978.

Joughin, I., R. Kwok and M. Fahnestock, 1996. Estimation of ice-sheet motion using satellite radar interferometry: Method and error analysis with application to Humboldt Glacier, Greenland, Journal of Glaciology, 42, 564-575.

Joughin, I.R., R. Kwok and M.A. Fahnestock, 1998. Interferometric estimation of three-dimensional ice-flow using ascending and descending passes, IEEE Transactions on Geoscience and Remote Sensing, 36(1), 25-37, doi:10.1109/36.655315.

Joughin, I.R., S. Tulaczyk, R. Bindschadler and S.F. Price, 2002. Changes in West Antarctic ice stream velocities: observation and analysis, Journal of Geophysical Research, 107(B11), 2289, doi:10.1029/2001JB001029.

Joughin, I., R. Bindschadler, M.A. King, D. Voigt, R.B. Alley, S. Anandakrishnan, H. Horgan, L. Peters, P. Winberry, S.B. Das and G. Catania, 2005. Continued deceleration of Whillans Ice Stream, West Antarctica, Geophysical Research Letters, 32, L22501, doi:10.1029/2005GL024319.

Joughin, I.R., B.E. Smith and D.M. Holland, 2010. Sensitivity of 21st century sea level to ocean-induced thinning of Pine Island Glacier, Antarctica, Geophysical Research Letters, 37, L20502, doi:10.1029/2010GL044819.

Joughin, I., R.B. Alley and D.M. Holland, 2012. Ice-sheet response to oceaninc forcing. Science, 338(6111), 1172-1176, doi:10.1126/science.1226481

Joughin, I. and L. Padman, 2003. Melting and freezing beneath Filchner-Ronne Ice Shelf, Antarctica, Geophysical Research Letters, 30(9), L01477, doi:10.1029/2003GL016941.

Joughin, I. and R.B. Alley, 2011. Stability of the West Antarctic ice sheet in a warming world, Nature Geoscience, 4(8), 506-513, doi:10.1038/NGEO1194.

Kenneally, J.R. and T.J. Hughes, 2003. Basal melting along the floating part of Byrd Glacier, Antarctic Science, 16(3), 355-358, doi:10.1017/S0954102004002068.

Keys, H. and D. Fowler, 1989. Sources and movement of icebergs in the south-west Ross Sea, Antarctica, Annals of Glaciology, 12, 85-88.

King, M., R. Coleman and P. Morgan, 2000. Treatment of horizontal and vertical tidal signals in GPS data: A case study on a floating ice shelf, Earth Planets and Space, 52(11), 1043-1047.

King, M., 2004. Rigorous GPS data-processing strategies for glaciological applications, Journal of Glaciology, 50, 601-607, doi: 10.3189/172756504781829747.

King, M.A., T. Murray and A.M. Smith, 2010. Non-linear responses of Rutford Ice Stream, Antarctic, to semi-diurnal and diurnal tidal forcing. Journal of Glaciology, 56, 167-176, doi:10.3189/002214310791190848.

Knudsen, R., R. Bingham, O. Andersen and M. Rio, 2011. A global mean dynamic topography and ocean circulation estimation using a preliminary GOCE gravity model, Journal Geodesy, 85, 861-879, doi:10.1007/s00190-011-0485-8.

Korona, J., E. Berthier, M. Bernard, F. Remy and E. Thouvenot, 2009. SPIRIT: SPOT 5 stereoscopic survey of polar ice: reference images and topographies during the fourth International Polar Year (2007-2009), ISPRS Journal of Photogrammetry and Remote Sensing, 64(2), 204-212, doi:10.1016/j.isprsjprs.2008.10.005.

Krieger, G., H. Fiedler, I. Hajnsek, M. Eineder, M. Werner and A. Moreira, 2005. TanDEM-X: Mission Concept and Performance Analysis, Proceedings of IGARSS 2005, Seoul, Korea, July 25-29, 2005.

Krieger, T., W. Curtis and J. Haase, 2011. Global validation of the ASTER Global Digital Elevation Model (GDEM) Version 2. Report to the ASTER GDEM Version 2 Validation Team.

Kwok, R., and M.A. Fahnestock, 1996. Ice sheet motion and topography from radar interferometry. IEEE Trans. Geosciences and Remote Sensing, 34, 189-200, 1996.

Lee, C.K., K.W. Seo, S.C. Han, J. Yu and T.A. Scambos, 2012. Ice velocity mapping of Ross Ice Shelf, Antarctica by matching surface undulations measured by ICESat laser altimetry, Remote Sensing of Environment, 124, 251-258, doi:10.1016/j.rse.2012.05.017.

Legresy, B., A. Wendt, I. Tabacco, F. Remy and R. Dietrich, 2004. Influence of tides and tidal current on Mertz Glacier, Antarctica. Journal of Glaciology, 50(170), 427-435, doi:10.3189/172756504781829828.

Lenaerts, J.T.M., M.R. van den Broeke, W.J. van de Berg, E. van Meijgaard and P.K. Munneke, 2012. A new, high-resolution surface mass balance map of Antarctica (1979-2010) based on regional atmospheric climate modeling, Geophysical Research Letters, 39, L04501, doi:10.1029/2011GL050713.

Lesnic, D., T. Elliot and D.B. Ingham, 1999. Analysis of coefficient identification problems associated to the inverse Euler-Bernoulli beam theory, IMA Joural of Applied Mathematics, 62, 101-116, doi:10.1093/imamat/62.2.101.

Levitus, S., J. Antonov and T. Boyer, 2005. Warming of the world ocean, 1955-2003, Geophysical Research Letters, 32(2), L02604, doi:10.1029/2004GL021592.

Loose, B., P. Schlosser, W.M. Smethie and S. Jacobs, 2009. An optimized estimate of glacial melt from the Ross Ice Shelf using noble gases, stable isotope, and CFC transient tracers, Journal of Geophysical Research, 114, C08007, doi:10.1029/2008JC005048.

Liu, H., K. Jezek, B. Li and Z. Zhao, 2001. Radarsat Antarctic Mapping Project Digital Elevation Model Version 2. Boulder, Colorado, USA: National Snow and Ice Data Center.

Little, C.M., A. Gnanadesikna and M. Oppenheimer, 2009. How ice shelf morphology controls basal melting, Journal of Geophysical Research, 114, C12007, doi:10.1029/2008JC005197.

Lucchitta, B.K and H.M. Ferguson, 1986. Antarctica: Measuring glacier velocity from satellite images, Science, 234(4780), 1105-1108, doi:10.1126/science.234.4780.1105.

Luccinetti, E. and E. Stussi, 2002. Measuring the flexural rigidity in non-uniform beams using an inverse problem approach, Inverse Problems, 18(3), 837-857, doi:10.88/0266-5611/18/3/320.

Magruder, L., E. Silverberg, C. Webb and B. Schutz, 2005. In situ timing and pointing verification of the ICESat altimeter using a ground-based system, Geophysical Research Letters, 32(21), L21S04, doi:10.1029/2005GLO23504.

Makinson, K., M.A. King, K.W. Nicholls and G.H. Gudmundsson, 2012. Diurnal and semidiurnal tide-induced lateral movement of Ronne Ice Shelf, Antarctica, Geophysical Research Letters, 38, L10501, doi:10.1029/2012GL051636, 2012.

Marsh, O.J., and W. Rack, 2012. A method of calculating ice-shelf surface velocity using ICESat altimetry, Polar Record, 48, 25–30, doi:10.1017/S0032247411000362.

Marsh, O.J., W. Rack, D. Floricioiu, N.R. Golledge and W. Lawson, 2013. Tidally-induced velocity variations of the Beardmore Glacier, Antarctica, and their representation in satellite measurements of ice velocity, The Cryosphere Discuss, 7, 1761-1785, doi:10.5194/tcd-7-1761-2013.

McGill, M., T. Markus, V.S. Scott, and T. Neumann, 2013. The Multiple Altimeter Beam Experiment Lidar (MABEL): An airborne simulator for the ICESat-2 Mission, Journal of Atmospheric and Oceanic Technology, 30, 345-352, doi:10.1175/JTECH-D-12-00076.1.

Mckay, R.M., G.B. Dunbar, T.R. Naish, P.J. Barrett, L. Carter and M. Harper, 2008. Retreat history of the Ross Ice Sheet (Shelf) since the Last Glacial Maximum from deep-basin sediment cores around Ross Island, Palaeogeography Palaeoclimatology Palaeoecology, 260(1-2), 245-261, doi:10.1016/j.palaeo.2007.08.015.

McLay, N.R., 2013. Ice velocity and mass balance study of the Skelton Glacier, Antarctica, using remote sensing and GIS techniques, Masters Thesis, University of Canterbury, NZ.

Meredith, M.P. and J.C. King, 2005. Rapid climate change in the ocean west of the Antarctic Peninsula during the second half of the 20th century, Geophysical Research Letters, 32(19), L19604, doi:10.1029/2005GL024042.

Monaghan, A.J., D.H. Bromwich and S.H. Wang, 2006. Recent trends in Antarctic snow accumulation from Polar MM5 simulations, Philosophical Transactions of the Royal Society A, 364(1844), 1683-1708, doi:10.1098/rsta.2006.1795.

Morris, E.M. and D.G. Vaughan, 2003. Spatial and temporal variation of surface temperature on the Antarctic Peninsula and the limit of viability of ice shelves, Antarctic Peninsula Climate Variability: Historical and Paleoenvironmental Perspectives, Antarctic Research Series, ed. Domack, E., A. Leventer, A. Burnett, R. Bindschadler, P. Convey and M. Kirby, Antarctic Research Series, 79, 61-68.

Mouginot, J., B. Scheuchl and E. Rignot, 2012. Mapping of ice motion in Antarctica using synthetic aperture radar data, Remote Sensing, 4(9), 2753-2767, doi:10.3390/rs4092753.

Murray, T., A.M. Smith, M.A. King and G.P. Weedon, 2007. Ice flow modulated by tides at up to annual periods at Rutford Ice Stream, West Antarctica, Geophysical Research Letters, 34(18), L18503, doi:10.1029/2007GL031207.

Naish, T., R. Powell, R. Levy, G. Wilson, R. Scherer, F. Talarico, L. Krissek, F. Niessen, M. Pompilio, T. Wilson, L. Carter, R. DeConto, P. Huybers, R. McKay, D. Pollard, J. Ross, D. Winter, P. Barrett, G. Browne, R. Cody, E. Cowan, J. Crampton, G. Dunbar, N. Dunbar, F. Florindo, C. Gebhardt, I. Graham, M. Hannah, D. Hansaraj, D. Harwood, D. Helling, S. Henrys, L. Hinnov, G. Kuhn, P. Kyle, A. Laufer, P. Maffioli, D. Magens, K. Mandernack, W. McIntosh, C. Millan, R. Morin, C. Ohneiser, T. Paulsen, D. Persico, I. Raine, J. Reed, C. Riesselman, L. Sagnotti, D. Schmitt, C. Sjunneskog, P. Strong, M. Tavianai, S. Vogel, T. Wilch and T. Williams, 2009. Obliquity-paced Pliocene West Antarctic Ice Sheet oscillations, Nature, 458, 322-328, doi:10.1038/nature07867.

NASA, 2013. Retrieved from http://icesat.gsfc.nasa.gov/icesat2/

Neckel, N., R. Drews, W. Rack and D. Steinhage, 2012. Basal melting at the Ekstrom Ice Shelf, Antarctica, estimated from mass flux divergence, Annals of Glaciology, 53(60), 294-302, doi:10.3189/2012AoG60A167.

Nicholls, K.W., S. Osterhus, K. Makinson, T. Gammelsrod and E. Fahrbach, 2009. Ice-ocean processes over the continental shelf of the southern Weddell Sea, Antarctica: a review, Reviews in Geophysics, 47, RG3003, doi:10.1029/2007RG000250.

Nye, J.F., 1965. The flow of a glacier in a channel of rectangular, elliptic of parabolic cross-section, Journal of Glaciology, 5, 661–690.

Oppenheimer, M., 1998. Global warming and the stability of the West Antarctic Ice Sheet, Nature, 393(6683), 325-332, doi:10.1038/30661.

Padman, L., H. Fricker, R. Coleman, S. Howard and L. Erofeeva, 2002. A new tide model for the Antarctic ice shelves and seas, Annals of Glaciology, 34(1), 247-254, doi:10.3189/172756402781817752.

Padman, L., M. King, D. Goring, H. Corr and R. Coleman, 2003. Ice-shelf elevation changes due to atmospheric pressure variations, Journal of Glaciology, 49(167), 521-526, doi:10.3189/17275650378180386.

Padman, L., S.Y. Erofeeva, H.A. Fricker, 2008. Improving Antarctic tide models by assimilation of ICESat laser altimetry over ice shelves, Geophysical Research Letters, 35(22), L22504, doi:10.1029/2008GL035592.

Pattyn, F., K. Matsuoka, D. Callens, H. Conway, M. Depoorter, D. Docquier, B. Hubbard, D. Samyn and J.L. Tison, 2012. Melting and refreezing beneath Roi Baudouin Ice Shelf (East Antarctica) inferred from radar, GPS, and ice core data, Journal of Geophysical Research, 117, F04008, doi:10.1029/2011JF002154.

Pattyn, F., C. Schoof, L. Perichon, R.C.A. Hindmarsh and 15 others, 2012. Results of the Marine Ice Sheet Model Intercomparison Project, MISMIP. Cryosphere, 6(3), 573-588, doi:10.5194/tc-6-573-2012

Pavlis, N.K., S.A. Holmes, S.C. Kenyon and J.K. Factor, 2012. The development and evaluation of the Earth Gravitational Model 2008 (EGM 2008), Journal of Geophysical Research, 117, B04406, doi:10.1029/2011JB008916.

Pawlowicz, R., B. Beardsley and S.Lentz, 2002. Classical tidal harmonic analysis including error estimates in MATLAB using T_TIDE, Computers and Geosciences, 28(8), 929-937, doi:10.1016/S0098-3004(02)00013-4.

Payne, A.J., A. Vieli, A.P. Shepherd, D.J. Wingham and E. Rignot, 2004. Recent dramatic thinning of largest West Antarctic ice stream triggered by oceans, Geophysical Research Letters, 31(23), L23401, doi:10.1029/2004GL021284.

Payne, A.J., P.R. Holland, A.P. Shepherd, I.C. Rutt, A. Jenkins and I. Joughin, 2007. Numerical modelling of ocean-ice interactions under Pine Island Bay's ice shelf, Journal of Geophysical Research, 112(C10), C10019, doi:10.1029/2006JC003733

Petrenko, V.F and R.W. Whitworth, 1999. *Physics of Ice*, Oxford University Press, Oxford, UK.

Pollard, D. and R. DeConto, 2009. Modelling West Antarctic ice sheet growth and collapse through the past five million years, Nature, 458(7236), 329-332, doi:10.1038/nature07809.

Pritchard, H.D., R.J. Arthern, D.G. Vaughan and L.A. Edwards, 2009. Extensive dynamic thinning on the margins of the Greenland and Antarctic ice sheets, Nature, 461(7266), 971-975, doi:10.1038/nature08471

Pritchard, H.D., S.R.M., Ligtenberg, H.A. Fricker, D.G. Vaughan, M.R. van den Broeke and L. Padman, 2012. Antarctic ice-sheet loss driven by basal melting of ice shelves, Nature, 484(7395), 502-505, doi:10.1038/nature10968.

Pritchard, H.D and D.G. Vaughan, 2007. Widespread acceleration of tidewater glaciers on the Antarctic Peninsula. Journal of Geophysical Research, 112, F03S29, doi:19.1029/2006JF000597.

Rabus, B.T. and O. Lang, 2002. On the representation of ice-shelf grounding zones in SAR interferograms, Journal of Glaciology, 48(162), 345-356, doi:10.3189/172756502781831197.

Reddy, T.E., D.M. Holland and K.R. Arrigo, 2010. Ross ice shelf cavity circulation, residence time, and melting: results from a model of oceanic chlorofluorocarbons, Continental Shelf Research, 30(7), 733-742, doi:10.1016/j.csr.2010.01.007.

Reeh, N., C. Mayer, O.B. Olesen, E.L. Christensen and H.H. Thomsen, 2000. Tidal movement of Nioghalvfjerdsfjorden glacier, northeast Greenland: observations and modelling, Annals of Glaciology, 31, 111-117, doi:10.3189/172756400781820408.

Reeh, N., E.L. Christensen, C. Mayer and O.B. Olesen, 2003. Tidal bending of glaciers: a linear viscoelastic approach, Annals of Glaciology, 37, 83-89, doi:10.3189/172756403781815663.

Riger-Kusk, M., 2011. Ice dynamics of the Darwin-Hatherton glacier system, Transantarctic Mountains, Antarctica, Ph.D. Thesis. University of Canterbury, New Zealand.

Rignot, E., 1996. Tidal motion, ice velocity and melt rate of Petermann Gletscher, Greenland, measured from radar interferometry, Journal of Glaciology, 42, 476-485.

Rignot, E., 2002. Mass balance of East Antarctic glaciers and ice shelves from satellite data. Annals of Glaciology, 34, 217-227, doi:10.3189/172756402781817419.

Rignot, E., J.L. Bamber, M.R. van den Broeke, C. Davis, Y. Li, W.J. van den Berg and E. van Meijgaard, 2008. Recent Antarctic ice mass loss from radar interferometry and regional climate modelling, Nature Geoscience, 1(2), 106-110, doi:10.1038/ngeo102.

Rignot, E., J. Mouginot and B. Scheuchl, 2011. Antarctic grounding line mapping from differential satellite radar interferometry. Geophysical Research Letters, 38, L10504, doi:10.1029/2011GL047109.

Rignot, E., J. Mouginot and B. Scheuchl, 2011. Ice flow of the Antarctic Ice Sheet. Science, 333(6048), 1427-1430, doi:10.1126/science.1208336.

Rignot, E., S. Jacobs, J. Mouginot and B. Scheuchl, 2013. Ice-shelf melting around Antarctica, Science, 341(6143), 266-270, doi:10.1126/science.1235798.

Rignot, E. and S.S. Jacobs, 2002. Rapid bottom melting widespread near Antarctic ice sheet grounding lines, Science, 296(5575), 2020-2023, doi:10.1126/science.1070942.

Rignot, E. and K. Steffen, 2008. Channelized bottom melting and stability of floating ice shelves, Geophysical Research Letters, 35, 2-6, doi:10.1029/2007GL031765.

Rignot, E. and R.H. Thomas, 2002. Mass balance of polar ice sheets, Science, 297(5586), 1502-1506, doi:10.1126/science.1073888.

Rott, H., W. Rack., P. Skvarca and H. de Angelis, 2002. Northern Larsen Ice Shelf, Antarctica: further retreat after collapse, Annals of Glaciology, 34, 277-282, doi:10.3189/172756402781817716.

Sayag, R. and M.G. Worster, 2011. Elastic response of a grounded ice sheet coupled to a floating ice shelf, Physical Review E, 84, 036111, doi:10.1103/PhysRevE.84.036111.

Scambos, T.A., M.J. Dutkiewicz, J.C. Wilson and R.A. Bindschadler, 1992. Application of image cross-correlation to the measurement of glacier velocity using satellite image data, Remote Sensing of Environment, 42(3), 177-186, doi:10.1016/0034-4257(92)90101-O.

Scambos, T.A., C. Hulbe, M. Fahnestock and J. Bohlander, 2000. The link between climate warming and break-up of ice shelves in the Antarctic Peninsula, Journal of Glaciology, 46(154), 516-530, doi:10.3189/172756500781833043.

Scambos, T.A., J.A. Bohlander, C.A. Shuman and P. Skvarca, 2004. Glacier acceleration and thinning after ice shelf collapse in the Larsen B embayment, Antarctica. Geophysical Research Letters, 31, L18402, doi:10.1029/2004GL020670.

Schenk, T., B. Csatho, C.J. van der Veen, H. Brecher, Y. Ahn and T. Yoon, 2005. Registering imagery to ICESat data for measuring elevation changes on Byrd Glacier, Antarctica, Geophysical Research Letters, 32(23), L23S05, doi:10.1029/2005GL024328.

Scheuchl, B., J. Mouginot and E. Rignot, 2012. Ice velocity changes in the Ross and Ronne sectors observed using satellite radar data from 1997 and 2009, The Cryosphere, 6, 1019-1030., doi:10.5194/tc-6-1019-2012.

Schmeltz, M., E. Rignot, D.R. MacAyeal, 2001. Ephemeral grounding as a signal of ice-shelf change, Journal of Glaciology, 47(156), 71-77, doi:10.3189/172756501781832502.

Schmeltz, M., E. Rignot, and D. MacAyeal, 2002. Tidal flexure along ice-sheet margins: comparison of InSAR with an elastic-plate model, Annals of Glaciology, 34, 202-208, doi:10.3189/172756402781818049.

Schoof, C., 2007. Ice sheet grounding line dynamics: Steady states, stability and hysteresis. Journal of Geophysical Research, 112(F3), F03S28, doi:10.1029/2006JF000664.

Schulson, E.M. and P. Duval, 2009. Creep and Fracture of Ice, Cambridge University Press, Cambridge.

Schutz, B.E., H.J. Zwally, C.A. Shuman, D. Hancock and J.P. DiMarzio, 2005. Overview of the ICESat Mission, Geophysical Research Letters, 32, L21S01, doi:10.1029/2005GL024009.

Schwalbe, E. and H.G. Maas, 2009. Motion analysis of fast flowing glaciers from multi-temporal terrestrial laser scanning, Photogrammetrie Fernerkundung Geoinformation, 1, 91-98, doi:10.1127/0935-1221/2009/0009.

Scott, J.B.T., G.H. Gudmundsson, A.M. Smith, R.G. Bingham, H.D. Pritchard and D.G. Vaughan, 2009. Increased rate of acceleration on Pine Island Glacier strongly coupled to changes in gravitational driving stress, Cryosphere, 3(1), 125-131, doi:10.5194/tc-3-125-2009.

Shepherd, A., D. Wingham, T. Payne and P. Skvarca, 2003. Larsen Ice Shelf has progressively thinned. Science, 302(5646), 856-859, doi:10.1126/science.1089768.

Shepherd, A., D. Wingahm and E. Rignot, 2004. Warm ocean is eroding West Antarctic Ice Sheet. Geophysical Research Letters, 31(23), L23402, doi:10.1029/2004GL021106.

Shpeherd, A., D. Wingham, D. Wallis, K. Giles, S. Laxon and A.V. Sundal, 2010. Recent loss of floating ice and the consequent sea level contribution, Geophysical Research Letters, 37, L13503, doi:10.1029/2010GL042496.

Shepherd, A. and D. Wingham, 2007. Recent sea-level contributions of the Antarctic and Greenland ice sheets, Science, 315(5818), 1529-1532, doi:10.1126/science.1136776.

Siegert, M.J., S. Carter, I. Tabacco, S. Popov and D.D. Blakenship, 2005. A revised inventory of Antarctic subglacial lakes, Antarctic Science, 17, 453-460, doi:10.1017/S0954102005002889.

Smith, A.M., 1996. Ice shelf basal melting at the grounding line, measured from seismic observations, Journal of Geophysical Research, 101(C10), 22749-22755, doi:10.1029/96JC02173.

Smith, B.E., C.R. Bentley and C.F. Raymond, 2005. Recent elevation changes on the ice streams and ridges of the Ross Embayment from ICESat crossovers, Geophysical Research Letters, 32, L21S09, doi:10.1029/2005GL024365.

Smith, B.E., H.A. Fricker, I.R. Joughin and S. Tulaczyk, 2009. An inventory of active subglacial lakes in Antarctica detected by ICESat (2003-2008), Journal of Glaciology, 55 (192), 573-595, doi:10.3189/002214309789470879.

Smith, A.M., T. Murray, 2009. Bedform topography and basal conditions beneath a fast-flowing West Antarctic Ice Stream, Quaternary Science Reviews, 28(7-8), 584-596, doi:10.1016/j.quascirev.2008.05.010.

Stearns, L.A., 2007. Outlet glacier dynamics in East Greenland and East Antarctica, Ph.D. Thesis, The University of Maine, United States of America.

Stearns, L.A., 2011. Dynamics and mass balance of four large East Antarctic outlet glaciers. Annals of Glaciology, 52(59), 116-126, doi:10.3189/172756411799096187.

Stearns, L.A., B.E. Smith and G.S. Hamilton, 2008. Increased flow speed on a large East Antarctica outlet glacier caused by subglacial floods, Nature Geoscience, 1, 827-831, doi:10.1038/ngeo356.

Stuart, A. W. and A. J. Heine, 1961. Glaciological work of the 1959-60 U.S. Victoria Land traverse, Journal of Glaciology, 3(30), 997-1002.

Studinger, M., L. Koenig, S. Martin and J. Sonntag, 2010. Operation IceBridge: using instrumented aircraft to bridge the observational gap between ICESat and ICESat-2, 2010 IEEE International Geoscience and Remote Sensing Symposium (IGARSS), 1918-1919, doi:10.1109/IGARSS.2010.5650555.

Swithinbank, C.W., 1963. Ice movement of valley glaciers flowing into Ross Ice Shelf, Antarctica. Science, 141(358), 523-524. doi:10.1126/science.141.3580.523.

Sykes, H.J., T. Murray and A. Luckman, 2009. The location of the grounding zone of Evans Ice Stream, Antarctica, investigated using SAR interferometry and modelling, Annals of Glaciology, 50(52), 35-40, doi:10.3189/172756409789624292.

Thoma, M., A. Jenkins, D. Holland and S. Jacobs, 2008. Modelling Circumpolar Deep Water intrusions on the Amundsen Sea continental shelf, Antarctica, Geophysical Research Letters, 35(18), L18602, doi:10.1029/2008GL034939.

Thomas, R.H., D.R. MacAyeal, D.H. Eilers and D.R. Gaylord, 1984. Glaciological studies on the Ross Ice Shelf, Antarctica, 1972-1978. The Ross Ice Shelf: Glaciology and Geophysics Antarctic Research Series, 42(2), 21-53, AGU.

Tikhonov, A.N. and V.Y. Arsenin, 1977. Solutions of ill-posed problems, New York, etc., Wiley.

van den Broeke, M., 2008. Depth and density of the Antarctic firn layer, Arctic Antarctic and Alpine Research, 40(2), 432-438, doi:10.1657/1523-0430(07-021)[BROEKE]2.0.CO;2.

Vanderveen, C.J., 1985. Response of a marine ice-sheet to changes at the grounding line. Quaternary Research, 24(3), 257-267, doi:10.1016/0033-5894(85)90049-3.

Vaughan, D.G., 1995. Tidal flexure at ice shelf margins, Journal Geophysical Research, 100(B4), 6213-6224, doi:10.1029/94JB02467.

Vaughan, D.G., 2008. West Antarctic Ice Sheet collapse - the fall and rise of a paradigm, Climatic Change, 91(1) 65-79, doi:10.1007/s10584-008-9448-3.

Vaughan, D.G., H.F.J. Corr, R. Bindschadler, P. Dutrieux, G.H. Gudmundsson, A. Jenkins, T. Newman, P. Vornberger and D.J. Wingham, 2012. Subglacial melt channels and fracture in the floating part of Pine Island Glacier, Antarctica, Journal of Geophysical Research, 117, 1-10, doi:10.1029/2012JF002360.

Velicogna, I. and J. Wahr, 2006. Measurements of time-variable gravity show mass loss in Antarctica, Science, 311(5768), 1754-1756, doi:10.1126/science.1123785.

Vieli, A., A.J. Payne, A. Shepherd and Z. Du., 2007. Causes of pre-collapse changes of the Larsen B ice shelf: numerical modelling and assimilation of satellite observations, Earth and Planetary Science Letters, 259(3), 297-306, doi:10.1016/j.epsl.2007.04.050.

Walker, D.P., M.A. Brandon, A. Jenkins, J.T. Allen, J.A. Dowdeswell and J. Evans, 2007. Oceanic heat transport onto the Amundsen Sea shelf through a submarine glacial trough. Geophysical Research Letters, 34, L02602, doi:10.1029/2006GL028154.

Walker, R.T., T.K. Dupont, B.R. Parizek and R.B. Alley, 2008. Effects of basal-melting distribution on the retreat of ice-shelf grounding lines, Geophysical Research Letters, 35(17), L17503, doi:10.1029/2008GL034947.

Walker, R.T., B.R. Parizek, R.B. Alley, S. Anandakrishnan, K.L. Riverman and K. Christianson, 2013. Ice-shelf tidal flexure and subglacial pressure variations, Earth and Planetary Science Letters, 361, 422-428, doi:10.1016/j.epsl.2012.11.008.

Weertman, J., 1974. Stability of the junction of an ice sheet and an ice shelf. Journal of Glaciology, 13(67), 3-11.

Wen, J., Y. Wang, W. Wang, K.C. Jezek, H. Liu and I. Allison, 2010. Basal melting and freezing under the Amery Ice Shelf, East Antarctica, Journal of Glaciology, 56(195), 81-90, doi:10.3189/002214310791190820.

Wingham, D.J., A.J. Ridout, R. Scharroo, R.J. Arthern and C.K. Shum, 1998. Antarctic elevation change from 1992 to 1996, Science, 282(5388), 456-458, doi:10.1126/science.282.5388.456.

Wingham, D.J., D.W. Wallis and A. Shepherd, 2009. Spatial and temporal evolution of Pine Island Glacier thinning, 1995-2006. Geophysical Research Letters, 36, L17501, doi:10.1029/2009GL039126.

Winkelmann, R., A. Levermann, M.A. Martin and K. Frieler, 2011. Increased future ice discharge from Antarctica owing to higher snowfall, Nature, 492, 239-242, doi:10.1038/nature11616.

Williams, M.J.M., K. Grosfeld, R.C. Warner, R. Gerdes and J. Determann, 2001. Ocean circulation and ice-ocean interaction beneath the Amery Ice Shelf, Antarctica, Journal of Geophysical Research, 106(C10), 22383-22399, doi:10.1029/2000JC000236.

Wilson, C.R. and A.P. Crary, 1961. Ice movement on the Skelton Glacier, Journal of Glaciology, 29, 873-878.

Wuite, J., K.C. Jezek, X. Wu, K. Farness and R. Carande, 2009. The velocity field and flow regime of David Glacier and Drygalski Ice Tongue, Antarctica, Polar Geography, 32(3), 111-127, doi:10.1080/10889370902815499.

Yin, J., J.T. Overpeck, S.M. Griffies, A. Hu, J.L. Russell and R.J. Stouffer, 2011. Different magnitudes of projected subsurface ocean warming around Greenland and Antarctica, Nature Geoscience, 4, 524-528, doi:10.1038/ngeo1189.

Zumberge, J.F., M.B. Heflin, D.C. Jefferson, M.M. Watkins and F.H. Webb, 1997. Precise point positioning for the efficient and robust analysis of GPS data from large networks, Journal of Geophysical Research, 102(B3), 5005-5017, doi:10.1029/96JB03860.

Zwally, J., B. Schutz, W. Abdalati, J. Abshire, C. Bentley, A. Brenner, J. Bufton, J. Dezio, D. Hancock, D. Harding, T. Herring, B. Minster, K. Quinn, S. Palm, J. Spinhirne and R. Thomas, 2002. ICESats laser measurements of polar ice, atmosphere, ocean and land, Journal of Geodynamics, 34, 405-445, doi:10.1016/S0264-3707(02)00042-X.

Zwally, H.J., M.B. Giovinettom, J. Li, H.G. Cornejo, M.A. Beckley, A.C. Brenner, J.L. Saba and D.H. Yi, 2005. Mass changes of the Greenland and Antarctic ice sheets and shelves and contributions to sea-level rise: 1992-2002, Journal of Glaciology, 51(175), 509-527, doi:10.3189/172756505781829007.